

University of Nevada, Reno

**A Fail-safe, Bi-Linear Liquid Spring, Controllable
Magneto-rheological Fluid Damper for a Three-dimensional
Earthquake Isolation System**

A dissertation submitted in partial fulfillment of the
requirements for the degree of Doctor of Philosophy in
Mechanical Engineering

By

Sevki Cesmeci

Dr. Faramarz Gordaninejad/Dissertation Advisor

August, 2017



THE GRADUATE SCHOOL

We recommend that the dissertation
prepared under our supervision by

SEVKI CESMECI

Entitled

**A Fail-safe, Bi-Linear Liquid Spring, Controllable
Magnetorheological Fluid Damper for a Three-dimensional
Earthquake Isolation System**

be accepted in partial fulfillment of the
requirements for the degree of

DOCTOR OF PHILOSOPHY

Faramarz Gordaninejad, Ph.D., Advisor

Yanyao Jiang, Ph.D, Committee Member

Matteo Aureli, Ph.D., Committee Member

Keri L Ryan, Ph.D., Committee Member

Mark A Pinsky, Ph.D., Graduate School Representative

David W. Zeh, Ph. D., Dean, Graduate School

August, 2017

ABSTRACT

Building codes governing building design and construction require that loss of human life is not anticipated during a large, infrequently occurring earthquake. However, earthquake-induced damage to the building load carrying components, nonstructural components, including architectural and mechanical systems, and internal equipment or contents, is still expected in code compliant buildings. Recent earthquakes have shown that economic losses are dominated by damage to nonstructural components and contents. Seismic isolation systems, which consist of layers of rubber or friction bearings separating the building from its foundation, are effective in protecting buildings from damage due to horizontal ground shakings. However, recent realistic large-scale earthquake shaking tests have shown that nonstructural components and contents in isolated buildings are susceptible to damage from vertical motions.

In this study, a fail-safe, bi-linear liquid spring, controllable magnetorheological (MR) damper is designed, built and tested. The device combines the controllable MR damping in addition to the fail-safe viscous damping and liquid spring features on a single unit serving as the vertical component of the building suspension system itself. The controllable MR damping offers an advantage in the case that the earthquake intensity might be higher than that of the design conditions. The bi-linear liquid spring feature provides two different stiffnesses in compression and rebound modes. The higher stiffness in the rebound mode can prevent a possible overturning of the structure during rocking mode of vibrations.

The device can be stacked together along with the traditional elastomeric bearings that are currently used to absorb the horizontal ground motions. In the occasion of an earthquake, it is not only exposed to vertical excitations, but also large residual shear excitations. It has to pass these shear forces between the ground and isolated structure. The theoretical and simulation modeling to overcome this major challenge and achieve other system requirements are presented. In addition, a comprehensive optimization program is developed in ANSYS platform to achieve all design requirements. The fabrication and experimental procedures are discussed. The test results showed that the device performed successfully under the combined axial and shear loadings. To our knowledge, this is the first device that not only can provide large damping and spring forces, but can also operate simultaneously under combined axial and shear loadings. The test results are compared against the theoretical modeling, and the results are discussed.

Keywords: Magnetorheological (MR) Damper, Liquid Spring, Bi-linear Liquid Spring, Seismic Isolation, Vertical Isolation

ACKNOWLEDGEMENTS

I would like to dedicate this work to my parents and brothers who have inspired and supported me throughout my academic career. I also would like to thank my wife, Nuriye who has come to enlighten my life as her name means in the last semester of my Ph.D. studies. Her patience, care, and support are unforgettable.

I would like to express my sincere gratitude to my advisor Dr. Faramarz Gordaninejad for giving me the opportunity to work with him under this unique and challenging project. His guidance, not only academically but also for life, is greatly appreciated. Also, his support and encouragement when I had health problems will not be forgotten.

I would like to thank deeply Dr. Keri L Ryan for her assistance and guidance from civil engineering side throughout the project. It was an invaluable experience to be a part of this interdisciplinary project. I also would like to take this opportunity to thank my other Ph.D. Committee members, Dr. Yanyao Jiang, Dr. Matteo Aureli, and Dr. Mark Pinsky for serving in my committee and for their helpful suggestions.

I thank Dr. Barkan Kavlicoglu from Advanced Materials and Devices, Inc., Chad J Lyttle, Todd Lyttle, and Dr. Patrick N Laplace from Large Scale Structures Laboratory, Tony Berendsen from Machine Shop of Mechanical Engineering Department for their helpful discussions during the fabrication and testing of the device. I especially would like to thank Nich Maus for sharing his knowledge and experience throughout the project.

Finally, I would like to thank the past and current members of Composite and Intelligent Materials Laboratory (CIML).

Siddaiah Yarra, you are not forgotten. I thank you for making my stay memorable at CIML.

This work is supported by National Science Foundation under Grant No, 1437003. Their support is gratefully acknowledged.

TABLE OF CONTENTS

ABSTRACT	i
ACKNOWLEDGEMENTS	iii
TABLE OF CONTENTS	v
LIST OF TABLES	ix
LIST OF FIGURES	x
CHAPTER 1 INTRODUCTION	1
1.1. State-of-the-Art Passive and Semi-active Seismic Isolation	1
1.2. Influence of Vertical Excitation on Structural and Nonstructural Response	7
1.3. Three-dimensional Isolation Systems	8
1.4. Bi-Linear Liquid Spring, Controllable Magnetorheological Dampers	11
1.4.1. Bi-linear Liquid Springs	13
1.4.2. Compressible Magnetorheological Dampers	14
1.5. Objective and Scope	19
1.6. Dissertation Organization	20
CHAPTER 2 DESIGN OF A BI-LINEAR LIQUID SPRING, CONTROLLABLE MAGNETORHEOLOGICAL DAMPER	22
2.1. Introduction	22
2.2. Analytical Modeling	28

2.2.1. Modeling of a Bi-directional, Bi-linear Liquid Spring	28
2.2.2. Modeling of Seal Friction	30
2.2.3. Fail-safe Viscous Damping	31
2.2.4. Controllable Magnetorheological Damping.....	33
2.3. Finite Element Modeling	36
2.3.1. Structural Analysis	37
2.3.2. Electromagnetic Analysis.....	44
2.3.3. Thermal Analysis	54
2.4. Optimization	65
CHAPTER 3 FABRICATION, EXPERIMENTAL SETUP, AND TEST PROGRAM.....	71
3.1. Introduction.....	71
3.2. Fabrication	71
3.2.1. Fabrication of the Electromagnet.....	73
3.2.2. Assembly of the BLS-CMRD	74
3.3. Experimental Setup.....	77
3.4. Axial Testing.....	82
3.4.1. Quasi-static Test.....	82
3.4.2. Seal Friction Characterization.....	85
3.4.3. Bi-linear Liquid Spring, Viscous Damping.....	85

3.4.4. Bi-linear Liquid Spring, Viscous Damping, Controllable Magnetorheological Damping	86
3.4.5. Tests with Scaled Earthquake Motions	87
3.5. Combined Axial and Shear Testing	87
CHAPTER 4 EXPERIMENTAL RESULTS AND MODEL VERIFICATION .	89
4.1. Introduction.....	89
4.2. Seal Friction Characterization.....	89
4.3. Bi-linear Liquid Spring, Viscous Damping	90
4.4. Bi-linear Liquid Spring, Viscous Damping, Controllable Magnetorheological Damping	92
4.5. Tests with Scaled Earthquake Motions.....	100
4.6. Combined Axial and Shear Testing	102
4.7. Model Verifications	104
CHAPTER 5 SUMMARY, CONCLUSIONS, AND FUTURE WORK	111
5.1. Summary	111
5.2. Conclusions.....	112
5.3. Future Work.....	113
REFERENCES	114
APPENDIX A. Device Assembly Protocol	125
APPENDIX B. Test Protocol.....	129

APPENDIX C. Fabrication Drawings of the BLS-CMRD 133

LIST OF TABLES

Table 2.1. Design requirements for the BLS-CMRD.	24
Table 2.2. Optimized Input and Output Parameters.	70
Table 3.1. Components of the BLS-CMRD.....	72
Table 3.2. Test matrix for the characterization of passive damping force.....	86
Table 3.3. Test matrix for the characterization of controllable MR damping.	86
Table 3.4. Earthquake records and scale factors.....	87
Table 3.5. Test matrix for combined axial and shear loading.....	88
Table B.1. Expanded form of the axial test.	129
Table B.2. Expanded form of the axial test-Continued.	130
Table B.3. Axial earthquake tests.	131
Table B.4. Combined axial and shear tests.	132

LIST OF FIGURES

Figure 1.1. (a) Schematic of horizontally deformed and (b) cut-out picture of an elastomeric bearing [1].	2
Figure 1.2. Schematic of a spherical sliding bearing [1].	3
Figure 1.3. A typical fluid viscous damper [3].	4
Figure 1.4. A 20 kN large scale seismic damper [12].....	6
Figure 1.5. Fallen ceiling panels and content disruption in a base isolated building subjected to 80% Tabas (PGA=0.87g horizontal, 0.59 g vertical).	8
Figure 1.6. Schematic for the installation of the BLS-CMRD under a building structure.	11
Figure 1.7. A single-acting liquid spring and its force response [41].....	12
Figure 1.8. A double-acting liquid spring and its force response [39].	14
Figure 2.1. (a) Cut-out view of the BLS-CMRD, (b) close up view of the MR valve, and (c) right half of the MR valve showing the magnetic flux lines and flow gap.	23
Figure 2.2. Design methodology for the BLS-CMRD.....	27
Figure 2.3. Significant geometric design parameters: (a) 2D cross-section of the device and (b) detail view of the top chamber.	28
Figure 2.4. Force vs. displacement curve of bi-directional, bi-linear liquid spring.....	29
Figure 2.5. Force vs. displacement curve of bi-directional, bi-linear liquid spring with friction force for a sinusoidal input of 0.0254 m.	31

Figure 2.6. (a) Schematic of the MR valve in the top chamber and (b) parallel plate approximation of the flow.....	32
Figure 2.7. Force vs. displacement curve of BLS-CMRD with spring, friction force, and viscous damping forces for a sinusoidal input of 0.0254 m at 4 Hz.....	33
Figure 2.8. Graphical representation of the Bingham plastic model.	34
Figure 2.9. Force vs. displacement curve of BLS-CMRD with spring, friction force, viscous, and controllable MR damping forces for a sinusoidal input of 0.0254 m at 4 Hz, and 1 A.....	35
Figure 2.10. (a) Experimental result given in Yang et al. [9] for 1 Hz, 0.0127 m displacement excitation with constant current input of 2 A and (b) theoretical result obtained by using Eqs. (2.7), (2.9), and (2.11) and the same displacement input.	36
Figure 2.11. 3D design model of the test setup with its main components.	37
Figure 2.12. 3D model of the BLS-CMRD. The cylinder is made transparent to show the inside of the device.	38
Figure 2.13. ANSYS FEA model with loading and boundary conditions.....	39
Figure 2.14. (a) Typical properties and (b) PV values of Oilite bearings[84].....	40
Figure 2.15. FEA results: (a) minimum FOS and (b) maximum total deformation (results are magnified by 310%).....	41
Figure 2.16. Convergence history of the strain energy for the FEA analysis of the model shown in Figure 2.13.....	43

Figure 2.17. Variations of the minimum FOS and maximum shear deformation with the radius of the top shaft.....	44
Figure 2.18. (a) Axisymmetric model for the electromagnetic analysis in ANSYS Maxwell and (b) close-up view of the MR valve.	47
Figure 2.19. Magnetic flux density, B , distribution after an electromagnetic analysis for the current input of 2500 A x turns.....	48
Figure 2.20. Variation of dynamic force range, D , with respect to the (a) flow gap, (b) active pole length, (c) piston radius, (d) current input, and (e) passive pole length.	51
Figure 2.21. Variations of viscous damping ratio, ζ_{viscous} , with respect to the (a) flow gap, (b) active pole length, (c) piston radius, (d) current input, and (e) passive pole length.	53
Figure 2.22. Thermal analysis of the BLS-CMRD in ANSYS software.....	56
Figure 2.23. Heat loadings and boundary conditions for the Transient Thermal heating analysis.....	57
Figure 2.24. Temperature distribution over the device after the Transient Thermal heating analysis.....	58
Figure 2.25. Variation of the maximum temperature in the MR fluid with time.	59
Figure 2.26. Variations of the maximum temperature in the MR fluid with respect to stroke, frequency, and current input.	61
Figure 2.27. Temperature distribution after the Transient Thermal cooling analysis.	62

Figure 2.28. Variation of the maximum temperature in the MR fluid when the device is subjected to forced cooling with a fan at room temperature.....	62
Figure 2.29. Effects of temperature on the viscous damping ratio, ζ_{viscous} , dynamic force range, D , and rebound and stiffness, k_r	63
Figure 2.30. Input parameters for the second optimization.	67
Figure 2.31. Output parameters for the second optimization.....	69
Figure 3.1. Setup for winding the electromagnet.....	74
Figure 3.2. Tensioning of the BLS-CMRD with a hydraulic jack.....	75
Figure 3.3. (a) Mold for grouting and (b) insertion of the grout.	76
Figure 3.4. Filling the silicone oil into the bottom chamber.....	76
Figure 3.5. Experimental setup: (a) full-view (back), (b) BLS-CMRD, (c) hydraulic actuator, (d) hydraulic pulling ram, (e), shaft displacement transducer, (f) Current transducer, and (g) DAQ board.....	81
Figure 3.6. MR fluid in the vacuum chamber.....	83
Figure 3.7. Test setup for the measurement of the bulk modulus of the MR fluid.....	84
Figure 3.8. Variation of bulk modulus with pressure for MRF-132DG.	85
Figure 4.1. Seal characterization test at $X = 0.0127$ m and $f = 0.01$ Hz.....	89
Figure 4.2. Force vs. displacement curves at zero current and $X = 0.0127$ m.	91
Figure 4.3. Force vs. displacement curves at zero current and $X = 0.0254$ m.	91
Figure 4.4. Force vs. displacement curves at $X = 0.0127$ m and $f = 1$ Hz.	93

Figure 4.5. Force vs. displacement curves at $X = 0.0127$ m and $f = 2$ Hz.	94
Figure 4.6. Force vs. displacement curves at $X = 0.0127$ m and $f = 4$ Hz.	94
Figure 4.7. Force vs. displacement curves at $X = 0.0254$ m and $f = 0.5$ Hz.	95
Figure 4.8. Force vs. displacement curves at $X = 0.0254$ m and $f = 1$ Hz.	95
Figure 4.9. Force vs. displacement curves at $X = 0.0254$ m and $f = 2$ Hz.	96
Figure 4.10. Force vs. displacement curves at $X = 0.0254$ m and $f = 4$ Hz.	96
Figure 4.11. (a) 2D cross-section of the device and (b) detail view of the top chamber. .	98
Figure 4.12. An alternative design for the BLS-CMRD.	100
Figure 4.13. (a), (b) Northridge-01, LA-Sepulveda V A Hospital, (c), (d) Loma Prieta, LGPC, and (e), (f) Chi-Chi, TCU079, all at 150% design level.	102
Figure 4.14. Force vs. displacement curves at different shear loadings: (a),(b) zero-shear load, (c),(d) 3.34 kN, (e),(f) 6.67 kN, (g),(h) 13.35 kN, and (i),(j) 27.85 kN.	104
Figure 4.15. The experimental and model yield stress vs. current.	105
Figure 4.16. Comparisons between the model and experiments for $X = 0.0127$ m, $f = 0.5$ Hz, and zero current.	106
Figure 4.17. Comparisons between the model and experiments for $X = 0.0127$ m, $f = 1$ Hz, and zero current.	107
Figure 4.18. Comparisons between the model and experiments for $X = 0.0127$ m, $f = 2$ Hz, and zero current.	107

Figure 4.19. Comparisons between the model and experiments for $X = 0.0127$ m, $f = 4$ Hz, and zero current.....	108
Figure 4.20. Comparisons between the model and experiments for $X = 0.0127$ m, $f = 1$ Hz, and different current levels (without modeling the cut-out regions).....	109
Figure 4.21. Comparisons between the model and experiments for $X = 0.0127$ m, $f = 1$ Hz, and different current levels.....	109
Figure 4.22. Comparisons between the model and experiments for $X = 0.0127$ m, $f = 2$ Hz, and different current levels.....	110
Figure 4.23. Comparisons between the model and experiments for $X = 0.0127$ m, $f = 4$ Hz, and different current levels.....	110
Figure A.1. Step 1: Insert the shaft into the cylinder bore (the bottom bearing, seals, bottom seal lower and upper glands were installed on the cylinder).....	125
Figure A.2. Step 2: Install the top seal upper gland (the top bearing was already press-fitted).....	126
Figure A.3. Step 3: Install the top seal lower gland.....	126
Figure A.4. Step 4: Insert the top cap on the shaft.....	127
Figure A.5. Step 5: Install the shaft stopper on the bottom side of the shaft.....	127
Figure A.6. Step 6: Install the top pedestal on the on the top side of the shaft.....	128
Figure A.7. Step 7: Install the bottom cap and fasten the external fastener rods on the top and bottom Caps.	128

CHAPTER 1 INTRODUCTION

Earthquakes have claimed millions of human lives and have cost billions of dollars in property damage throughout the history. Researchers have put a great deal of effort to minimize the losses and damages. In the event of an earthquake, a finite amount of energy is input to the building structures which transforms into kinetic and potential (strain) energies. Although some of this input energy is absorbed through inherent (or material) damping, if structural control devices are not used to dissipate the remaining energy, the structure will continue to shake for an extended period of time. During the shaking, large deformations will cause the structural components to yield and eventually fracture causing losses of human lives as well as economic losses. There have been four major types of structural control devices: passive, active, semi-active, and hybrid systems that have been used to absorb the seismic input energy in the lateral direction.

1.1. State-of-the-Art Passive and Semi-active Seismic Isolation

Passive systems include either elastomeric or spherical sliding bearings, or passive viscous dampers. Elastomeric bearings are composed of alternating layers of natural or synthetic rubber vulcanized and bonded to intermediate steel shim plates. An example of elastomeric bearings is shown in Figure 1.1.

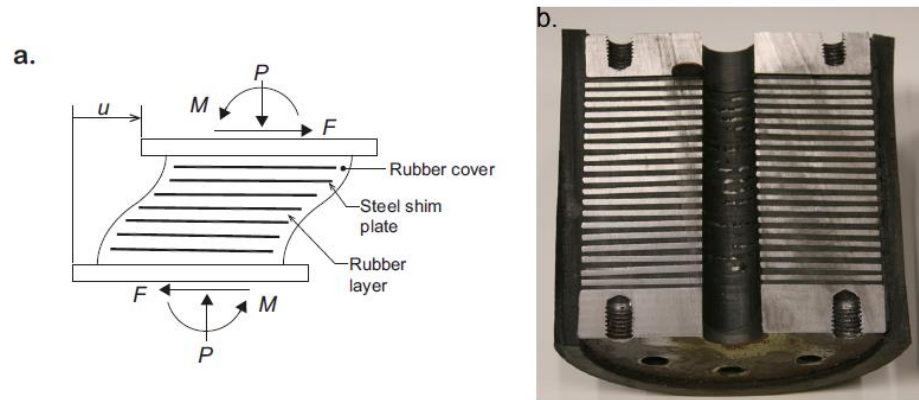


Figure 1.1. (a) Schematic of horizontally deformed and (b) cut-out picture of an elastomeric bearing [1].

The sandwiched rubber layers are allowed both compression and shear deformations in the vertical and horizontal directions, respectively. They are designed such that they have high vertical and low horizontal stiffnesses. The high vertical stiffness enables them to carry the high structural loads, while the low horizontal stiffness provides flexibility in the horizontal direction to dissipate energy. The horizontal and compression stiffnesses can be controlled by several geometric parameters such as the thickness of the rubber layer, bonded rubber area, and a dimensionless shape factor. The latter is defined as the ratio of the loaded area to the area free to bulge for a single rubber layer [1]. Elastomeric bearings can be classified into three groups: low-damping, high-damping, and lead-rubber bearings. Low-damping bearings are designed to accommodate creep and temperature effects, and have an equivalent damping ratio ranging from 2% to 3% at 100% shear strain. High-damping bearings are, on the other hand, used to eliminate the need for external supplemental damping devices, and their equivalent damping ratios range from 10% to 20% at 100% shear strain. Lead-rubber bearings slightly differ from

low-damping bearings in that they have a lead-plug inserted into a hole in the center to increase the dissipation energy through yielding. The lead-rubber has a high pre-yield stiffness providing the required resilience against the disturbances caused by wind or service loads. When the disturbance is high enough, as in the event of an earthquake, the plug plastically deforms and provides additional dissipation [1], [2].

Spherical sliding bearings consist of a base-plate, spherical concave dish and an articulated slider (Figure 1.2). The articulated slider has a low friction surface and is in contact with the curvature on the concave dish. In the event of an earthquake, it both absorbs the horizontal input seismic energy through frictional damping and provides the restoring force to the superstructure. There are different types of sliding bearings actively used in practice such as friction-based bearings (polytetrafluoroethylene (PTFE) spherical bearings), Double PendulumTM, Triple PendulumTM, and Eradquake isolator [1], [2].

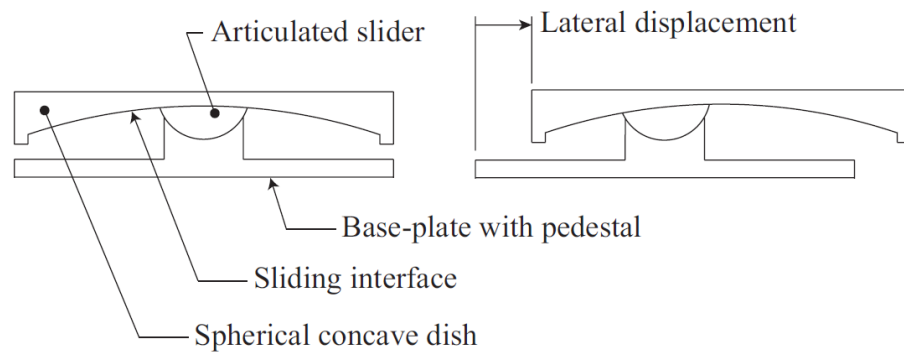


Figure 1.2. Schematic of a spherical sliding bearing [1].

Another type of passive structural control device is the fluid viscous damper. A typical fluid viscous damper is shown in Figure 1.3 with its main components. It basically consists of a cylinder, a piston inside the cylinder, a rod connected to the piston, and both

a dynamic and static sealing system to prevent the fluid leakage from the cylinder. The piston is free to move inside the cylinder, and there is usually a small gap between it and the inner surface of the cylinder. When the device is exposed to an external excitation, the fluid flows through this annular gap from one side of the piston (e.g. chamber 2) to the other side (e.g. chamber 1) thereby damping the input energy through viscous dissipation. Fluid viscous dampers have been extensively used for protection of building structures from earthquake and windstorms. So far more than 240 major structures have been protected by such devices including the Los Angeles City Hall, Pacific Northwest Baseball Stadium in Seattle, Washington, and Torre Mayor in Mexico City, Mexico [3].

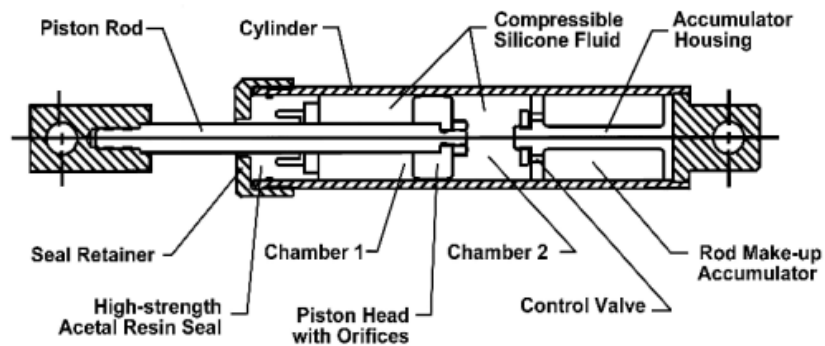


Figure 1.3. A typical fluid viscous damper [3].

Passive dampers have been preferred because of their simple design, low fabrication and maintenance costs, high reliability, and robust performance. However, these dampers have constant damping characteristics and do not adapt to varying loading conditions and load intensity.

More recently, more sophisticated isolation systems, which could adapt to the changing loading conditions, have been developed [4]. These systems essentially are composed of a sensor, a control, and an actuation system. The sensor system measures the excitation input such as acceleration to the structure. A control system acquires the input data from the sensors, computes the required counter force, and sends a corresponding signal to the actuator system to produce the applied reaction force. Actuation systems generally use hydraulic actuators, but magnetic actuators are also available. These systems impart energy to the structure and might cause structural instabilities. Although they might offer remarkable isolation performance, their high power consumption, high fabrication costs, and demanding maintenance also limit their applications in seismic protection.

On the other hand, the last decades have witnessed the development of another type of isolation system called semi-active isolation system that combines the advantages and eliminates the drawbacks or incapacities of passive and active isolation systems. The semi-active systems use field controllable electrorheological (ER) or magnetorheological (MR) dampers that can change their damping characteristics under applied electrical and magnetic fields, respectively [5]. MR dampers have much higher force capacities than the ER dampers; therefore they are more suitable for seismic isolation. MR dampers have the same configuration as the passive fluid viscous dampers. They also consist of an outer cylinder, a piston, and piston rod. The only difference is that they incorporate electromagnetic coils, usually wound around the piston, to alter the damping characteristics of the MR fluid (Figure 1.4). As in the active systems, in semi-active systems there is a sensor, a control, and an actuation mechanism. A sensor reads

the excitation input and transmits it to the control board. The control board, usually a microprocessor, then sends the required input to the electromagnet to change the damping and thus, the force applied by the damper. The semi-active systems require very low power consumption and have low fabrication and maintenance costs as compared to the active systems. They also do not cause structural instabilities since they do not introduce energy to the structure. Another advantage of these adaptive systems is that they are inherently fail-safe devices. In the case of a likely power outage to the device during an earthquake or an electronic failure in the control system, the device would still operate in passive-mode with some preset constant damping characteristics. Their performance level ranges between the upper bound of active systems and lower bound of passive systems. Because of their unique advantages over the passive and active systems, semi-active systems have attracted significant attention in seismic isolation of structural buildings [6]–[11].

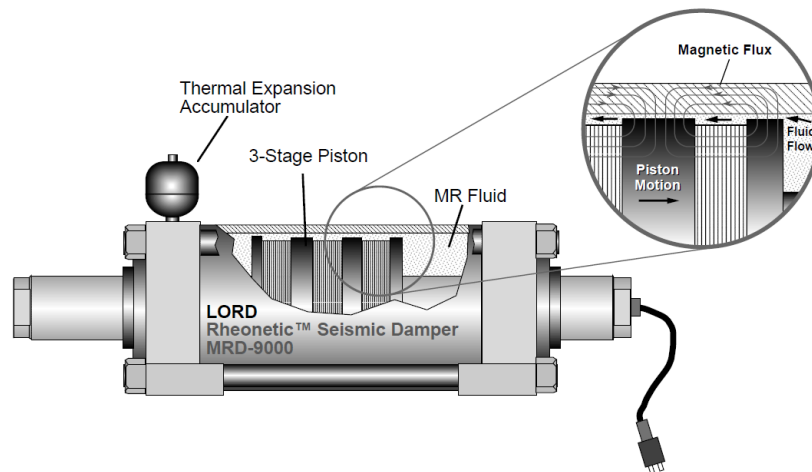


Figure 1.4. A 20 kN large scale seismic damper [12].

1.2. Influence of Vertical Excitation on Structural and Nonstructural Response

Current design procedures are aimed at mitigating the damaging effects of lateral ground excitation, as prompted by the demonstrated collapse potential of weak and non-ductile systems throughout history. Lacking hard evidence that vertical excitation contributes to seismic damage, for most structures design codes do not require that the influence of vertical ground excitation be explicitly considered in seismic design. This approach has been proven to achieve a life safety objective. Techniques targeted at higher performance objectives such as continued functionality—which require protection of the structure, nonstructural components, and contents from damage—also focus primarily on horizontal ground excitation. In past earthquakes, damage to nonstructural components and contents has been shown to constitute the majority of economic losses [13], [14].

Recent evidence from the NEES TIPS/E-Defense test program indicates that the damage potential of vertical excitation on nonstructural components and contents has been underestimated. For example, Figure 1.5 shows a snapshot of the internal rooms of a test building taken while the building isolated with triple friction pendulum bearings was subjected to 80% of the Tabas-Tabas Station record (horizontal PGA = 0.87g and vertical PGA = 0.59g). This photo reflects fallen ceiling panels and content disruption.



Figure 1.5. Fallen ceiling panels and content disruption in a base isolated building subjected to 80% Tabas (PGA=0.87g horizontal, 0.59 g vertical).

A comprehensive literature survey reveals that the nonstructural damage and content disruption in the isolated buildings was most directly related to the vertical vibration of the floor system. Prior to the test program, very few tests incorporated elements allowing for the investigation of realistic seismic induced floor vibration on nonstructural component damage and content disruption, especially when horizontal floor acceleration is constrained to relatively low levels through seismic isolation.

1.3. Three-dimensional Isolation Systems

Research on 3D isolation systems has been largely motivated by the needs of nuclear facilities. Warn and Ryan [1] provide a recent review. Base isolation may be a viable solution to design the structures and components of nuclear power plants for very rare earthquakes without loss of capability to perform their safety functions. A packaged approach that can provide both lateral and vertical attenuation is sought [15].

Traditional horizontal seismic isolation is achieved through flexible devices that shift the vibration period of the structure away from the predominant frequency content of the ground motion. The friction pendulum (FP) bearing and its derivatives (e.g. [16], [17]) are essentially axially rigid in compression with no uplift restraint, and are thus ill-suited for vertical isolation. Elastomeric bearings are detailed with alternating bonded layers of rubber and steel, which together provide lateral flexibility and vertical stiffness to support the weight of the building. Thicker rubber layers may be used to increase the fundamental period in the vertical direction [18]. This approach was explored for the nuclear industry, where a 3D isolation system was designed and characterization tests of individual 1/4th scale bearings were performed [19]. The approach was concluded to be plausible [19], [20], but was not followed up on. However, application of elastomeric devices in 3D isolation has limitations because of their inherent stability issues. The bearing critical load capacity, P_{cr} decreases as the rubber layers get thicker. P_{cr} also decreases with increasing lateral displacements [21]–[24].

GERB, a German-based company, developed a 3D earthquake isolation system based on helical springs with similar flexibility in all three directions and viscous dampers [25]. These 3D isolation systems are known to increase the horizontal floor accelerations compared to horizontal earthquake isolation only. 1994 Northridge Earthquake has severely shaken a three-story residential building in California isolated with a GERB system. The peak horizontal acceleration at the top floor was recorded as 0.63g relative to the input PGA less than 0.5g, providing less performance than an average horizontal seismic isolation only. The vertical PGA was around 0.1g [26].

Japanese researchers have devoted a substantial effort to develop 3D earthquake isolation systems for nuclear facilities. To this end, several approaches that use pressurized air or air springs along with elastomeric bearings were proposed [27]–[32]. Shimizu Corporation applied a 3D seismic isolation system that used air springs for the vertical isolation along with traditional elastomeric bearings for the horizontal isolation. The system also involved viscous oil dampers to suppress the rocking displacements. These solutions have either stability issues or they are quite complicated and costly. Therefore, there is still a need for a viable solution for 3D isolation.

In this study, a novel solution is proposed for the vertical isolation that has not been investigated previously. The novelty of the proposed Bilinear, Liquid Spring, Controllable Magnetorheological Damper (BLS-CMRD) system comes from that it combines the passive, controllable MR damping characteristics, and a bi-linear liquid spring feature in a single unit serving as a suspension system itself. The MR damping property of the device offers a controllable damping in the case that earthquake intensity might be higher than that of the design conditions, whereas the bi-linear liquid spring feature resists rocking/overtipping by increasing the stiffness in the rebound mode. The device works in series with traditional elastomeric bearings that are used to absorb the horizontal seismic excitations. In this configuration, it is exposed to combined large shear and axial loadings (Figure 1.6).

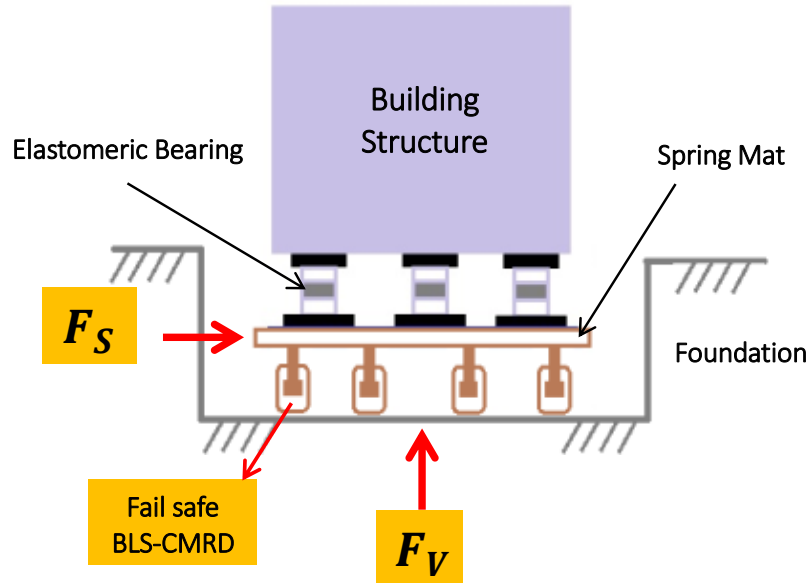


Figure 1.6. Schematic for the installation of the BLS-CMRD under a building structure.

1.4. Bi-Linear Liquid Spring, Controllable Magnetorheological Dampers

Liquid springs take the compressibility property of liquids and use it to store mechanical energy. A liquid spring is generally designed as a cylindrical chamber with a compressible liquid and a piston, and a shaft structure. The spring piston can be a single shaft or a double shaft arrangement that moves axially in and out of the one or two chambers. Figure 1.7 shows a single chamber configuration. In such configuration, when the piston shaft moves into the liquid chamber, it compresses the liquid therein and in response, the liquid generates a resisting force that varies linearly (within a certain compression range) with the displacement of the piston shaft generating a spring effect [33]–[39]. The spring coefficient is a function of the volume of the liquid, the diameter of the shaft, and the bulk modulus of the working liquid [40]:

$$k = \beta \frac{A_s^2}{V} \quad (1.1)$$

where β is the bulk modulus of the MR fluid, A_s is the cross-sectional area of the shaft, and V is the volume of the fluid chamber. Therefore, liquid springs can be designed to a given spring coefficient by adjusting these geometric and material properties.

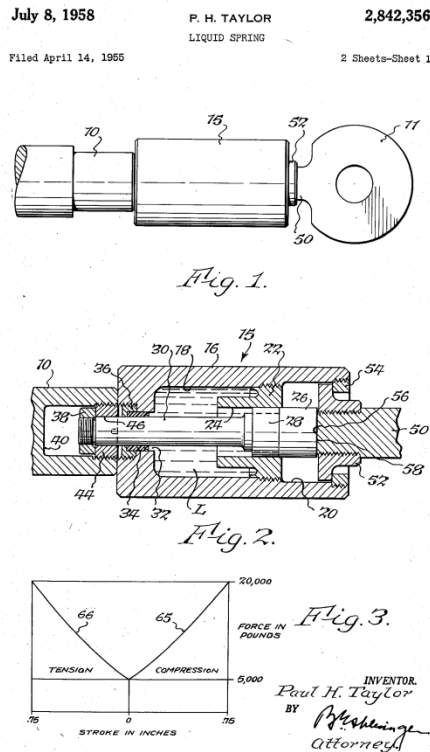


Figure 1.7. A single-acting liquid spring and its force response [41].

Liquid springs have been a research topic since the mid-1900s. Various designs with the ability to seal high pressures and buffer the pressure spike created during the initial compression of the liquid spring have been developed [33]–[39], [42]–[57]. Compared to conventional helical spring suspensions, liquid springs exhibit a desirable combination of simplicity, safety, compactness, excellent dynamic response, and ease of

servicing [35]. Liquid springs are utilized in suspension systems of off-road vehicles, landing gear of aircraft, heavy machinery equipment, passenger vehicles, and military vehicles [35], [45], [47]–[49]. Some of these applications require high pressure to be produced inside the liquid spring to support large weights involved, especially in rough terrain or hard landing. Over the past few decades, the liquid spring has been proposed to replace the conventional, passive damper-helical spring vehicle suspension systems with more compact devices. Compared to the traditional metal helical springs, a liquid spring can have seven times higher spring rates than the metal helical springs under the similar geometric sizes. In addition to this, unlike the helical springs, a liquid spring does not plastically deform or is damaged when it reaches its physical limits; instead it behaves as a rigid body and returns to its original state when the force is removed. This makes them ideal for a high load/small displacement situations as might be desired in an earthquake isolation system [40].

1.4.1. Bi-linear Liquid Springs

Liquid springs can be designed such that they would have different springs rates in both compression and tension modes. In 1955, Hogan [58] built a “double acting liquid shock isolator”, which combined liquid springs of different rates in compression and tension with liquid damping (Figure 1.8). The damping varied proportionally to the relative velocity of the piston. In 1986, Taylor [59] introduced a more compact “tension-compression liquid spring unit” reducing the size of such isolators to make them more available for confined spaces.

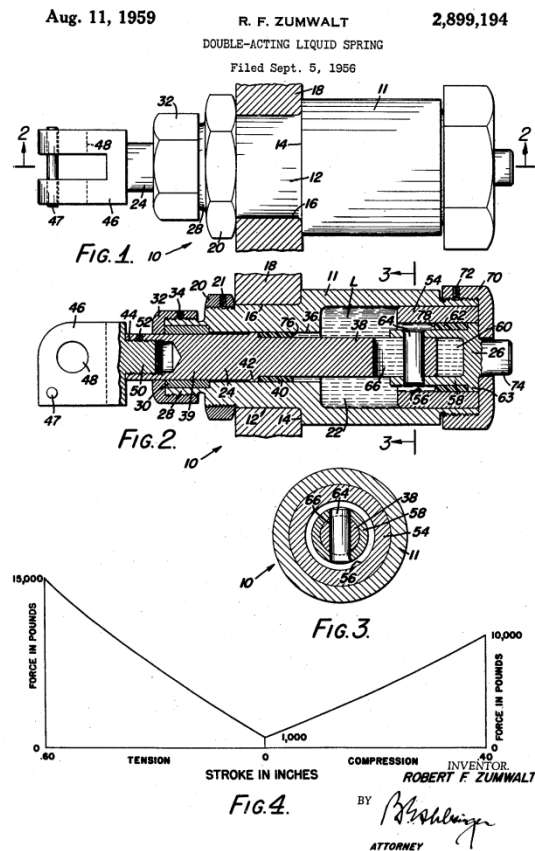


Figure 1.8. A double-acting liquid spring and its force response [39].

1.4.2. Compressible Magnetorheological Dampers

Magnetorheological (MR) dampers incorporate electromagnets to activate the field-controllable MR fluids to provide variable damping in addition to passive viscous damping [60], [61]. MR fluids, discovered by Jacob Rabinow at the US National Bureau of Standards in the late 1940's, are suspensions of magnetically polarizable soft iron particles, having diameters of 1–100 μm , in a special carrier liquid such as water, silicone oil, mineral oil, synthetic and semi-synthetic oils, and glycol [62]–[64]. The essential feature of the MR fluids is that they can reversibly change their states from a Newtonian fluid to a semi-solid or plastic with controllable dynamic yield stress within a few

milliseconds, when they are subjected to an external magnetic field [65]. The ferromagnetic particles reside randomly in the carrier medium, but once the magnetic field is applied, these particles align in the direction of the magnetic flux lines and form a chain-like structure. In order to yield these chain-like structures and initiate the flow in this semi-solid state, a pre-yield stress has to be applied on the fluid. The level of stress needed varies with the magnetic field intensity resulting in a field-dependent yield stress [62]. This behavior of MR fluids can be represented, in the simplest form, with the Bingham plastic constitutive equation,

$$\tau = \tau_y + \mu\dot{\gamma}; \quad \tau > \tau_y \quad (1.2)$$

where τ_y is the field-dependent yield stress, μ is the plastic viscosity, and $\dot{\gamma}$ is the shear strain rate.

MR fluids have been utilized in various engineering applications such as brakes (or clutches), dampers, prosthetic knees, landing gear systems, and many more. However, the efforts have been concentrated on dampers, especially in automotive suspension systems, due to their unique controllable damping feature, mechanical simplicity, robustness, low power consumption, and fast response time [10], [62], [63], [66]–[72]. MR dampers are inherently fail-safe devices from an electronic point of view. If there is a power outage to the device or there is an electronic fault in the system, it could still work as a passive damping device with preset design parameters [73].

Compressible MR dampers utilize both the controllable damping and compressibility of MR fluids to provide both damping and stiffness in a single compact device. There has been an increasing interest in compressible MR dampers in the last

decade. Hong et al. [74] studied a compressible MR strut that used a compressible fluid spring and a bypass MR fluid valve for an automotive suspension system. They employed a hydrodynamic-based modeling to design their device and validated their modeling approach with characterization tests under ramped displacement input at amplitude, frequency and applied currents of 15 mm, 0.167 Hz and 0, 0.5, and 1 A, respectively. The maximum force output of the device was measured to be around 2.5 kN.

More recently, Hitchcock and Gordaninejad [75] patented an adjustable controllable compressible fluid damper that could control both the damping and energy storage capacities of the MR fluid. Their design incorporated two chambers sealed from each other and filled with MR and silicone oils separately. The chamber with the MR fluid featured an MR valve and a constant-diameter shaft before and after the valve piston to generate the variable damping only, whereas the second chamber accommodated an extension of the shaft to produce the spring effect.

Researchers in Composite and Intelligent Material Laboratory (CIML) of University of Nevada, Reno (UNR) have performed various studies about compressible magnetorheological dampers in the last decade. Mantripragada et al. [76] designed, built and tested a compressible magnetorheological damper to examine the feasibility of its use on heavy off-road vehicles. The device, which consisted of two separate liquid spring chambers and an external MR valve, was characterized under sinusoidal displacement input with amplitudes, frequencies, and excitation currents of 0.254 to 1.27 cm, 0.1 to 0.75 Hz, and 0 to 3 A, respectively. The maximum force output of the device was measured to be 18 kN under 1.27 cm displacement, 2 cm/s velocity, and 1 A current

excitations. A phenomenological model was proposed to capture the dynamic behavior of the device. The model was then compared against the experimental data and a good agreement was observed between the model and test data.

Raja et al. [77], [78] conducted another study on the feasibility of a small-scale compressible magnetorheological damper for use in the suspension system of a tracked vehicle to improve the mobility of the vehicle while preserving its stability and safety. Their design utilized a single chamber which accommodated both the MR valve and the spring shaft that is attached to the valve piston. They developed a fluid-mechanics based model to design and predict the behavior of the device and validated the model with experimental results. The experiments were conducted under sinusoidal displacement excitations. Testing amplitudes, frequencies, and currents ranged from 0.254 to 0.635 cm, 0.1 to 1 Hz, and 0 to 2 A, respectively. Their theoretical calculations agreed well with the experimental data and proved to be a useful tool for both designs and predictions of dynamic behaviors of such devices. The maximum force output was measured to be 12 kN for the device.

Potnuru et al. [79] designed, fabricated, and tested another compressible magnetorheological fluid damper-liquid spring. In their study, they investigated the effect of varying cross-sections of flow channel on the velocity profile and pressure drops at different magnetic fields. They also characterized the device under sinusoidal input displacements at different frequencies to obtain its equivalent spring and damping coefficients and energy dissipation.

Mckee et al. [80], [81] investigated the effect of temperature on the performance characteristics of compressible magnetorheological dampers. To this end, they designed, developed, and tested a single-chamber liquid spring with internal MR valve. The experimental results demonstrated that the stiffness and damping are functions of the operating temperature. This was attributed to the fact that both bulk modulus and viscosity of the MR fluid was inversely related to the temperature. When the temperature was increased from 25 °C to 70 °C, both the stiffness and the damping decreased by up to 20%. Moreover, at around 80 °C, the mechanical properties of the seals were observed to deteriorate, which eventually resulted in mechanical failures.

More recently, Maus et al. [40], [82] studied a proof-of-concept of a bilinear, liquid spring, controllable magnetorheological damper. Their design incorporated two chambers that were sealed from each other. One of the chambers housed an internal MR valve and was filled with an MR fluid only. The shaft sections before and after the valve piston had different diameters to achieve the spring effect in this chamber. The other chamber was filled with pure silicone oil and involved an extension of the shaft after the valve piston to produce only the spring effect in this chamber. They presented a fluid-mechanics based modeling for the design of the device and validated the theoretical modeling with the experimental data. Tests were conducted under sinusoidal displacement excitations at amplitudes, frequencies, and currents of up to 2.5 cm, 0.1 to 4 Hz, and 0 to 5 A, respectively. The maximum damper force was measured to be around 11 kN.

All of these efforts in the field of compressible magnetorheological dampers have provided an insight and contributed to the understanding of their behavior under different loading and operating conditions. However, all of the characterization tests have been performed in axial directions only, and the maximum force output of the dampers was not higher than 18 kN.

1.5. Objective and Scope

In this study, a 1/4th scale fail-safe, bi-linear liquid spring, controllable magnetorheological (BLS-CMRD) damper is designed, built, and tested. The device combines the controllable MR damping in addition to the fail-safe viscous damping and liquid spring features on a single unit serving as the vertical component of the building suspension system itself. The controllable MR damping offers an advantage in the case that the earthquake intensity might be higher than that of the design conditions. The bi-linear liquid spring feature provides two different stiffnesses in compression and rebound modes. The higher stiffness in the rebound mode helps prevent a possible overturning of the structure during rocking mode of vibrations. The device is stacked together along with the traditional elastomeric bearings that are currently used to absorb the horizontal ground motions. In the occasion of an earthquake, it is not only exposed to vertical excitations, but also large residual shear excitations that might be up to 28 kN for a scaled earthquake excitations (Figure 1.6). The high shear forces pose several major design challenges. First of all, the device has to be able pass the shear force between the structure and ground without yielding. Also, the shear force applied to the shaft can produce uneven stresses on the seals which might lead to leakage and result in a

premature failure of the device. In addition to these, the device also has to satisfy some other design requirements such as compression and tension stiffnesses, passive damping ratio, maximum allowable temperature rise in the working fluid, etc. In order to achieve all of these design requirements, a comprehensive multi-objective optimization is carried out in ANSYS platform where the Static Structural, Electromagnetic, Transient Heat, and Microsoft Excel modules are integrated to determine the optimal geometry of the device. Next, the design is experimentally validated on a custom-built test setup in the LSSL of UNR. All of these aspects of the design and test will be discussed in the next chapters.

1.6. Dissertation Organization

The dissertation is organized as five chapters. Chapter 2 describes the design of BLS-CMRDs. First the working principle of BLS-CMRDs is explained. Then the analytical and finite element modeling are presented. Finally the optimization procedure to achieve the given system requirements is discussed.

Chapter 3 explains the fabrication of the device and experimental setup, and presents the test program. First the fabrication and assembly processes of the device are presented. Then the experimental setup is described in detail. Finally, the testing procedure is described.

The experimental results are presented and synthesized in Chapter 4. Then the dynamic behavior of the BLS-CMRD is modeled with the analytical modeling presented in Chapter 2, and the discrepancies between the model and experimental data are discussed.

Chapter 5 concludes the dissertation with a summary of the work, conclusions, and suggested future work.

CHAPTER 2 DESIGN OF A BI-LINEAR LIQUID SPRING, CONTROLLABLE MAGNETORHEOLOGICAL DAMPER

2.1. Introduction

The BLS-CMRD consists of a cylinder that has two chambers, i.e., top and bottom, separated by a sealing system, a shaft with a piston, two caps to close the two chambers, and four external rods to fasten the caps against the cylinder (Figure 2.1*a*). The top chamber is filled with MRF-132DG, while the bottom chamber is filled with pure silicone oil. The piston is housed in the top chamber, and there is a small annular gap between the piston and the inner wall of the cylinder. The piston splits the top chamber into Chamber 1 and 2. When the shaft moves downward, the MR fluid in Chamber 2 flows into Chamber 1 through the annular gap, and vice versa when the shaft moves in the opposite direction (Figure 2.1*b*). The flow of MR fluid through this narrow channel causes viscous energy dissipation and thus, a viscous damping. The piston has three separate copper coils. When the coils are energized, an electromagnetic field is developed in the flow gap, which activates the MR fluid and generates a controllable MR damping in addition to passive viscous damping (Figure 2.1*c*). The shaft sections before and after the valve piston have different diameters to achieve the spring effect in this chamber in the rebound mode, i.e., when the piston moves upward. Regarding the bottom chamber, a downward extension of the shaft produces a spring effect in the compression mode.

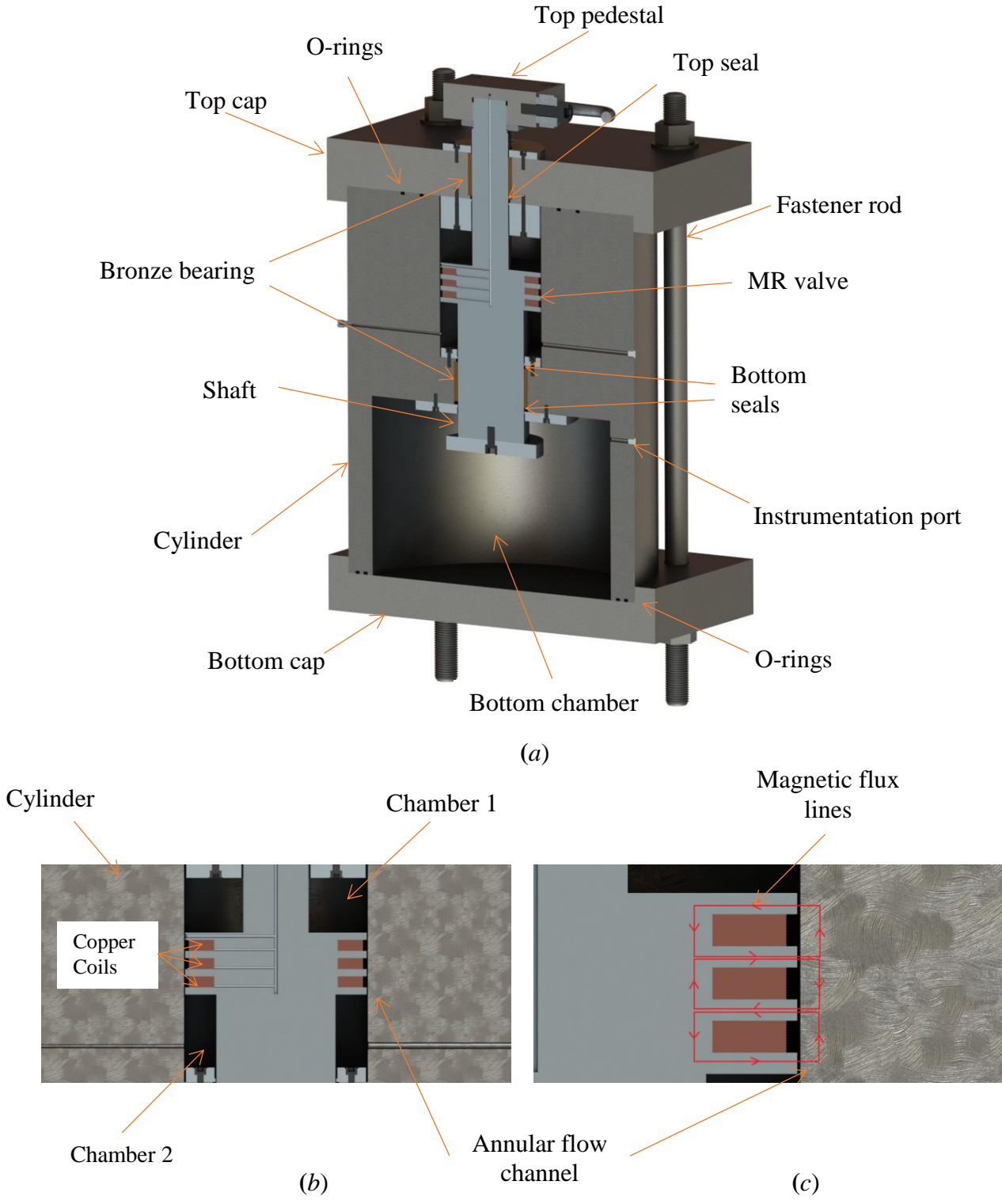


Figure 2.1. (a) Cut-out view of the BLS-CMRD, (b) close up view of the MR valve, and (c) right half of the MR valve showing the magnetic flux lines and flow gap.

For the purpose of this study, a 1/4th scale BLS-CMRD was designed, built, and tested. The design requirements are listed in Table 2.1 and discussed as follows. The design frequency (based on the target natural frequency of vertical isolation), $f = 4$ Hz, and the stroke, $X = 2.54$ cm, of the device are determined from selected earthquake motions in the literature by considering the trade-offs between the different displacements and accelerations. The device is designed for different stiffnesses in compression and rebound. The compression stiffness, k_c , and the rebound stiffness, k_r , are calculated to be 60,000 N/cm and 240,000 N/cm, respectively. The rebound stiffness is higher than the compression stiffness to prevent the structure from overturning during rocking mode. The device is designed for a viscous damping ratio, ζ , between 0.15 ~ 0.20, to ensure that it provides adequate damping in the fail-safe mode.

Table 2.1. Design requirements for the BLS-CMRD.

Static mass, m	9,459.73 kg
Frequency, f	4 Hz
Stroke, X	2.54 cm
Compression stiffness, k_c	60,000 N/cm
Rebound stiffness, k_r	240,000 N/cm
Viscous damping ratio, ζ	0.15 ~ 0.20
Shear force, F_S	27,840 N
Allowable shear deformation, x	≤ 1.524 mm
Minimum structural factor of safety (FOS)	≥ 2
Dynamic range, D	> 2.5

Recall that for 3D isolation, the BLS-CMRD devices are stacked together along with the traditional elastomeric bearings that are currently used to absorb the horizontal

ground motions (Figure 1.6). In the occasion of an earthquake, the device is exposed to not only vertical excitations, but also transmits the lateral force demand of the structure as a shear force in the direction perpendicular to the shaft. In order to maintain the rigidity of the BLS-CMRD to pass the shear force between the building structure and the ground, the allowable shear deformation of the device is determined to be less than 1.524 mm based on the deflection to free length ratio of the shaft ($d/L < 0.02$). These high shear forces pose several major design challenges. The device has to be able to carry the given amount of shear force without a yield or fracture. Even in the elastic region, transmitting the shear force to the shaft may produce uneven stresses on the seals that could lead to leakage and result in a premature failure of the device. The performance of the device in shear will be evaluated as part of the experiment.

To ensure structural safety, the minimum structural factor of safety (FOS) is selected to be 2 against yielding for any component of the BLS-CMRD. The most critical component is the shaft since it is exposed to high shear loadings. In addition to ensuring that the shaft stays in the elastic region against the shear load, the shear deformations on this part are minimized whenever possible to reduce the stresses on the seals. Dynamic range, D , is a measure of the performance of an MR damper. It is described as the ratio of the total damper force to the uncontrollable damping forces, and given by [9],

$$D = \frac{F_{\text{damper}}}{F_{\text{uncontrollable}}} = \frac{F_{\text{MR}} + F_{\text{viscous}} + F_{\text{seal}}}{F_{\text{viscous}} + F_{\text{seal}}} = 1 + \frac{F_{\text{MR}}}{F_{\text{viscous}} + F_{\text{seal}}} \quad (2.1)$$

The dynamic range, D , for BLS-CMRD is target to be greater than 2.5 at the design frequency and stroke when the magnetic field is saturated.

The design of the device involves both analytical and simulation modeling. The sizes of the top and bottom chambers, and the shaft are determined through analytical modeling of bi-directional liquid spring force according to the compression and rebound stiffnesses given in Table 2.1. Then, the seal friction force is added to the spring force. After that, the fail-safe viscous damping force is modeled according to the damping ratio listed in Table 2.1. Lastly, the MR damping force is modeled in accordance with the dynamic range given in Table 2.1. The viscous and MR damping are related to each other, and both determine the dimensions of the MR valve (Figure 2.1*b*). However, MR damping depends on the magnetic flux density developed in the flow gap. Although there are analytical formulations to obtain the magnetic flux density in the flow gap, they are very general and the results might not be accurate. Better predictions could be obtained via computer simulations. In addition, the allowable shear deformation and minimum FOS given in Table 2.1 could be best determined through a structural analysis aided by software packages. The design methodology is illustrated in the schematic in Figure 2.2. Analytical and finite element modeling are discussed in Section 2.2 and 2.3, respectively. To achieve all these design requirements, a comprehensive optimization program is developed in Ansys platform. The optimization process is discussed in Section 2.4. The significant geometric design parameters used in analytical and finite element modeling are shown in Figure 2.3.

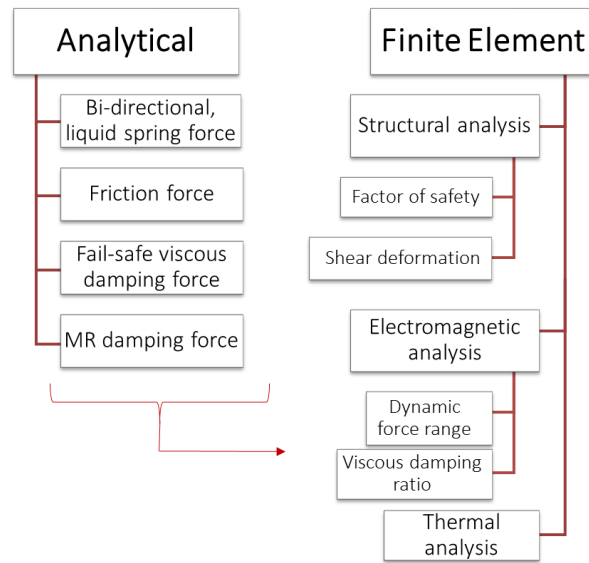
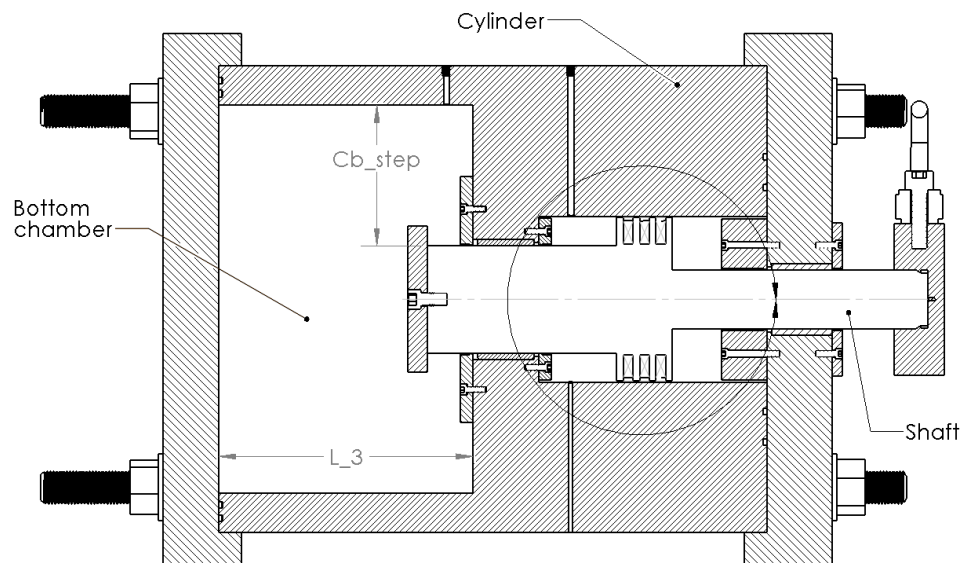


Figure 2.2. Design methodology for the BLS-CMRD.



(a)

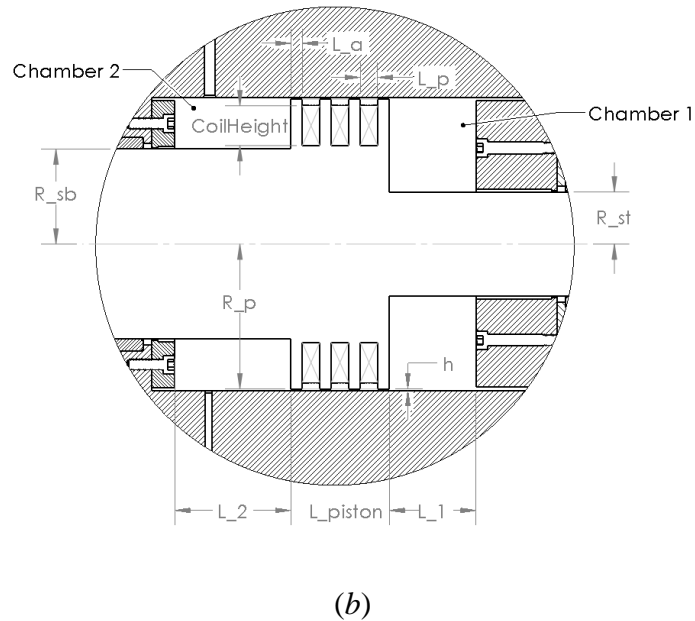


Figure 2.3. Significant geometric design parameters: (a) 2D cross-section of the device and (b) detail view of the top chamber.

2.2. Analytical Modeling

The total force of the BLS-CMRD is given as the summation of the bi-linear liquid spring, seal friction, fail-safe viscous damping, and controllable MR damping forces. Each of these forces will be discussed in this section. The representative force vs. displacement graphs are plotted based on the optimized material and geometric parameters, which are given in Section 2.4.

2.2.1. Modeling of a Bi-directional, Bi-linear Liquid Spring

In mechanics, for a coil spring, spring force is defined as the multiplication of a spring constant (or rate) and displacement of the spring. For liquid springs, however, the spring force is described as the multiplication of a spring rate and displacement of the

spring shaft into the spring chamber. The spring rate is a function of material and geometric parameters as given in Eq. (1.1), repeated here for convenience [40], [83],

$$k_i = \beta \frac{A_{s,i}^2}{V_i} \quad (2.2)$$

where β is the bulk modulus of the working fluid, $A_{s,i}$ and V_i are the cross-sectional area of the shaft and the volume of the fluid in specific chambers, respectively. If there is initial pressurization in specific chambers, then the total spring force can be written as the summation of the spring force and hydrostatic pressure force on the shaft,

$$F_{\text{spring}} = k_i x_{s,i} + P_i A_{s,i} \quad (2.3)$$

where P_i is the initial pressure in specific chambers. Figure 2.4 shows a graphical representation of the spring force for the stroke of 0.0254 m. The bi-linearity is achieved by using different values for the bulk moduli, and the shaft and chamber dimensions in the top and bottom chambers, which are given in Table 2.2.

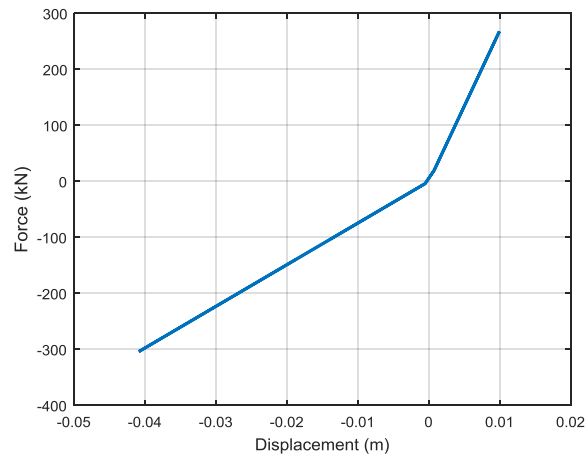


Figure 2.4. Force vs. displacement curve of bi-directional, bi-linear liquid spring.

2.2.2. Modeling of Seal Friction

The friction force in a BLS-CMRD comes from the mechanical friction between the seals and shaft. In the current design, the top and bottom chambers are sealed from each other with two seals on either end of the bottom bearing, whereas the top chamber is sealed from the outer environment via one seal on the bottom side of the top bearing. The seal lips have to be in contact with the shaft at all times during operation. The seals are designed in a way that when the pressure of the liquid in a specific chamber increases, the seal lip presses on the shaft more firmly resulting in an additional friction force. This behavior of the seals can be characterized by splitting the total friction force into two components: quasi-static and dynamic frictions,

$$F_{\text{friction}} = F_f + F_{f,d} \quad (2.4)$$

The constant quasi-static friction force, F_f , can be determined experimentally by testing the device under quasi-static loading conditions, i.e., at very low speeds avoiding the inertial effects. The dynamic seal friction force, $F_{f,d}$, is given as,

$$F_{f,d} = \frac{1}{2} A_{\text{sl}} \Delta P \quad (2.5)$$

where A_{sl} is the area of the seal in contact with the shaft, ΔP is the pressure difference across the seal. Since there are three seals, $F_{f,d}$ becomes,

$$F_{f,d} = \frac{1}{2} [A_{\text{sl},1}(P_1 - P_a) + A_{\text{sl},2}P_2 + A_{\text{sl},3}P_{\text{bottom}}] \quad (2.6)$$

where subscript 1, 2, and 3 denote for the seals adjacent to Chamber1, Chamber2, and the bottom chamber, P_a is the ambient pressure outside the device, P_1 , P_2 , and P_{bottom} are the

pressures in Chamber1, Chamber2, and the bottom chamber. Then, the total friction force can be expressed as,

$$F_{\text{friction}} = F_f + F_{f,d} \quad (2.7)$$

The total force of the device at this stage of the design becomes the summation of the spring force and seal friction force,

$$F_{\text{device}} = F_{\text{spring}} + F_{\text{friction}} \quad (2.8)$$

Eq. (2.8) is represented in Figure 2.5 for $F_f = 5,500 \text{ N}$ and the stroke of 0.0254 m.

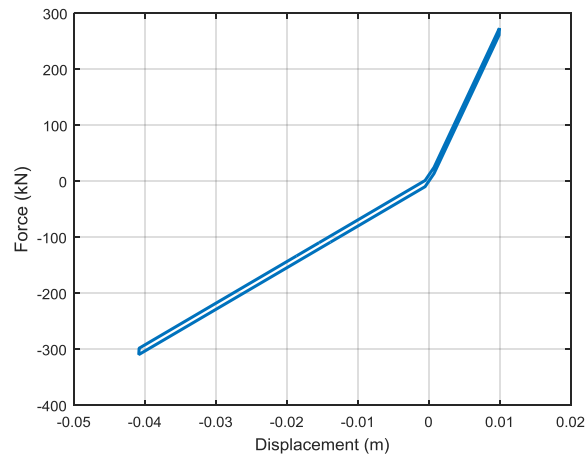


Figure 2.5. Force vs. displacement curve of bi-directional, bi-linear liquid spring with friction force for a sinusoidal input of 0.0254 m.

2.2.3. Fail-safe Viscous Damping

When a magnetic field is not applied, the device works in fail-safe mode as a passive damper. When the piston moves down, the fluid in Chamber 1 flows into Chamber 2 through the annular clearance between the piston and the cylinder wall thereby generating a viscous dissipation (Figure 2.6a, b). When h/D_p is small enough, the flow through two hollow cylinders can be accurately approximated as a flow through

two large parallel plates. This assumption is validated by Table 2.2. The force generated due to the viscous flow through two large parallel plates is well established and is given by [9],

$$F_{\text{viscous}} = \left(1 + \frac{whV_p}{2Q}\right) \frac{12\mu QL_{\text{piston}}A_p}{wh^3} \quad (2.9)$$

where Q is the flow rate through the annular gap between the piston and cylinder wall, h is the height of the flow gap, L_{piston} is the axial length of the piston, w is the mean circumference of the annular flow path, V_p is the piston velocity, A_p is the effective piston area, and μ is the plastic viscosity of the MR fluid. Eq. (2.9) assumes steady flow and constant flow properties.

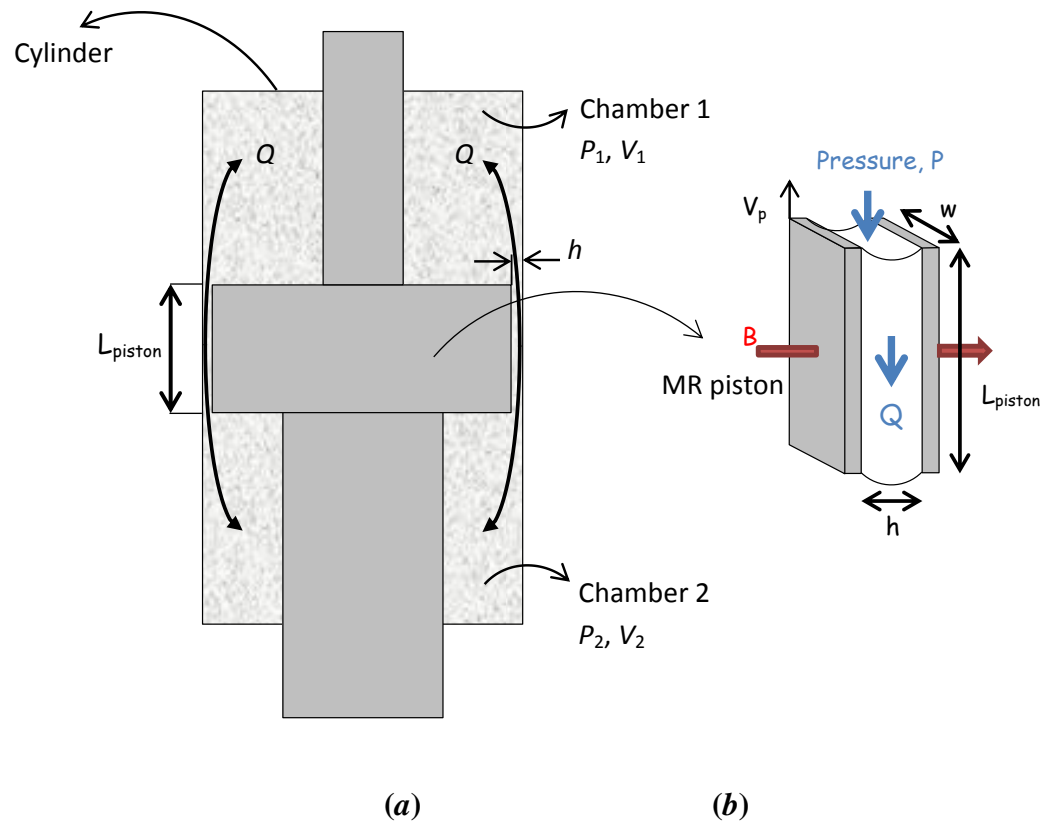


Figure 2.6. (a) Schematic of the MR valve in the top chamber and (b) parallel plate approximation of the flow.

The total force of the device at this stage of the design now becomes the superposition of the spring, seal friction, and viscous damping forces,

$$F_{\text{device}} = F_{\text{spring}} + F_{\text{seal}} + F_{\text{viscous}} \quad (2.10)$$

Eq. (2.10) is represented in Figure 2.7 for a sinusoidal excitation of 0.0254 m at 4 Hz. A careful look at Figure 2.7 would reveal that the force is not symmetric about the x -axis. This is because the effective piston area, A_p is different for compression and rebound modes. There is more flow through the MR valve in the rebound mode than the compression mode.

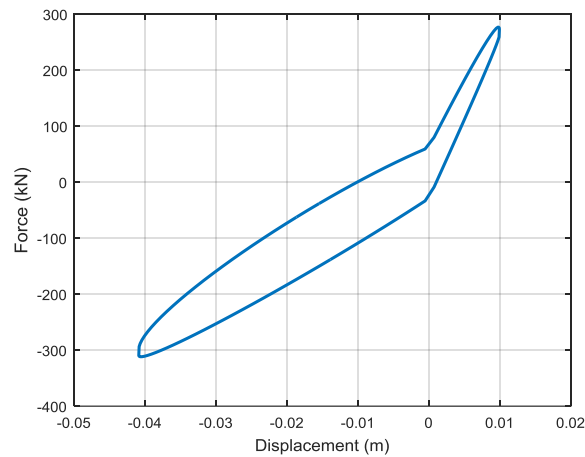


Figure 2.7. Force vs. displacement curve of BLS-CMRD with spring, friction force, and viscous damping forces for a sinusoidal input of 0.0254 m at 4 Hz.

2.2.4. Controllable Magnetorheological Damping

When a magnetic field is applied on MR fluids, they change their state from liquid to semi-solid, and a certain yield stress has to be applied onto the fluid to initiate the flow. Once the flow is initiated, the fluid flows as a viscous fluid. This non-Newtonian behavior of the MR fluids can be well represented with the simple Bingham plastic model effectively, repeated here from Eq. (1.2),

$$\tau = \tau_y + \mu\dot{\gamma}; \quad \tau > \tau_y$$

where τ is the shear stress, τ_y is the yield stress, μ is the plastic viscosity, and $\dot{\gamma}$ is the shear strain rate. τ_y is a function of magnetic field and can be controlled with the intensity of the applied magnetic field. The Bingham plastic model is also depicted in Figure 2.8.

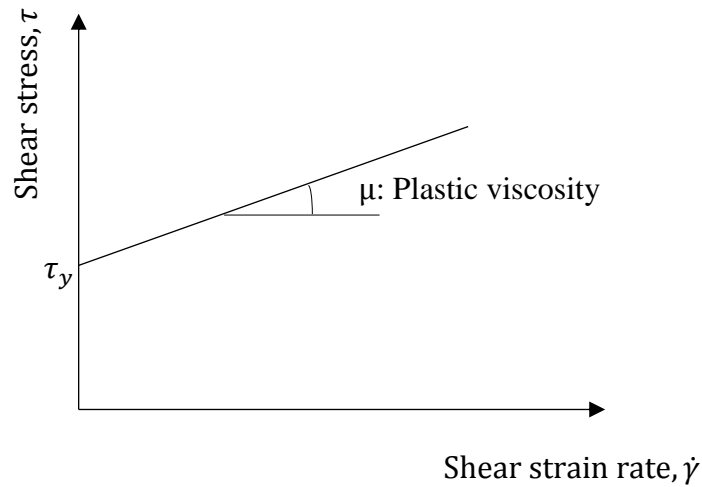


Figure 2.8. Graphical representation of the Bingham plastic model.

The controllable MR force based on parallel plate approximation and Bingham plastic model is given by [9],

$$F_{MR} = \left(2.07 + \frac{12Q\mu}{12Q\mu + 0.4wh^2\tau_y(B)} \right) \frac{\tau_y(B)LA_p}{h} \text{sgn}(V_p) \quad (2.11)$$

Where μ is the plastic viscosity of the MR fluid, Q is the flow rate through the annular gap between the piston and cylinder wall, h is the height of the flow gap, L is the effective axial pole length, w is the mean circumference of the annular flow path, and A_p

is the effective piston area. The total damper force then becomes the superposition of the spring, seal friction, viscous damping, and MR damping forces,

$$F_{\text{device}} = F_{\text{spring}} + F_{\text{seal}} + F_{\text{viscous}} + F_{\text{MR}} \quad (2.12)$$

and is plotted in Figure 2.9 for a sinusoidal excitation of 0.0254 m at 4 Hz and 1 A applied current. The curve is not symmetric about the x -axis as in Figure 2.7 and unsymmetrical forces become more apparent. This is because the effective piston area in Eq. (2.11) contributes to the unequal forces in compression and rebound modes.

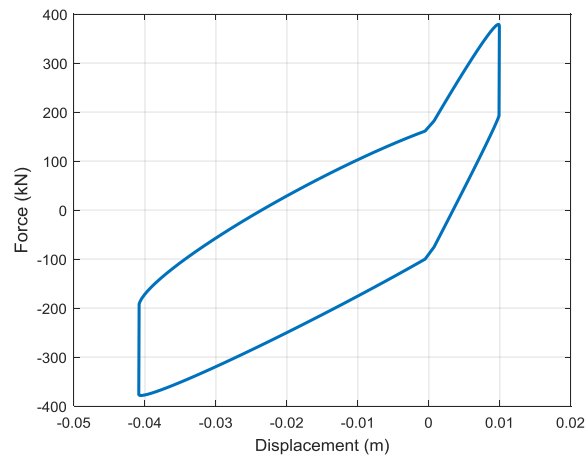


Figure 2.9. Force vs. displacement curve of BLS-CMRD with spring, friction force, viscous, and controllable MR damping forces for a sinusoidal input of 0.0254 m at 4 Hz, and 1 A.

The modeling procedure presented here is employed to model a large-scale MR damper in the literature. Yang et al. [9] modeled a 20 ton-capacity MR damper by using the formulations given in Eqs. (2.7), (2.9), and (2.11). That device did not include a liquid spring and the friction force was given as a constant seal friction. Under these considerations, the same force levels are achieved by using the Eqs. (2.7), (2.9), and (2.11) and implementing their damper specifications. The comparison is shown in Figure

2.10. Figure 2.10a shows the experimental data, while Figure 2.10b shows the model data. This quick check ensures that the modeling procedure for the damping force discussed here is accurate.

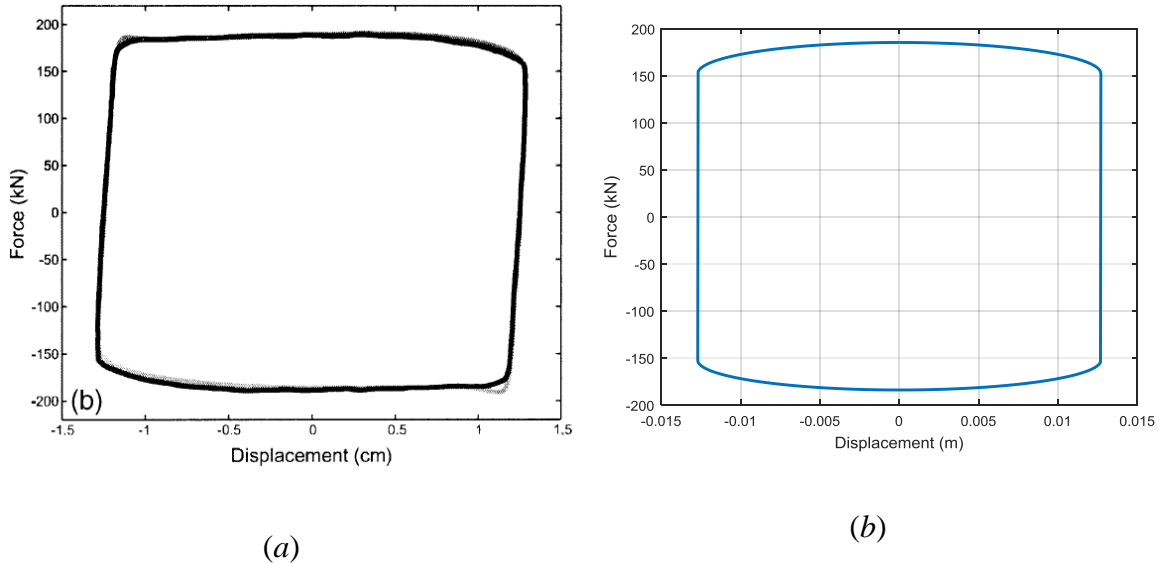


Figure 2.10. (a) Experimental result given in Yang et al. [9] for 1 Hz, 0.0127 m displacement excitation with constant current input of 2 A and (b) theoretical result obtained by using Eqs. (2.7), (2.9), and (2.11) and the same displacement input.

2.3. Finite Element Modeling

The design of the BLS-CMRD involves finite element modeling in addition to the theoretical modeling discussed in Section 2.2. This section discusses the structural, electromagnetic, and thermal analyses. The model geometries here are drawn based on the optimized geometric parameters listed in Section 2.4. The model was updated iteratively during the design process to reach the design targets.

2.3.1. Structural Analysis

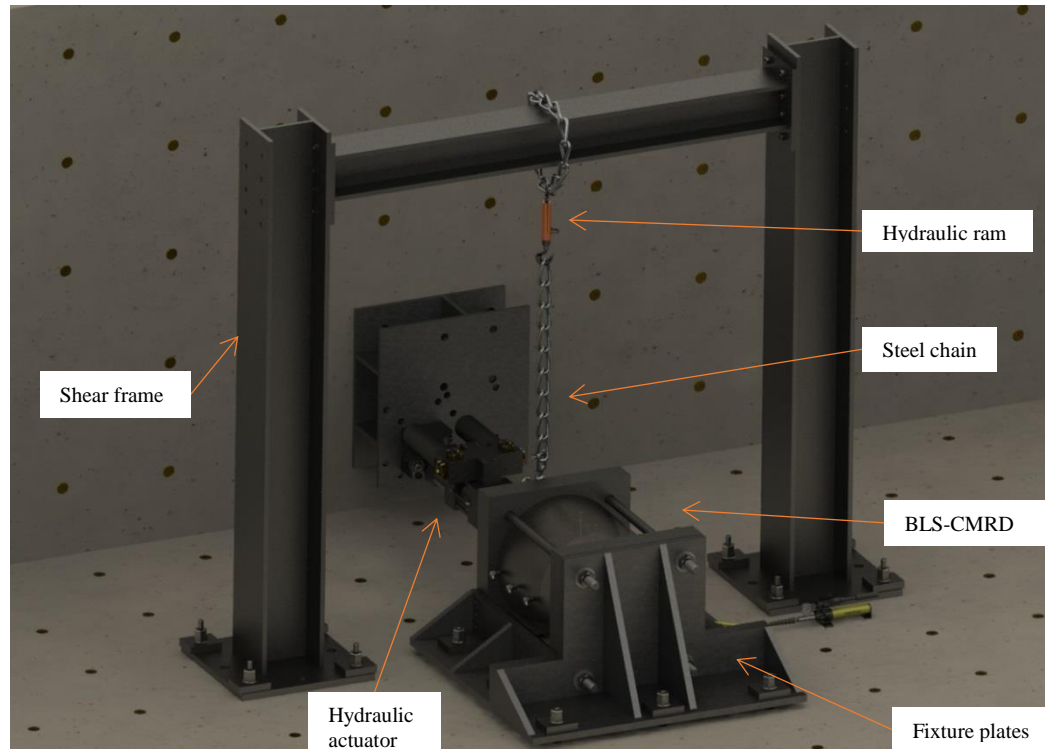


Figure 2.11. 3D design model of the test setup with its main components.

Three-dimensional (3D) structural Finite Element Analysis (FEA) of the BLS-CMRD – subjected to loads and boundary conditions imposed by the experimental setup – is performed by using ANSYS software. Figure 2.11 shows a 3D modeling of the experimental setup where the BLS-CMRD will be tested. The axial and shear loadings are applied as shown via a hydraulic actuator and a hydraulic pulling ram, respectively. This section discusses the structural analysis performed to achieve the structural FOS and allowable shear deformation that are given in Table 2.1.

Figure 2.12 shows a 3D model of the BLS-CMRD, which is imported into the ANSYS Static Structural module. Because the assembly is symmetric, analyses are

applied to a model of half of the system with appropriate boundary conditions. The geometry is then cleaned up from small holes, chamfers, and rounded edges to achieve a high quality meshing. The model is further reduced according to the regions of stress concentrations to save on computer resources and computational times.

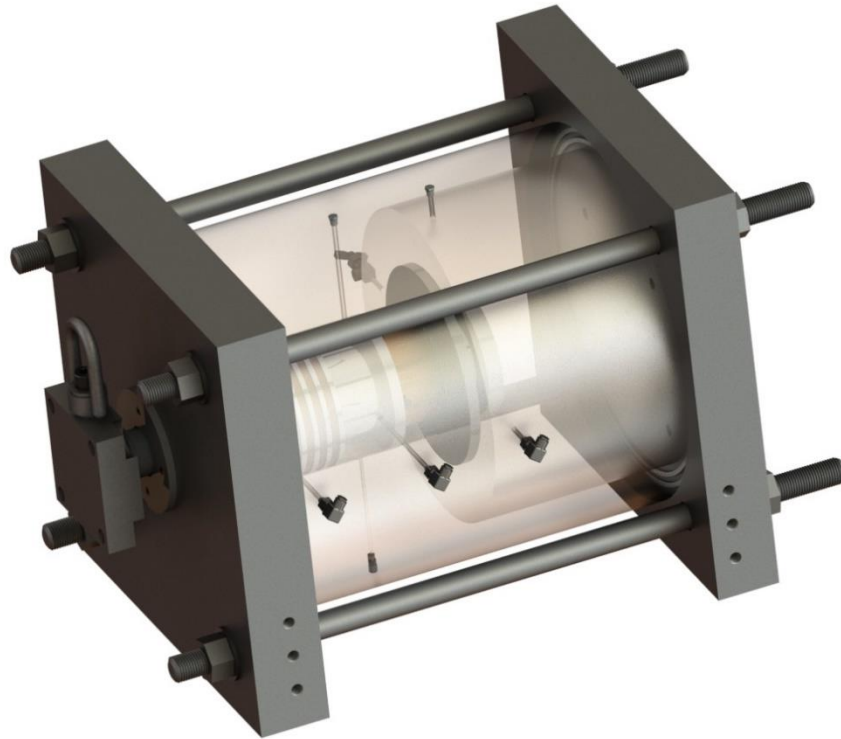


Figure 2.12. 3D model of the BLS-CMRD. The cylinder is made transparent to show the inside of the device.

After the geometry clean-up, a corresponding material is assigned to each part. AISI 1018 steel is selected for the shaft and cylinder due to its good magnetic properties and availability in the market. The top cap, top pedestal, and shaft stopper are made from A36 (mild steel) due to its vast availability in the market.

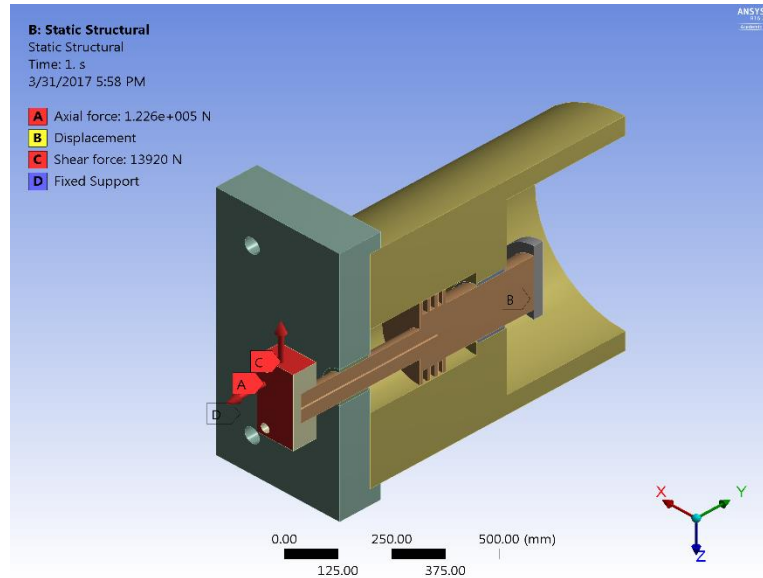


Figure 2.13. ANSYS FEA model with loading and boundary conditions.

To avoid additional lubrication that would require oil grooves, the bearings are made from oil-impregnated sintered bronze alloys. The bottom bearing is selected to be Oilite bronze® (SAE 841) because the force demand to this bearing is relatively small. The top bearing is, however, chosen to be Super Oilite® (SAE 863) as it is subjected to high compression stresses from the vertical shear loading. Typical mechanical properties of Oilite bearings are given in Figure 2.14a. Super Oilite® has two times higher yield strength in compression than Oilite bronze®. Super Oilite 16®, Excelite TX®, and Excelite HTX® oil-impregnated bronze bearings are alternatives that all offer higher strengths. However, another design criterion for the bearings is the PV factor, where P and V represents the load and velocity, respectively. The bearings have to be compatible with the PV as well as P and V values individually of a specific design. The calculations for PV factors are given in Figure 2.14b. P and V values for the BLS-CMRD are calculated to be 480 psi and 80 sfm, respectively.

TYPICAL PROPERTIES* OILITE BEARING MATERIALS			
PROPERTIES	OILITE BRONZE†	SUPER OILITE	SUPER OILITE 16
Composition — Percent			
COPPER	87.2 - 90.5	18.0 - 22.0	18.0 - 22.0
IRON	1.0 MAX	BALANCE	BALANCE
LEAD	—	—	—
GRAPHITE	0 - 0.3	—	0.6 - 1.0
TIN	9.5 - 10.5	—	—
ACID INSOLUBLES (MAX.)	—	—	—
MAGNESIUM	—	—	—
TOTAL OTHER ELEMENTS (MAX.)	1.0	2.0	2.0
BALANCE	—	—	—
Physical & Mechanical Properties			
DENSITY (GM PER CU. CM.)	6.4 - 6.8	5.8 - 6.2	6.0 - 6.4
POROSITY (% OIL BY VOLUME)	19 MIN.	19 MIN.	15 MIN.
"K" STRENGTH CONSTANT	26,500	40,000	60,000
ELONGATION (% IN ONE INCH)	1	1	0.5
YIELD STRENGTH IN COMP. (PSI)**	11,000	22,000	40,000
Comparable Specifications			
ASTM	B-438-05 GR 1 TYPE II	B-439-07 GR 4	B-426 GR 4 TYPE II
MILITARY	MIL-B-5687D TYPE 1 GR. 1	MIL-B-5687D TYPE 2 GR. 4	—
MPIF	CT-1000-K26	FC-2000-K30	N/A
SAE — NEW OLD	841 TYPE 1 CLASS A	863 TYPE 3	—

*Bearings may exhibit appreciable differences in properties due to size, shape, thickness, etc.
**For .001" permanent set on test specimens 1-1/4" diameter by 1" long.

(a)

LOADS AND SPEEDS

The best method for evaluating the acceptability of Oilite bearings for any given application is by using PV factor (Pressure x Surface Velocity) where:

P = the load in (psi) on the projected bearing area (Bearing ID x Length).

V = surface velocity of the shaft in feet per minute (SFM).

$$PV = \frac{W}{LD} \times \frac{\pi DN}{12} = \frac{3.14 WN}{12L}$$

W = total load on bearing (pounds)

L = bearing length (inches)

D = ID of bearing (inches)

N = shaft speed (rpm)

MATERIAL	NORMAL UPPER LIMITS FOR OILITE BEARING MATERIALS			
	PV	P(psi) STATIC	P(psi) DYNAMIC	V (sfm)
OILITE BRONZE	50,000	8,000	2,000	1,200
SUPER OILITE	35,000	20,000	4,000	225
50-16	75,000	50,000	8,000	35

(b)

Figure 2.14. (a) Typical properties and (b) PV values of Oilite bearings[84].

Although Super Oilite 16® provides almost two times higher strength than Super Oilite®, it is not an option because of its lower V value. Excelite TX® and Excelite HTX®, which are not listed here, are not readily available in the market. Manufacturers require large order volumes to supply them. Therefore, Oilite bronze® and Super Oilite® prove to be the best fits for this design.

After the material assignments, the loadings and boundary conditions are assigned appropriately to represent the physics of the device. For the rebound mode, a 122.60 kN axial loading and a 13.92 kN vertical loading are applied on the front and top faces of the top pedestal, respectively. Also, a 14 MPa hydrostatic pressure is applied to the inner

surface of the top chamber (Figure 2.13). Fixed support boundary conditions are applied to the screw holes on the side of the top cap. A displacement boundary condition with $(x,y,z) = (\text{free},0,\text{free})$ is assigned to the shaft stopper. All connections between the parts are modeled properly to reflect the real operating conditions of the device. For instance, because the shaft is oscillating through both the top and bottom bronze bearings, frictional contacts are assigned to the connections between the shaft and the top bronze bearing and the shaft and the bottom bronze bearing with friction coefficient of 0.13. The connections between the bearings and the cylinder are defined as bonded contacts since both bearings are press-fitted to the cylinder. The connection between the cylinder and the top cap is assigned to a frictional contact with a friction coefficient of 0.2. Finally, the connection between the shaft and the top pedestal is assigned to a bonded contact since the top pedestal is screwed on the shaft, and the calculations for this threaded connection are already done analytically.

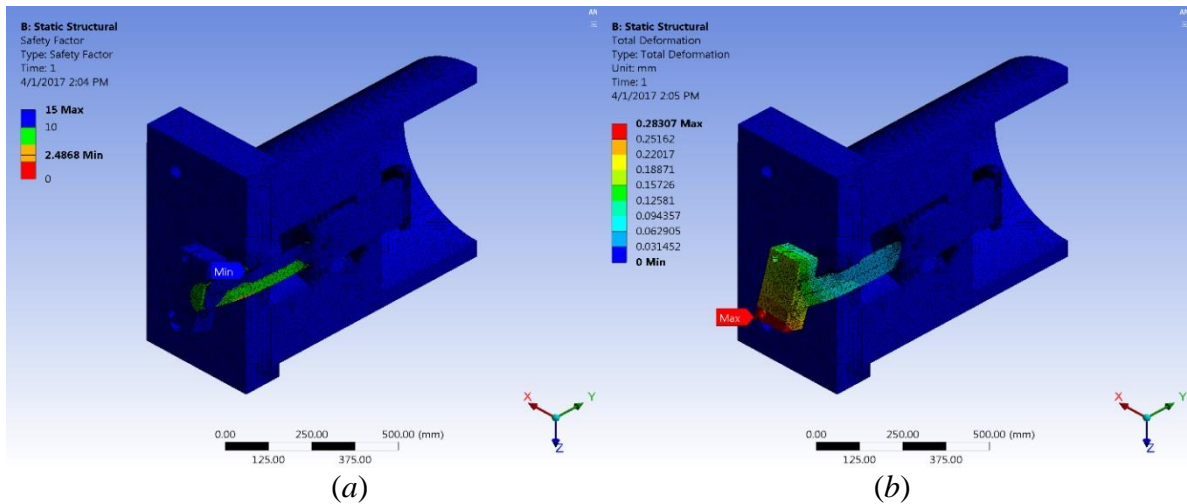


Figure 2.15. FEA results: (a) minimum FOS and (b) maximum total deformation (results are magnified by 310%).

Analysis results are investigated for the minimum FOS over the entire device, and the maximum total deformation on the shaft as per the design requirements (Table 2.1). Figure 2.15 shows the results for the minimum FOS and the total deformation. The minimum FOS occurs on the top bronze bearing where it is compressed against the top cap by the shaft. The maximum total deformation occurs on the top pedestal, and deformation reduces gradually along the shaft axis.

Both results agree with our intuitions. However, as a general rule of thumb, a mesh independency analysis should be conducted to ensure that solutions are converging to a constant as the number of mesh elements is increased. In general, the errors in a FEA might result from user errors, modeling errors, discretization errors, or a combination of these three. In a well-posed problem, where the user and modeling errors are eliminated, as the number of mesh elements increases the energy of the entire model converges to an exact solution. The convergence of energy also ensures the convergence of any particular local response.

ANSYS has a built-in tool to perform a mesh independency analysis. It allows the user to input an allowable change (in percentage) for a particular response. After each trial, it automatically identifies the regions that require mesh refinement based on the structural error information and increases the number of elements in those particular regions. For each refinement, a new trial is executed and a corresponding response is calculated. If the change between two successive computed responses is less than the allowable change, then the mesh refinement is aborted and the solution is said to be mesh independent. For this particular analysis, the allowable change is set to 1% for the strain

energy of the entire model. Once the strain energy has converged, the minimum FOS and the maximum shear deformation are interpreted from the converged solution. Figure 2.16 shows the convergence history of the strain energy for the FEA of the model shown in Figure 2.13. After the mesh independency analysis, the minimum FOS is determined to be 2.48 on the top bronze bearing and the maximum shear deformation on the shaft is found to be 0.21 mm.

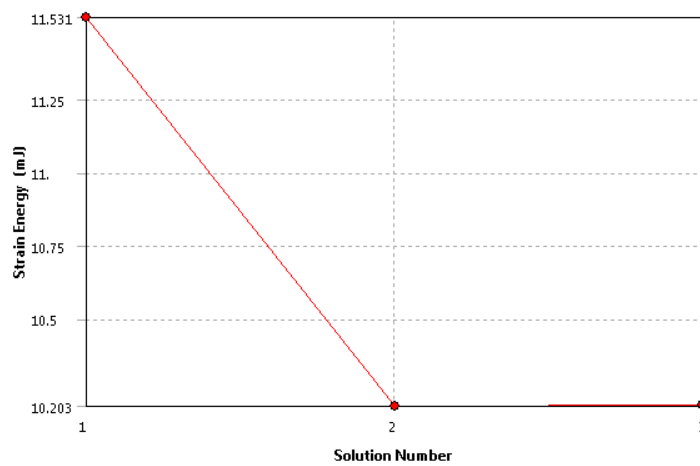


Figure 2.16. Convergence history of the strain energy for the FEA analysis of the model shown in Figure 2.13.

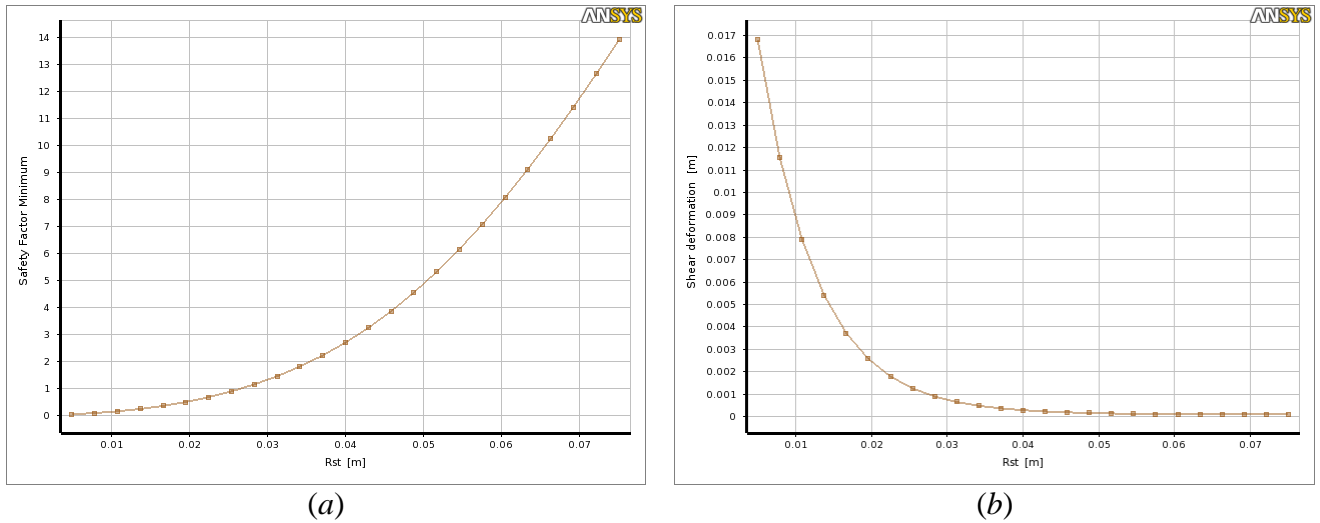


Figure 2.17. Variations of the minimum FOS and maximum shear deformation with the radius of the top shaft.

During the structural analysis, a parametric study is conducted to investigate the variations of minimum FOS and maximum shear deformation with the geometric dimensions of the device. The radius of the shaft, R_{st} , is found to be the controlling parameter for both FOS and maximum shear deformation (Figure 2.17). As the radius of the shaft is increased, the FOS is observed to increase, while the maximum shear deformation is seen to decrease exponentially.

2.3.2. Electromagnetic Analysis

The MR valve is responsible for generating the required viscous damping ratio, ζ_{viscous} , and also determines the dynamic range, D . In the passive mode, when there is no magnetic field applied to the MR fluid, the valve provides only the passive damping due to the viscous flow of the MR fluid through the flow channel. However, in the semi-active mode, when there is a magnetic field applied to the MR fluid, the valve provides

an additional damping that varies with the intensity of the field. This is often called controllable MR damping. D (Eq. (2.1)) requires the calculation of the controllable MR damping force, F_{MR} , which also requires the information of the dynamic yield stress, $\tau(B)$, of the MR fluid. In order to obtain $\tau(B)$, the magnetic flux density, B , developed in the flow channel has to be known. For an electromagnet, B is given by,

$$B = \mu_0 \left(\frac{N}{L_p} \right) I \quad (2.13)$$

where μ_0 is the magnetic field permeability of the material, N is the number of turns of the coil, L_p is the length of the coil, and I is the current applied to the coil. The MR valve and the representative magnetic flux lines are shown in Figure 2.1*b,c*. For such a complex electromagnet, the magnetic flux density, B , can be best predicted with the help of a computer software. In this study, ANSYS Maxwell module is used to calculate the B in the flow gap. BLS-CMRD is composed of cylindrical components except the top and bottom caps, and top pedestal. Because these parts are square and are also far from the magnetic field region, they can be approximated to be cylindrical without a loss in the accuracy of the analyses. Therefore, the analyses are conducted on a 2D axisymmetric model to save on the computer resources and computational time. The axisymmetric model is shown in Figure 2.18*a,b* with its main components and modeling assumptions. Although the magnetic field is concentrated around the piston, analyses are applied to a model of the entire device to ensure the accuracy based on previous experiences.

The model geometry is drawn in the ANSYS Geometry module and then imported into the Maxwell module. After the geometry is imported, a corresponding material is assigned to each component. AISI 1018 is assigned to the shaft and cylinder,

bronze is assigned to the top and bottom bearings, MRF 132-DG is assigned to the MR fluid, silicone oil is assigned to the bottom chamber, and steel A36 is assigned to all remaining parts. The shaft and the cylinder materials are chosen to be AISI 1018 because of its good magnetic properties. The MR fluid is chosen to be hydrocarbon-based MRF-132DG of Lord Co. The relationship between the magnetic flux density, B , and magnetic field intensity, H , the yield stress, τ , and magnetic field intensity, H , for the fluid is given by the following expressions [85],

$$B = 0.68[1 - e^{(-10.97\mu_0 H)}] + \mu_0 H \quad (2.14)$$

$$\tau = 63,855.60 \tanh(6.33 \times 10^{-6} H) \quad (2.15)$$

where B is in Tesla, H is in A/m, τ is in Pa and $\mu_0 = 4\pi \times 10^{-7}$ T/(A/m) is the magnetic constant.

A rectangular boundary is drawn around the 2D model, and an insulation boundary condition is applied to it. The coils are wound in alternating directions to achieve an overall higher magnetic field in the flow channel. Besides the viscous damping ratio, ζ_{viscous} , and the dynamic range, D , the magnetic flux density in the flow channel is targeted to be 1 T to have the MR fluid reach its magnetic saturation. ANSYS Maxwell accepts current x turns as an excitation input to the coils.

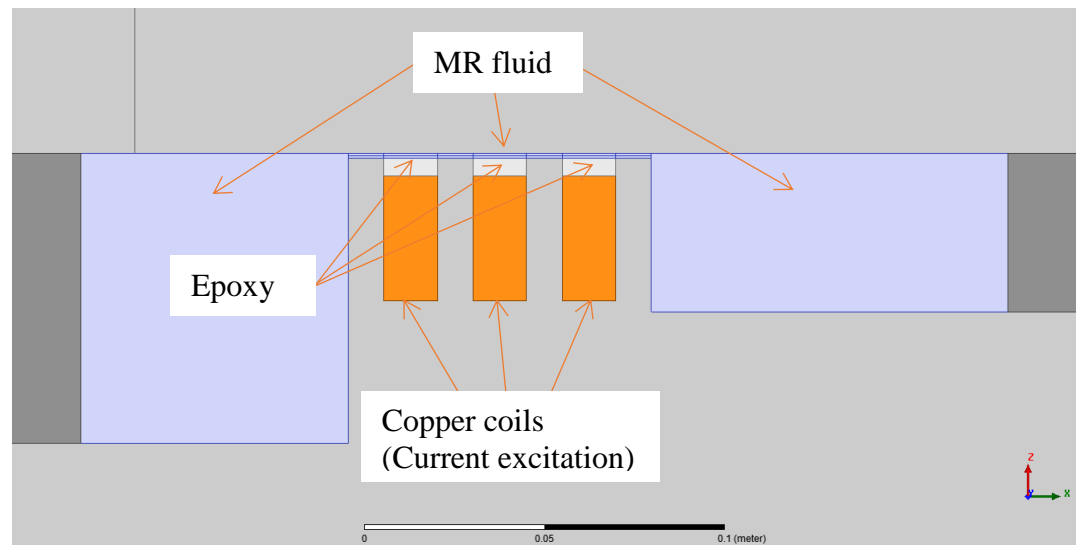
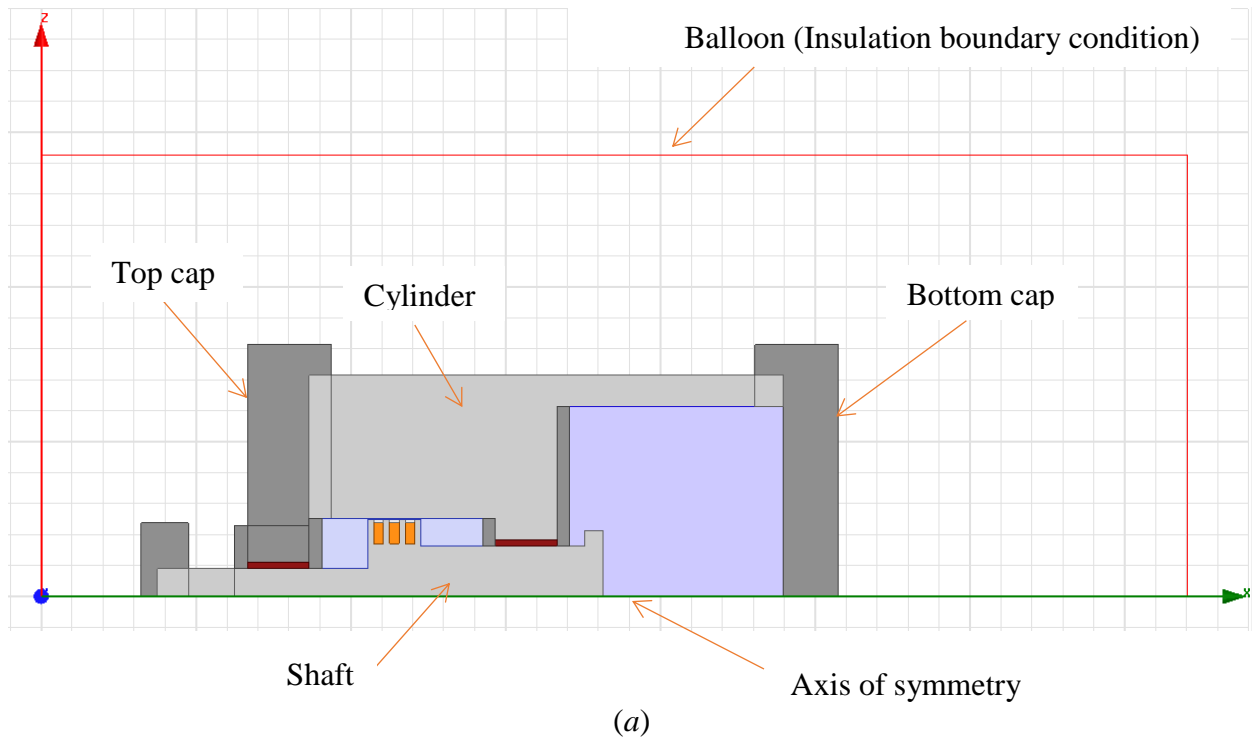


Figure 2.18. (a) Axisymmetric model for the electromagnetic analysis in ANSYS

Maxwell and (b) close-up view of the MR valve.

Figure 2.19 shows the result for magnetic flux density, B , on the MR valve for the current input of 2500 A x turns. The magnetic field develops in the regions of the MR fluid where it is not adjacent to the coils. The lengths of these regions are called active pole lengths (red regions in the flow gap in Figure 2.19), whereas the coil lengths are called passive pole lengths (blue regions in the flow gap in Figure 2.19).

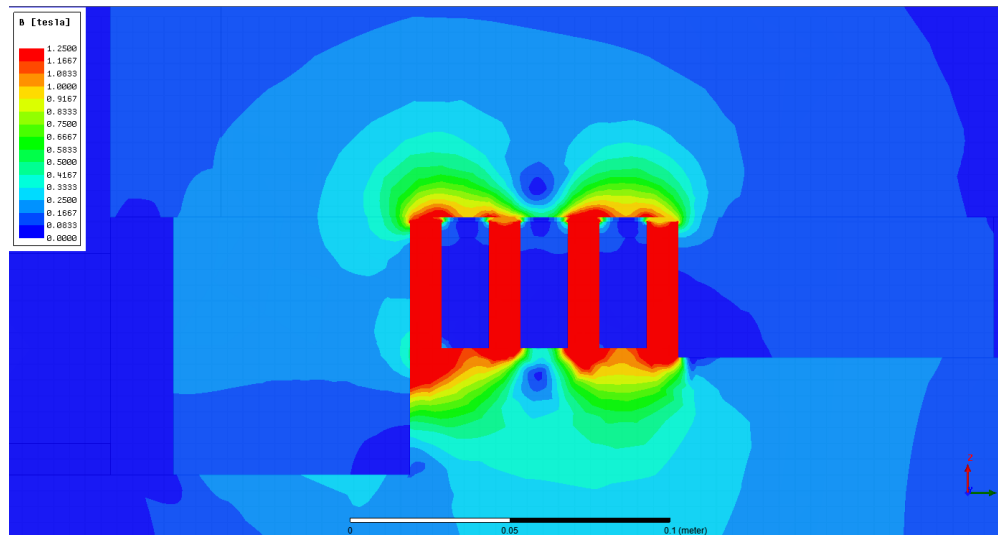


Figure 2.19. Magnetic flux density, B , distribution after an electromagnetic analysis for the current input of 2500 A x turns.

After the electromagnetic analyses, the relationship for the yield stress as a function of the applied current input is obtained as follows,

$$\tau = 44,960 \tanh(1.108I + 0.2893) \quad (2.16)$$

for a coil of 1135 turns, where the τ is in Pa and I is in A.

During the analysis, the effects of the geometric dimensions of the MR valve and the applied current input ($A \times \text{turns}$) on the dynamic range, D , and the viscous damping ratio, ζ_{viscous} , are investigated. Figure 2.20 and 2.21 show the variations of D and ζ_{viscous} with respect to the height of the flow gap, h , active pole length, L_a , passive pole length, L_p , radius of the piston, R_p , and the current input. Each parameter is varied within the range shown in the figures, while the remaining parameters are kept at constant values shown in Table 2.2.

In order to achieve higher D 's, F_{MR} has to be maximized while F_{viscous} is minimized, since F_{friction} is usually constant within a range as suggested by Eq. (2.1). However, as given in Eqs. (2.9) and (2.11), F_{viscous} and F_{MR} are both functions of the height of the flow gap, h , active pole length, L_a , and radius of the piston, R_p . Noting that F_{friction} is constant and keeping all other parameters constant, F_{viscous} increases two orders of magnitude faster than F_{MR} with decreasing values of h , and thus, leads to decreasing D . On the other side, both F_{viscous} and F_{MR} decrease with higher values of h , again decreasing D .

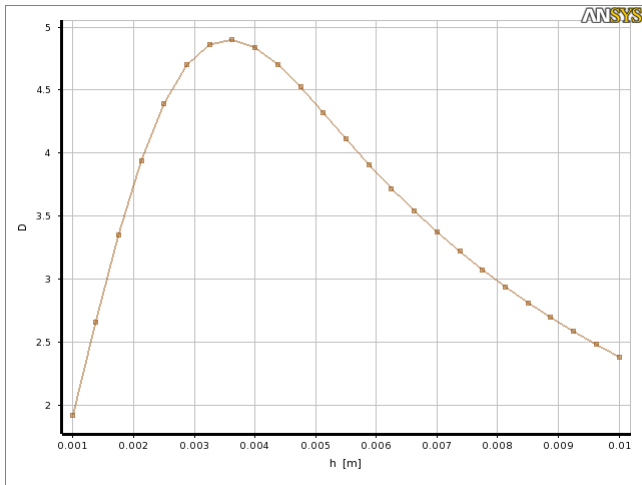
On the other hand, increasing active pole length, L_a , increases F_{MR} and thus, increases D in two ways. First, increasing L_a increases the magnetic field generated in the flow gap, the dynamic yield stress, $\tau(B)$, and eventually increases F_{MR} as $\tau(B)$ is a multiplier in Eq. (2.11). The increase in $\tau(B)$ is limited by the magnetic saturation of the MR fluid. Second, increasing L_a directly increases F_{MR} as L_a is a multiplier in Eq. (2.11). However, it should also be noted that L_a increases the axial length of the piston L_{piston}

and thus, increases F_{viscous} , leading to decreasing D . The variation of D with L_a is shown in Figure 2.20*b*.

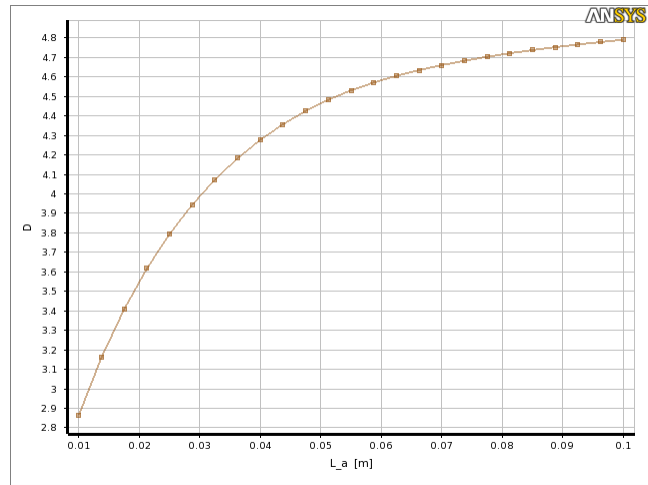
Increasing R_p decreases D because F_{viscous} increases two orders of magnitude than F_{MR} with R_p . Therefore, there must be an optimal combination of h , L_a and R_p to maximize D . The above discussion is illustrated in Figure 2.20*a*, *b*, and *c*.

Increasing current input to the coils increases the magnetic field generated in the flow gap and thus, F_{MR} , leading to increasing D . This increase is limited by the magnetic saturation of the MR fluid. Therefore, increase in D gradually levels off (Figure 2.20*d*).

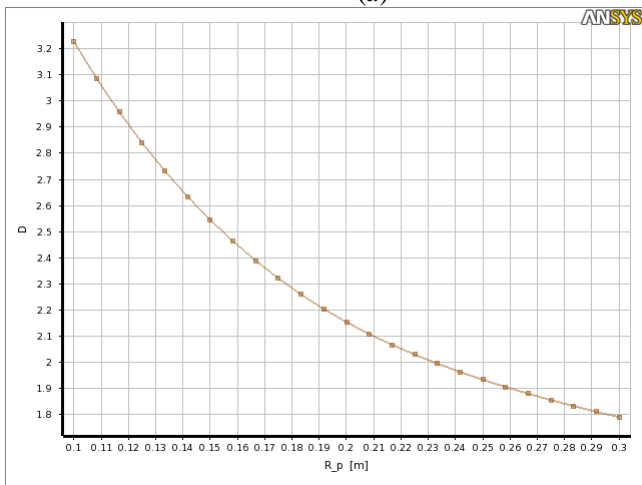
The dynamic force range, D , decreases with the passive pole length (length of the coil), L_p , as shown in (Figure 2.20*e*). This is due to the fact that as L_p increases, the length of the piston increases and thus, F_{viscous} increases resulting in lower D 's.



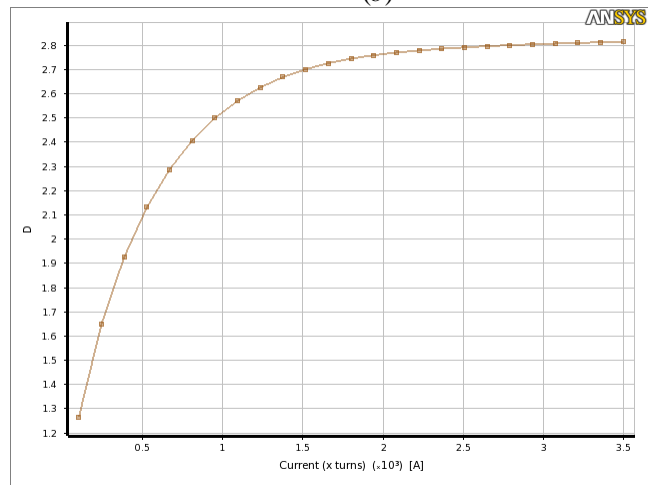
(a)



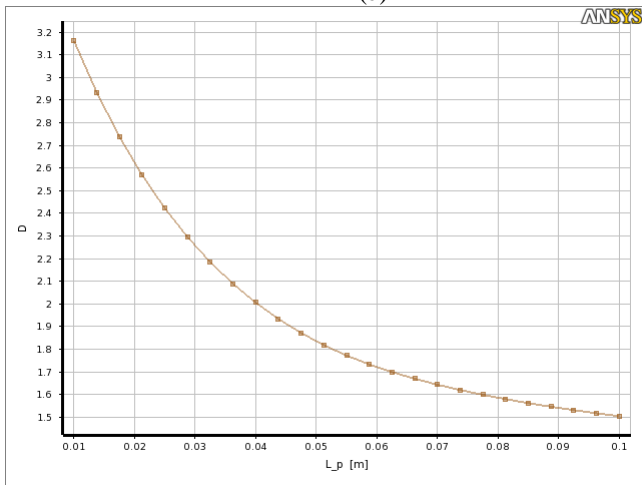
(b)



(c)



(d)



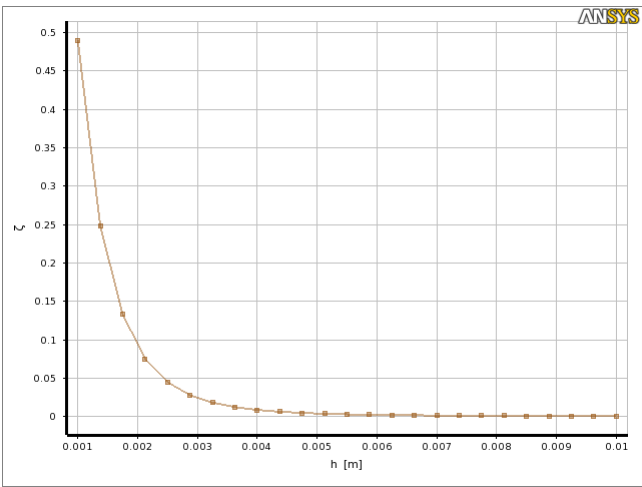
(e)

Figure 2.20. Variation of dynamic force range, D , with respect to the (a) flow gap, (b) active pole length, (c) piston radius, (d) current input, and (e) passive pole length.

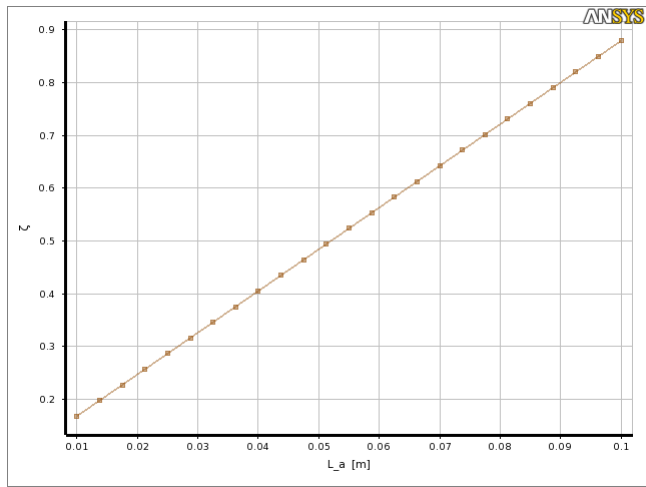
The viscous damping ratio, ζ_{viscous} , is also related to the design of the MR valve. Assuming a simple harmonic excitation, $x(t) = X\sin(\omega_d t)$, ζ_{viscous} is given by,

$$\zeta_{\text{viscous}} = \left(\frac{W}{\pi\omega_d X^2} \right) \left(\frac{1}{2\sqrt{km}} \right) \quad (2.17)$$

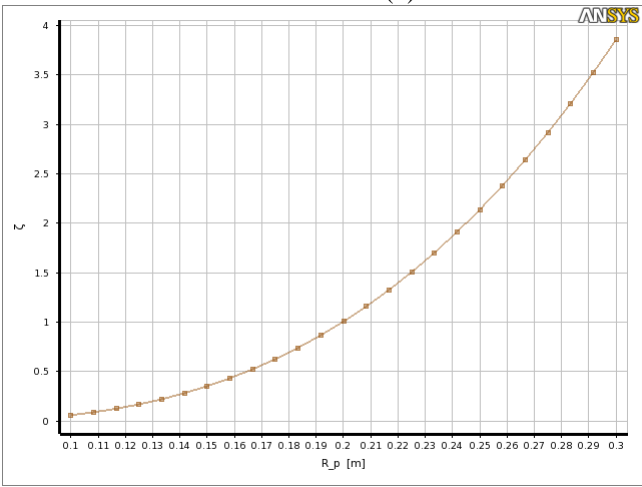
where $W = \int_0^{2\pi/\omega_d} F_{\text{viscous}} dx$, m is the mass, k is the spring constant, ω_d and X are the driving frequency and amplitude of the harmonic excitation, respectively. The effects of h , L_a , R_p , current input and L_p on the viscous damping ratio ζ_{viscous} is also investigated and shown in Figure 2.21. The value of ζ_{viscous} greatly decreases with increasing values of h , as F_{viscous} is inversely proportional to the h (Figure 2.21a). On the other hand, ζ_{viscous} increases linearly with both increasing L_a and L_p , as both parameters increase the axial length of the piston, L_{piston} , which is a multiplier in F_{viscous} (Eq. (2.9)). The effects of L_a and L_p on F_{viscous} are shown in Figure 2.21b, e. ζ_{viscous} also increases with increasing R_p values as shown in Figure 2.21c, since it is a direct multiplier in Eq. (2.9). It is included in both Q and A_p . Finally, ζ_{viscous} is not affected by the applied current because F_{viscous} results from passive fluid friction only (Figure 2.21d). Therefore, there must be an optimal value for h , L_a , L_p and R_p to reach the given target for ζ_{viscous} . The procedures to obtain the optimal values of these parameters are discussed in Section 2.4.



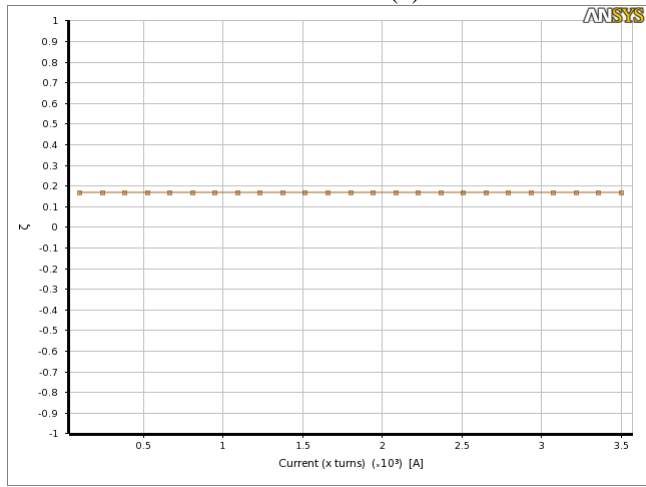
(a)



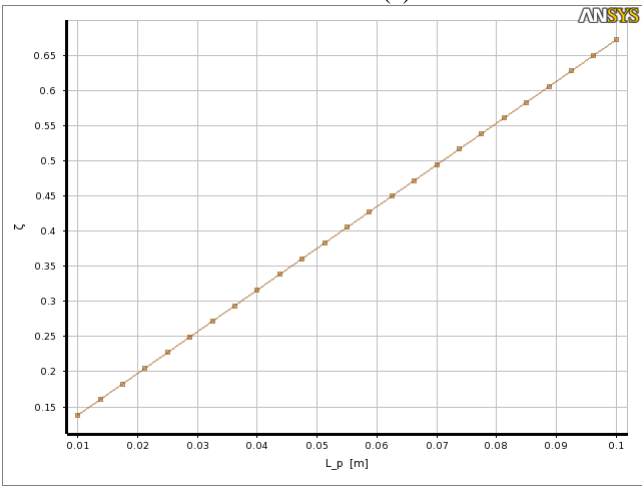
(b)



(c)



(d)



(e)

Figure 2.21. Variations of viscous damping ratio, ζ_{viscous} , with respect to the (a) flow gap, (b) active pole length, (c) piston radius, (d) current input, and (e) passive pole length.

2.3.3. Thermal Analysis

The total energy dissipation by the device can be calculated from the area under a force vs. displacement loop. This energy becomes a heat source to the MR fluid in the top chamber. The heat generation manifests itself as an increase in the temperature of the fluid. The elevated temperatures affect the performance of the BLS-CMRD in several ways. Most importantly, seals might be damaged with increased temperatures. Mckee et al. [80], [81] demonstrated the effects of temperature on the performance of seals. They showed that the seals expanded with increasing temperature, which caused additional compression and thus, deformation on the seals. They reported that the seals failed suddenly and unexpectedly during testing when the temperature was raised to around 80 °C. Also, before the failure occurred, the expansion on the seals caused an increase in the friction force because the seal lips pushed stronger against the shaft. The MR fluid also tries to expand with elevated temperatures which results in pressure buildup inside of the chamber. The added pressures push the seals against the shaft surface more strongly which also causes an increase in the friction force. The temperature rise also affects the properties of the MR fluids. Both the bulk modulus and viscosity of the MR fluid decrease with increased temperatures reducing the stiffness and damping, respectively. Temperature increase is also known to degrade the magnetic properties of the MR fluids. According to Curie's law, the iron particles inside the fluid partially lose their ability to be magnetized.

Electromagnetic heating, produced by the copper coils, is another heat source in the device. When energized, current flows through the copper wires. Although copper has

a high electrical conductivity, there is some resistance to electrical current, causing Ohmic power losses. This phenomenon is also known as Joule-Lenz effect. The Ohmic losses are transformed into heating, which is often called Joule heating. The Joule heating raises the temperature of the coils, as well as the surroundings. As the temperature in the coils rises, the resistance of the wires increases. This requires additional power for the coils to maintain the same magnetic field in the MR fluid. According to Curie's law, the valve piston and the cylinder wall also lose their magnetic properties with increasing temperature. The heat transfer to the piston and the cylinder wall from both the MR fluid and coils consequently reduces the efficiency of the electromagnet. All these considerations have to be taken into account in the design of a BLS-CMRD.

In order to assess the effects of heating on the performance of the BLS-CMRD, a thermal analysis is conducted in ANSYS software. The thermal analysis involves theoretical calculations to determine the heat generation due to viscous dissipation, as well as an electromagnetic analysis to calculate the heat generation from Joule heating. All theoretical calculations are performed in Excel module, whereas the electromagnetic analysis is performed in Maxwell module. The calculated heat sources are then input to the Transient Thermal module. Following the heating analysis, a cooling analysis is conducted to calculate the time required for the MR fluid to cool down to the room temperature to achieve consistency between the tests. During the analyses, the device is considered to operate at its limit conditions, i.e., the maximum stroke, frequency, and applied current, to ensure the maximum heat generation in the device. Figure 2.22 shows the schematic of the program developed in ANSYS.

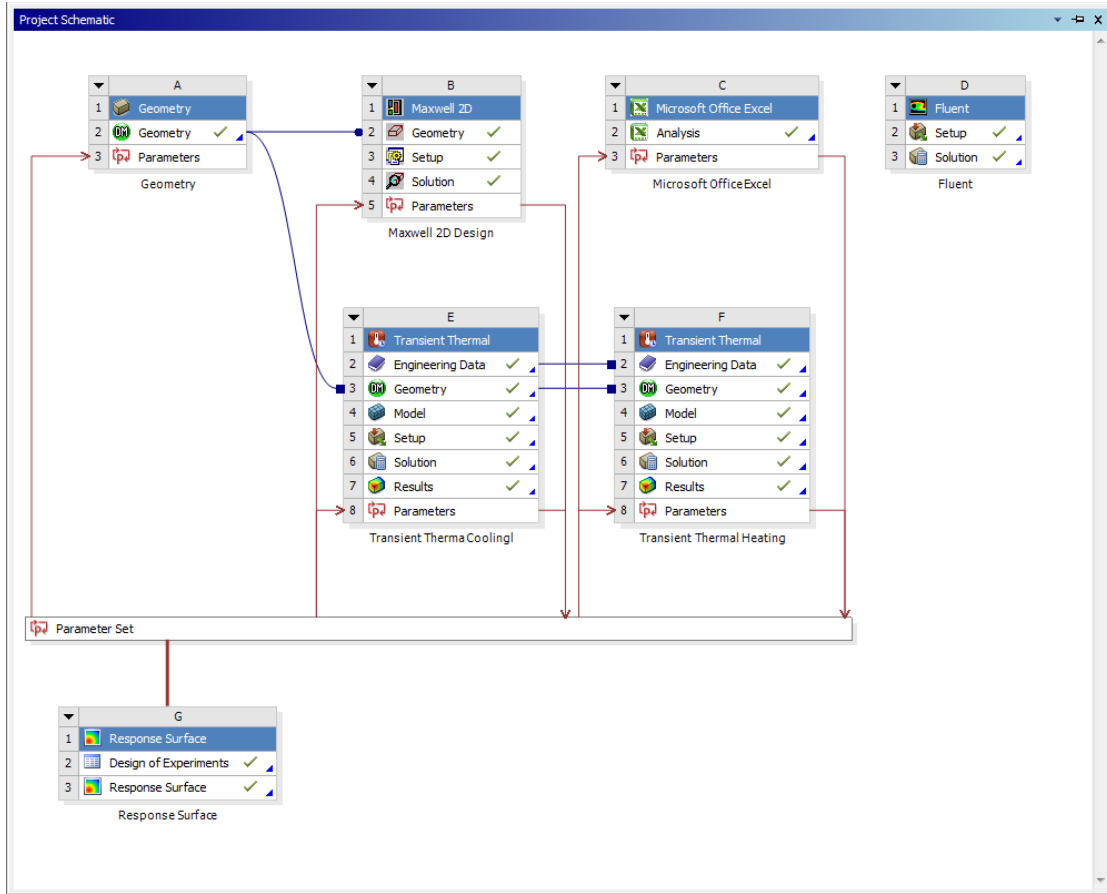


Figure 2.22. Thermal analysis of the BLS-CMRD in ANSYS software.

Figure 2.23 shows the heat loadings and boundary conditions used in the Transient Thermal analysis. Although the top and bottom caps are square, the device is modeled as axisymmetric because the cylinder, shaft, and seal glands are all axisymmetric (Figure 2.1). The total viscous heating is calculated by the superposition of the seal friction, viscous, and MR damping as,

$$W_{\text{total}} = 4F_{\text{friction}}X + \pi F_{\text{viscous}}X + 4F_{\text{MR}}X \quad (2.18)$$

in the Excel module and is input to the Transient Thermal module as a heat source. The calculation of the MR damping force requires the information of the magnetic flux

density in the flow gap. This information is passed to the Excel module from the Maxwell module. The Joule heating is, on the other hand, calculated by the Maxwell module directly and is transferred to the Transient Thermal module. This is verified with the formulation for the Joule heating, $Q = I^2R$, where I is the current applied to the coils and R is the resistance of the coils. The device is to be cooled with a fan at room temperature during the tests. To represent the forced convection, a convection boundary condition with $T_\infty = 22\text{ }^\circ\text{C}$ and $h = 50\text{ W/m}^2\text{ }^\circ\text{C}$ is assigned to all outer surfaces of the device.

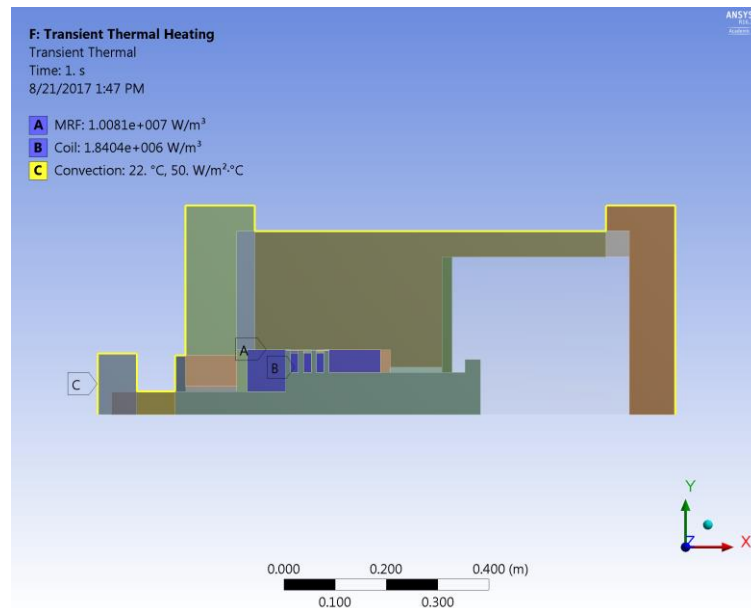


Figure 2.23. Heat loadings and boundary conditions for the Transient Thermal heating analysis.

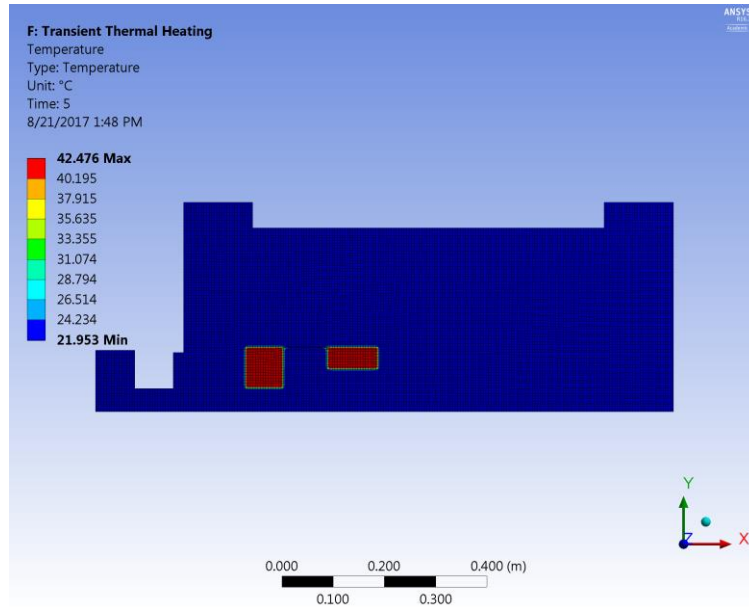


Figure 2.24. Temperature distribution over the device after the Transient Thermal heating analysis.

Figure 2.24 shows the temperature contours after the Transient Thermal analysis at 5 s. The maximum temperature is found to be around 42.5 °C in the centers of Chamber 1 and 2. Because the cylinder wall of the top chamber is too thick (0.23 m), heat is not able to flow out, and becomes mostly trapped in Chamber 1 and 2. Figure 2.25 shows the variation of the maximum temperature in the MR fluid with time for $X = 0.0254$ m, $f = 4$ Hz, and $I = 3500$ A x turns. The maximum temperature increases linearly with time and reaches around 42.5 °C in 5 seconds.

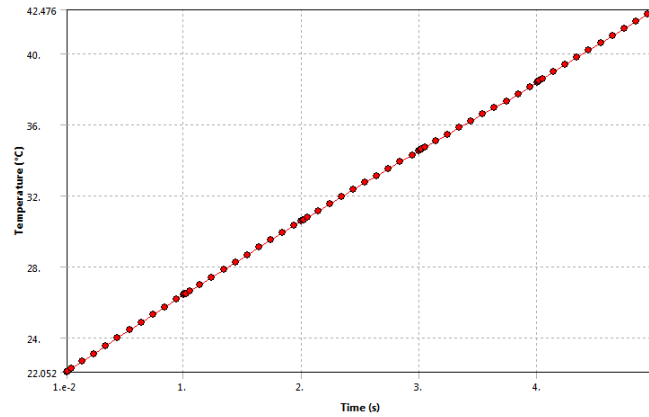
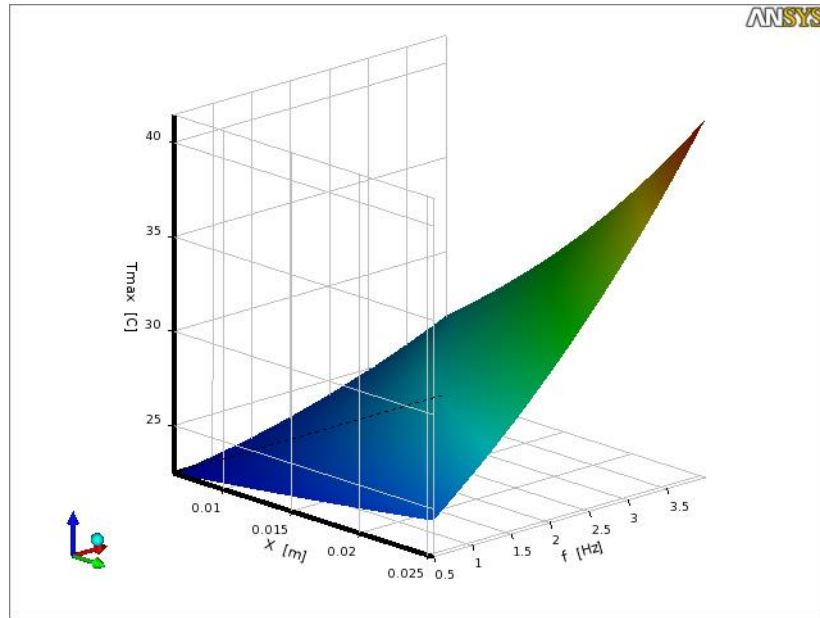
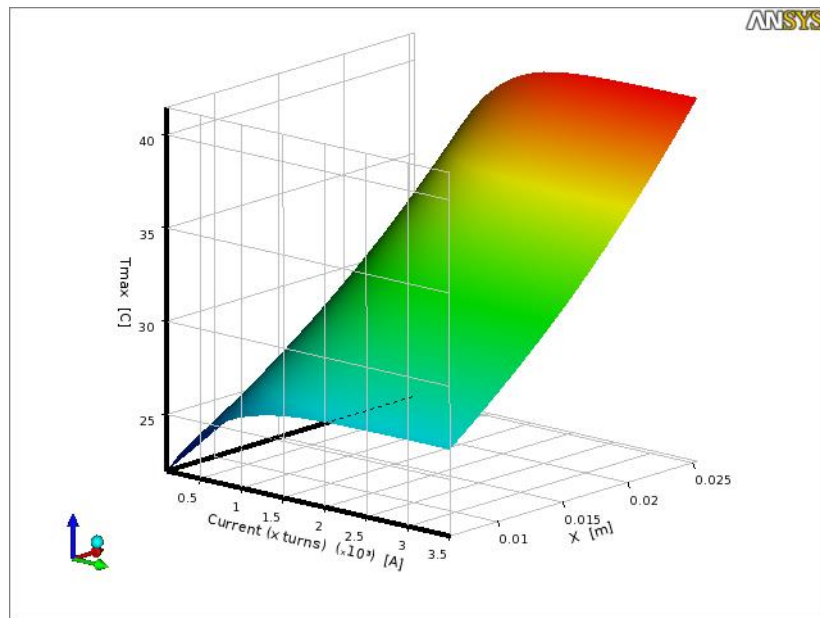


Figure 2.25. Variation of the maximum temperature in the MR fluid with time.

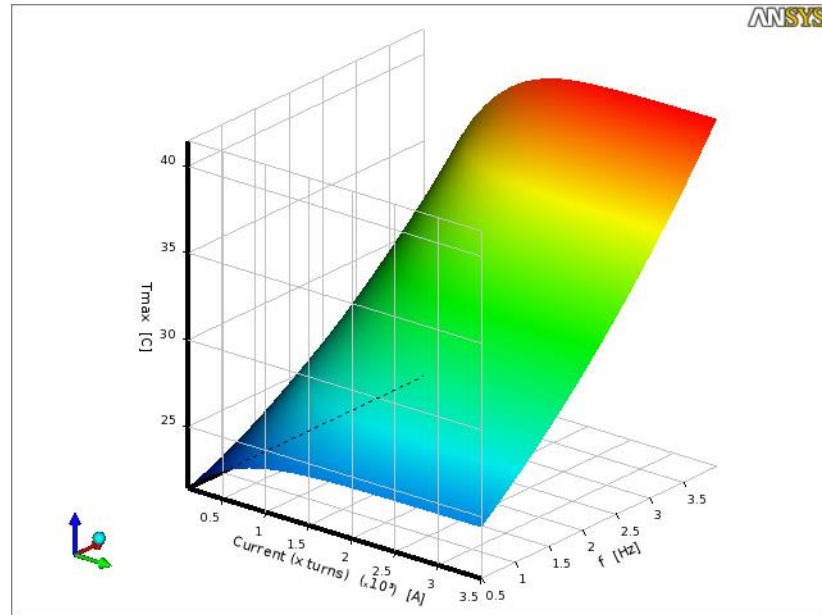
Analyses are also repeated for different strokes, frequencies, and currents. To do this, stroke, frequency, and current input are varied from 0.00635 to 0.0254 m, 0.5 to 4 Hz, and 100 to 3500 current x turns, respectively. Figure 2.26*a*, *b*, and *c* show the variations of the maximum temperature with these three parameters as a result of the Transient Thermal analysis at $t=5$ s, after 5 s of ongoing cyclic loading. The maximum temperature is observed to increase linearly with increasing stroke and frequency. The temperature is also found to increase with increasing current and level off as the current reaches around 2000 current x turns. This is due to the fact that the magnetic field and thus, the MR damping force saturates, causing the energy dissipation to reach its limit.



(a)



(b)



(c)

Figure 2.26. Variations of the maximum temperature in the MR fluid with respect to stroke, frequency, and current input.

As mentioned previously, another thermal analysis is conducted to calculate the time required to cool the device down to room temperature. To do this, the maximum temperature found in the Transient Thermal analysis is assigned to the MR fluid as an initial temperature, and all the outer surfaces of the device are subjected to convective boundary condition with $T_{\infty} = 22\text{ }^{\circ}\text{C}$ and $h = 50\text{ W/m}^2\text{ }^{\circ}\text{C}$ because the device is cooled with a fan at room temperature. Figure 2.27 shows the temperature contours after 1 hour. The maximum temperature is found to be concentrated in Chamber 1 which has a higher volume of MR fluid than Chamber 2. The heat tends to flow in the cylinder wall of the bottom chamber rather than the silicone oil, because the steel AISI 1018 has a higher thermal conductivity than that of silicone oil. The variation of the maximum temperature

with time is also plotted in Figure 2.28. The maximum temperature is found to decrease exponentially and it takes almost 1 hour for the device to cool down to room temperature.

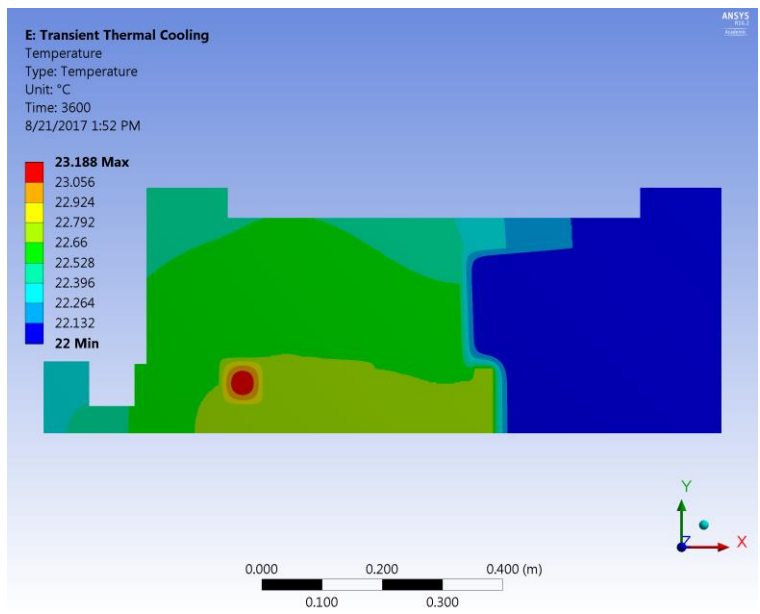


Figure 2.27. Temperature distribution after the Transient Thermal cooling analysis.

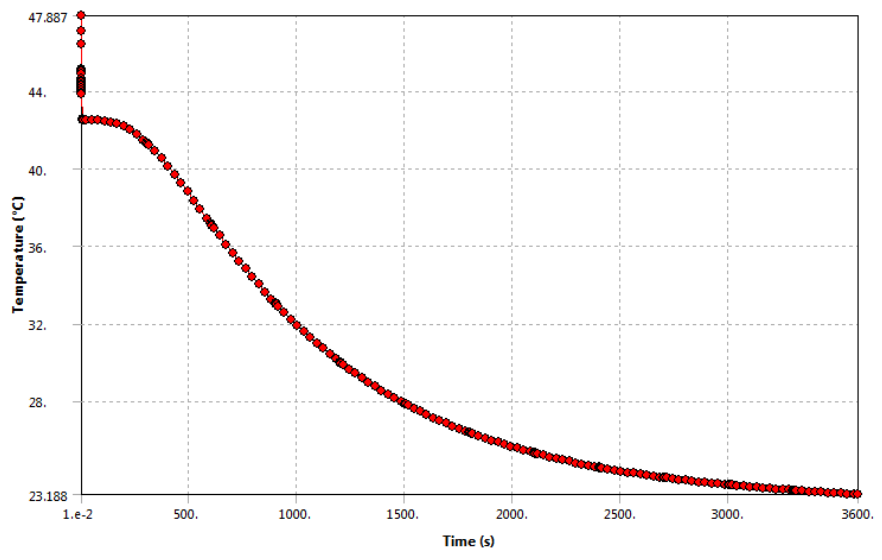


Figure 2.28. Variation of the maximum temperature in the MR fluid when the device is subjected to forced cooling with a fan at room temperature.

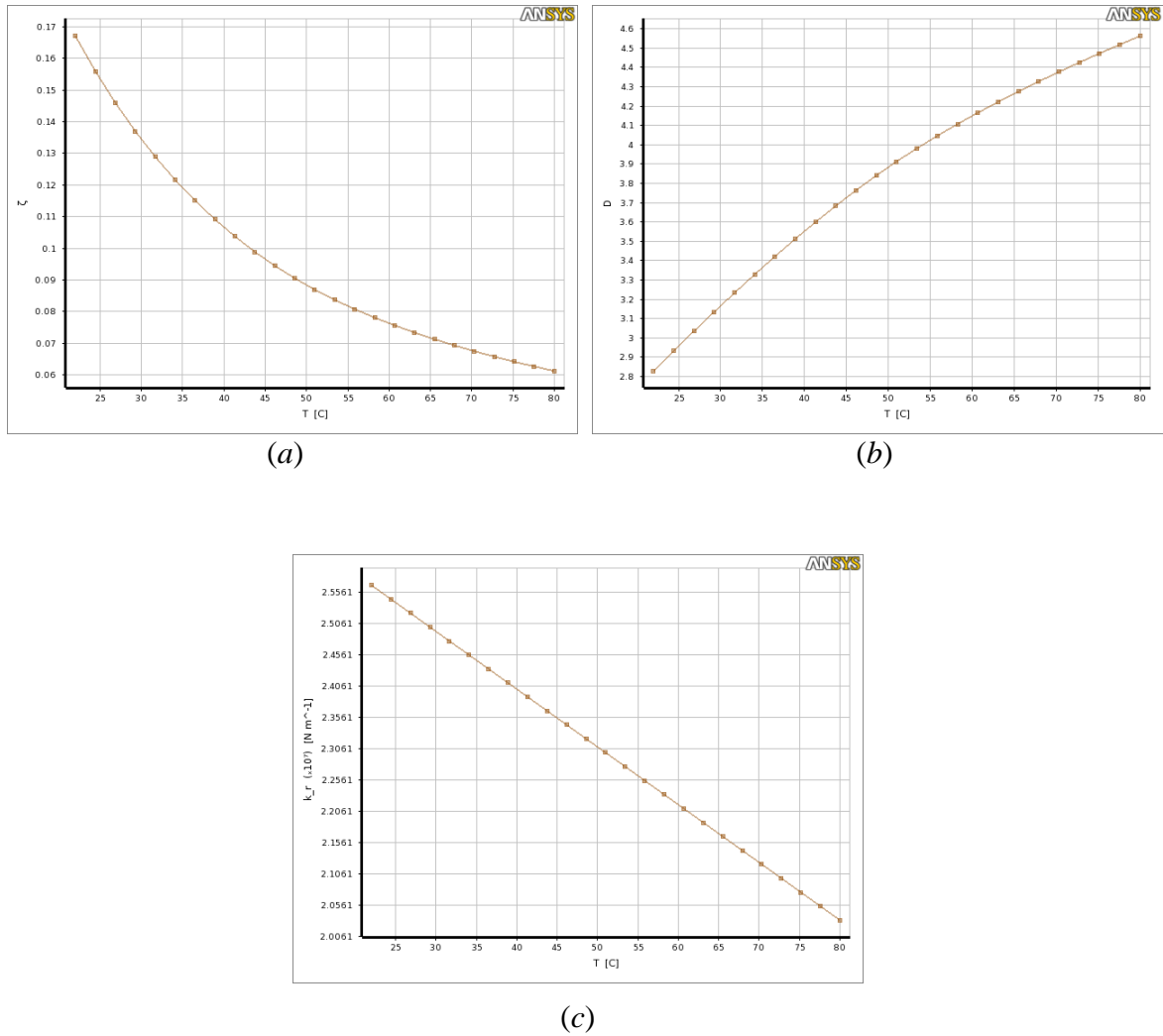


Figure 2.29. Effects of temperature on the viscous damping ratio, ζ_{viscous} , dynamic force range, D , and rebound and stiffness, k_r .

The temperature also affects the physical properties of the MR fluid. The viscosity of the MR fluid is known to decrease exponentially with increasing temperature according to the following formula [85],

$$\mu(T) = \mu_{40(^{\circ}\text{C})}(\text{Pa})e^{\left[\frac{(1+2.43\phi)(40(^{\circ}\text{C})-T(^{\circ}\text{C}))}{(T(^{\circ}\text{C})+48(^{\circ}\text{C}))}\right]} \quad (2.19)$$

where $\mu_{40(^{\circ}\text{C})} = 0.112 \text{ Pa}\cdot\text{s}$ and $\phi = 0.32$ for the MRF-132DG. The bulk modulus of the MR fluid, β , also decreases linearly with increasing values of temperature as shown by [80] with the following relation,

$$\beta(T) = 0.735 \times 10^9 (\text{Pa}) - 0.267 \times 10^7 \left(\frac{\text{Pa}}{^{\circ}\text{C}}\right) (T(^{\circ}\text{C}) - 22(^{\circ}\text{C})) \quad (2.20)$$

To see the effects of temperature on the design requirements of the viscous damping ratio, ζ_{viscous} , dynamic force range, D , and rebound stiffness, k_r , Eqs. (2.19) and (2.20) are implemented into the Excel module in the ANSYS program. Figure 2.29 shows the effects of temperature on these three design requirements. ζ_{viscous} is found to decrease exponentially as the temperature increases. This is due to the fact that the viscosity of the MR fluid decreases exponentially with temperature according to Eq. (2.19). The decrease in ζ_{viscous} is calculated to be 45% at the temperature of 42.5 °C. D is observed to increase with increasing values of temperature. However, the rate of increase reduces at higher temperatures. This is because F_{viscous} is decreasing exponentially with increasing values of temperature according to Eq. (2.19). Lastly, the rebound stiffness, k_r , is seen to decrease linearly with increasing temperature. This is because the bulk modulus of the MR fluid, β , decreases with increasing temperature according to Eq. (2.20). As the temperature is raised from 22 °C to 42.5 °C, the decreases in ζ_{viscous} and k_r are calculated to be 45% and 8%, respectively, whereas the increase in D is found to be over 25%.

In the light of these findings and due to the concerns about the performance of the seals and the electromagnet at elevated temperatures, the temperature in the MR fluid is kept at its minimum. The test durations are adjusted to ensure that the maximum temperature does not exceed 25 °C. The maximum temperature of 42.5 °C in Figure 2.25 is produced after 5 s under the maximum loading conditions, i.e., under the stroke, frequency, and current input of 0.0254 m, 4 Hz, and 3500 A x turns, respectively. To monitor the temperature in real-time during the testing, a thermocouple (TG24T(T)A2G, 36/5, 1/4NPT from Conax Technologies, INC) is used.

2.4. Optimization

The parametric studies in Section 2.3 reveal that the design requirements given in Table 2.1 are functions of some common geometric parameters. These parameters are depicted in Figure 2.3. In the structural analysis (Section 2.3.1), the minimum FOS and maximum shear deformation are found to be strong functions of R_{st} . Eq. (2.2) indicates that the rebound stiffness, k_r , varies with the fourth power of R_{st} . Hence, k_r is also a strong function of R_{st} . Also, the electromagnetic analysis (Section 2.3.2) shows that D and $\zeta_{viscous}$, are both functions of h , L_a , L_p and R_p . In order to achieve the given design requirements in Table 2.1, these parameters, R_{st} , h , L_a , L_p and R_p , must be optimized.

Furthermore, the thermal analysis (Section 2.3.3) shows that D , $\zeta_{viscous}$, and k_r vary with temperature. To optimize R_{st} , h , L_a , L_p and R_p and to account for the temperature effects in D , $\zeta_{viscous}$, and k_r , a multi-objective optimization program is developed in ANSYS platform. The program consists of two stages. In the first stage, the Static Structural and Microsoft Excel modules are run simultaneously to determine the

minimum FOS and maximum allowable shear deformation and to calculate k_r and k_c , respectively. In the second stage, the Maxwell, Microsoft Excel, and Transient Thermal modules are run simultaneously to determine the magnetic flux density in the flow gap, to calculate D and ζ_{viscous} , and to account for the heating effects, respectively. The input parameters such as R_{st} , h , L_a , L_p , R_p , X , and f , etc. are transferred from the Microsoft Excel module to ANSYS (Figure 2.30).






















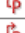
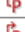

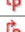




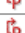
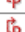


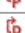


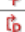


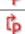

Outline of All Parameters				
	A	B	C	D
1	ID	Parameter Name	Value	Unit
2	[-] Input Parameters			
3	[-]  Geometry (A1)			
4	 P244	A	0.00057	
5	 P245	DS_h	0.0015	m
6	 P246	DS_C_th	0.23	m
7	 P247	DS_R_sb	0.082	m
8	 P248	DS_C_b_step	0.215	m
9	 P251	DS_R_p	0.125	m
10	 P253	DS_R_st	0.045	m
11	 P277	DS_L_a	0.01	m
12	 P278	DS_L_p	0.015	m
13	 P279	DS_L_2	0.1	m
14	 P280	DS_L_3	0.32	m
15	 P281	DS_L_1	0.075	m
16	[-]  Microsoft Office Excel (C1)			
17	 P157	WB_AWG	22	
18	 P158	WB_Bave	0.82263	T
19	 P160	WB_Cb_step	0.215	m
20	 P166	WB_CoilHeight	0.038	m
21	 P174	WB_h	0.0015	m
22	 P175	WB_HMRF	1.7705E+05	A m ⁻¹
23	 P185	WB_R_p	0.125	m
24	 P186	WB_R_sb	0.082	m
25	 P187	WB_R_st	0.045	m
26	 P188	WB_Stroke_X	0.0254	m
27	 P266	WB_frequency_f	4	Hz
28	 P271	WB_Temp	22	C
29	 P272	WB_L_1	0.075	m
30	 P273	WB_L_2	0.1	m
31	 P274	WB_L_3	0.32	m
32	 P275	WB_L_a	0.01	m
33	 P276	WB_L_p	0.015	m
34	 P289	WB_ConductorSource	1135	A
35	[-]  Maxwell 2D Design (B1)			
36	 P18	\$Phase_in [A]	1135	A
37	 P220	\$Temp [cel]	22	K
38	[-]  Transient Thermal Cooling (E1)			
39	 P234	Convection Film Coefficient	50	W m ⁻² C ⁻¹
40	 P262	Commands (APDL) ARG1	37.12	
41	[-]  Transient Thermal Heating (F1)			
42	 P239	MRF Magnitude	7.4447E+06	W m ⁻³
43	 P240	Coil Magnitude	2.0509E+05	W m ⁻³

Figure 2.30. Input parameters for the second optimization.

The geometric parameters and current input (conductor source) are shared with the Geometry and Maxwell modules, respectively. Eqs. (2.1), (2.2), (2.3), (2.9), (2.11), (2.15), (2.17), (2.18), (2.19), and (2.20) are implemented into the Microsoft Excel module. The outputs of the Maxwell module, i.e., magnetic flux density, B , and magnetic field intensity, H , are transferred to the Microsoft Excel module to calculate $\tau(B)$ and thus, F_{MR} and W_{total} . W_{total} is transferred to Transient Thermal module as a heat source to the fluid. Similarly, another output of the Maxwell module, total Ohmic loss, is transferred to the Transient Thermal module directly as the other heat source to the coils. These communications between the modules are performed simultaneously. Then, the optimum design is explored with the Response Surface Optimization module. Figure 2.30 and 2.31 show the optimized input and output parameters, respectively. The significant input and output parameters are also listed in Table 2.2.

Outline of All Parameters				
	A	B	C	D
1	ID	Parameter Name	Value	Unit
44	[-] Output Parameters			
45	[+] Microsoft Office Excel (C1)			
46	[p] P165	WB_CoilArea	0.00057	m ²
47	[p] P167	WB_CoilResistance	38.626	Ohm
48	[p] P170	WB_D	2.1861	
49	[p] P184	WB_PowerInput	122.52	W
50	[p] P190	WB_Turns	1103.8	
51	[p] P191	WB_Velocity_V0	0.63837	m s ⁻¹
52	[p] P192	WB_VoltageInput	39.718	V
53	[p] P209	WB_W_viscous	4076.8	J
54	[p] P210	WB_W_total	11741	J
55	[p] P211	WB_Ceq_total	2.3048E+05	N s m ⁻¹
56	[p] P212	WB_Ceq	80031	N s m ⁻¹
57	[p] P213	WB_ζ_total	0.48372	
58	[p] P214	WB_ζ_viscous	0.16796	
59	[p] P236	WB_C_th	0.2305	m
60	[p] P268	WB_mu	0.15795	Pa s
61	[p] P269	WB_β_MRF	7.431E+08	Pa
62	[p] P282	WB_Fμ_c	30797	N
63	[p] P283	WB_Fμ_r	71382	N
64	[p] P284	WB_Fr_c	59680	N
65	[p] P285	WB_Fr_r	91187	N
66	[p] P288	WB_CurrentInput	1.0283	A
67	[p] P291	WB_A_sb	0.021124	m ²
68	[p] P292	WB_A_st	0.0063617	m ²
69	[p] P294	WB_T	38664	Pa
70	[p] P295	WB_V_r	0.0063083	m ³
71	[p] P296	WB_V_c	0.083596	m ³
72	[p] P298	WB_A_p	0.049087	m ²
73	[-] Maxwell 2D Design (B1)			
74	[p] P216	B1	0.73682	
75	[p] P217	B2	0.93472	
76	[p] P218	B3	0.71578	
77	[p] P219	B4	0.9032	
78	[p] P254	Total_Ohmic_loss	2.0509E+05	
79	[p] P255	H1	1.3676E+05	
80	[p] P256	H2	2.3003E+05	
81	[p] P257	H3	1.293E+05	
82	[p] P258	H4	2.1211E+05	
83	[-] Transient Thermal Cooling (E1)			
84	[p] P233	Minimum Temperature in The MRF	22.066	C
85	[-] Transient Thermal Heating (F1)			
86	[p] P237	Maximum Temperature in The MRF	23.141	C
87	[p] P238	Temperature Maximum	23.141	C
88	[p] P263	Maximum Temperature in The Coils	22.192	C
*	[p] New output parameter		New expression	
90	Charts			

Figure 2.31. Output parameters for the second optimization.

Table 2.2. Optimized Input and Output Parameters at $T = 25\text{ }^{\circ}\text{C}$.

Input parameters		Output parameters		
h	0.0015 m	Eq. (2.1)	D	2.6
R_p	0.125 m	Eq. (2.2)	k_c	60,318 N/cm
			k_r	256,710 N/cm
L_a	0.010 m	Eq. (2.17)	ζ_{viscous}	0.17
L_p	0.015 m		Min. FOS (Shaft)	2.5
R_{st}	0.045 m		Max. shear deformation (Shaft)	0.21 mm
R_{sb}	0.082 m		F_f	5,500 N
L_1	0.075 m	Eq. (2.9)	$F_{\text{viscous},r}$ (for $X=0.0254$ m and $f=4$ Hz)	72,932 N
L_2	0.100 m		$F_{\text{viscous},c}$ (for $X=0.0254$ m and $f=4$ Hz)	31,466 N
L_3	0.320 m	Eq. (2.11)	$F_{MR,r}$ (for $\tau=40$ kPa)	123,960 N
$C_{b,\text{step}}$	0.215 m		$F_{MR,c}$ (for $\tau=40$ kPa)	81,130 N
w	0.790111 m			
Q_r	0.027275 m ³ /s			
Q_c	0.017851 m ³ /s			
β_{MRF} (assumed)	0.748 GPa			
β_{Silicone} (assumed)	1.13 GPa			
$A_{s,r}$	0.014762 m ²			
$A_{s,c}$	0.021124 m ²			
V_r	0.006308 m ³			
V_c	0.083596 m ³			
$A_{p,r}$	0.042726 m ²			
$A_{p,c}$	0.027963 m ²			
L_{piston} ($3L_p + 4L_a$)	0.085 m			
L ($4L_a$)	0.040 m			

CHAPTER 3 FABRICATION, EXPERIMENTAL SETUP, AND TEST PROGRAM

3.1. Introduction

The parts of the BLS-CMRD were fabricated by different vendors and assembled in the LSSL of UNR. The device was fixed to the floor in a horizontal configuration. An actuator was attached between the shaft head and the wall to excite the device axially. The shear loading was applied by pulling on the shaft head vertically via a high-strength strap attached to an I-beam frame. The device is excited sinusoidally at different strokes, frequencies, and currents. The axial and shear loadings, axial displacement and shear deformation of the shaft, pressures in Chamber 1 and 2, and the bottom chamber, temperature of the MR fluid, and applied current are measured.

3.2. Fabrication

The fabrication of the BLS-CMRD was a real challenge due to its large size. The parts of the device had to be machined at different locations. The top and bottom caps were outsourced to Sands Machine in Roseville, CA, whereas the cylinder and shaft were machined in Hood EIC, LLC and McBride Machine INC, respectively, both in Sparks, NV. The smaller parts, i.e., the top pedestal, top seal upper gland, top seal lower gland, bottom seal upper gland, bottom seal lower gland, and shaft stopper were machined at UNR's Mechanical Engineering Machine Shop. The fastener rods and nuts, seal gland bolts, pressure transducers, silicone oil, and hand-pump were purchased from McMaster-Carr. The seals were custom-designed and fabricated by American High Performance Seals. Table 3.1 shows a full list of the parts and fittings with their corresponding

suppliers or manufacturers. The fabrication drawings of the device are given in Appendix C.

Table 3.1. Components of the BLS-CMRD.

Part Name	Material	Quantity	Vendor
Top cap	A36	1	Sands Machine
Bottom cap	A36	1	Sands Machine
Cylinder	AISI 1018	1	Hood EIC, LLC
Shaft	AISI 1018	1	McBride Machine INC
Top pedestal	A36	1	UNR Machine Shop
Top seal upper gland	A36	1	UNR Machine Shop
Top seal lower gland	A36	1	UNR Machine Shop
Bottom seal upper gland	A36	1	UNR Machine Shop
Bottom seal lower gland	A36	1	UNR Machine Shop
Shaft stopper	A36	1	UNR Machine Shop
Fastener rods	Grade B7 medium-strength steel threaded rod, 2"-4-1/2 thread size, 6 feet long	4	McMaster-Carr
Fastener rod nuts	High-strength steel hex nut, grade 8, zinc yellow-chromate plated, 2"-4-1/2 thread size	12	McMaster-Carr
Fastener rod washers	Steel	4	UNR Machine Shop
Seal gland bolts	316 stainless steel socket head screw, M10 x 1.5 mm Thread, 30 mm Long	12	McMaster-Carr
Seal gland bolts	316 stainless steel socket head screw, M10 x 1.5 mm Thread, 80 mm Long	4	McMaster-Carr
Seals	Seal material Duralast 4555, AE ring material Duraloy 7333	3	American High Performance Seals
O-rings	Buna-N, 8 mm Wide, ID=332.252 mm,	1	McMaster-Carr

	ID=426.276 mm, ID=619.302 mm, ID=659.305 mm		
Pressure transducers	With NIST certificate, 0-10 V, 1/4 NPT, 10, 000 PSI 3196K9	3	McMaster-Carr
Thermocouple	TG24T(T)A2G, 36/5, 1/4NPT with 2 type T thermocouple wire, a cap, Grafoil Sealant,	1	Conax Technologies, INC
MR fluid	MRF-132DG	8 lt	Mid-Atlantic Rubber Co.
Silicone oil	LPS Silicone, 5 Gallon Pail	5	McMaster-Carr
Magnet wire	22 AWG Copper 4.4 kg	3	Superior Essex
Manual hand-pump	One speed, 45 cu. in. Oil capacity	1	McMasterr-Carr
Fixture plates	A36	1	Sands Machine

3.2.1. Fabrication of the Electromagnet

The electromagnet consisted of three coils wound in alternating directions. The coils were wound by using a lathe as shown in Figure 3.1 in LSSL of UNR. The lathe was equipped with a digital counting mechanism. A permanent magnet attached to the head of the lathe was detected by the counter at each revolution to count the number of turns of the coil. Before winding, the coil housing was insulated with Sprayon red insulating varnish to prevent a possible shortcut in the coil circuit. Then, the coil was wound with 1135 average turns per spool. After winding, the coil was covered with Loctite heavy duty epoxy. The epoxy was later shaved off with the lathe to be flush with the metal piston. The ends of the wire were insulated with a high-temperature heat-shrink tubing. A loose spring coil was formed with the heat-shrunk tubing to accommodate the

stroke of the shaft. The wire ends were then sent out from Chamber 2 with an insulation fitting from Conax Technologies.

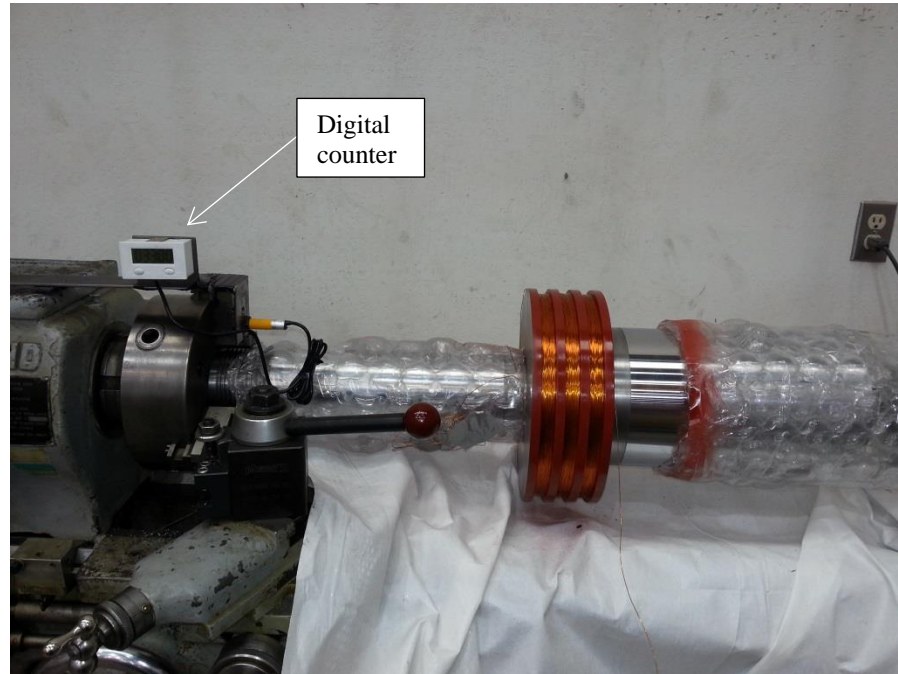


Figure 3.1. Setup for winding the electromagnet.

3.2.2. Assembly of the BLS-CMRD

The BLS-CMRD was assembled in the LSSL of UNR. The device parts were assembled in the order shown in Appendix A. During the assembly process, the external rods were tensioned with forces up to 800 kN with a hydraulic jack (Figure 3.2). The total length of the device in the neutral position and the width of the device are 1.187 m and 0.814 m, respectively.

Following assembly, the device was moved into its place within the test setup. To avoid any point loading, a grout was inserted between the device and laboratory floor (Figure 3.3).

After grouting, the chambers were filled with fluids. First, the bottom chamber was filled with pure silicone oil. The oil was fed to the chamber through a port at the bottom by utilizing gravity. To increase the filling rate and help prevent any entrapped air in the fluid, a vacuum pump was used to generate suction at another port at the top (Figure 3.4). This port was later used to measure the pressure in this chamber.



Figure 3.2. Tensioning of the BLS-CMRD with a hydraulic jack.

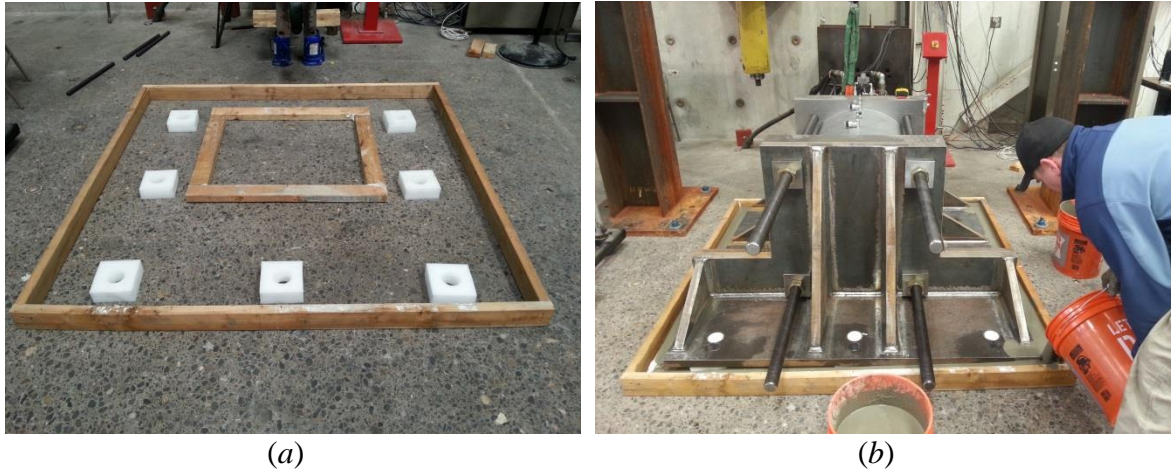


Figure 3.3. (a) Mold for grouting and (b) insertion of the grout.



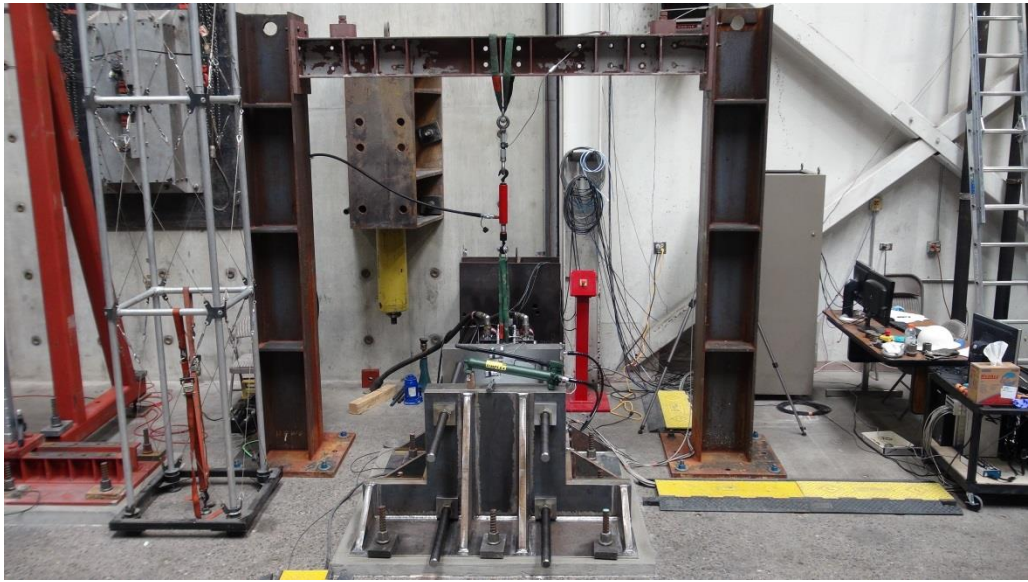
Figure 3.4. Filling the silicone oil into the bottom chamber.

Then, the top chamber was filled with MR fluid by using a hand pump (Figure 3.5b). The MR fluid was pumped slowly from a port at the bottom, allowing the air to flow out from a port at the top. When the chamber was close to full, the vacuum pump was attached to the top port to eliminate the air in the fluid.

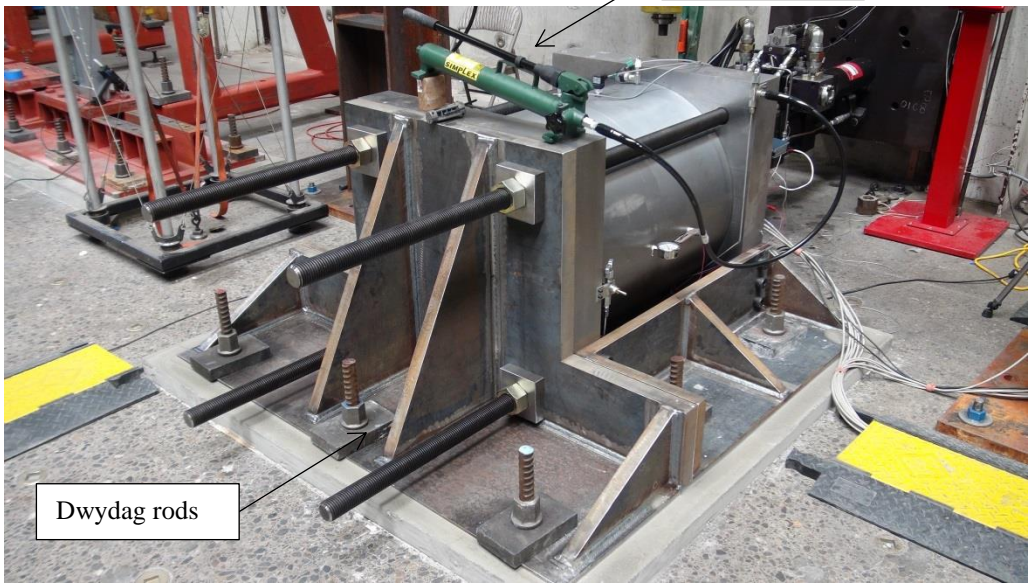
3.3. Experimental Setup

The BLS-CMRD was tested on the test setup shown in (Figure 3.5). The device was oriented horizontally whereas it would be vertical for real application. The device was fixed to the laboratory floor by using fixture plates via seven Dywidag tie rods, each capable of providing 355 kN in tension and 71 kN in shear (Figure 3.5*a,b*). In order to reflect the real-life loading conditions (Figure 1.6. Schematic for the installation of the BLS-CMRD under a building structure.), the device was excited axially via a 245 kN MTS-244.315 hydraulic actuator sinusoidally, and the shear loading was applied through a 5 ton hydraulic pulling ram attached to a vertical I-beam frame (shear frame) (Figure 3.5*c,d*). The axial displacement of the shaft was measured by a Novotechnik TR100-49 linear potentiometer (Figure 3.5*e*). The hydraulic ram was tied to the device from the top pedestal via a hoist ring and high-strength straps. A 89 kN load cell from Transducer Techniques was used to measure the shear loading (Figure 3.5*d*). The applied current to the electromagnet was fed back by a 10A DC magnetic current transducer from CR Magnetics Inc.

The pressures in the top and bottom chambers were controlled with Kerotest/Marsh N1572-10,000 psi needle valves and a one-speed 45 cu in hydraulic hand-pump. The pressures in Chamber 1 and 2, and the bottom chamber were measured via WIKA A-10 pressure transmitters (Figure 3.5*c*). The temperature in the top chamber was recorded via a TG24T(T)A2G-36/5 thermocouple from Conax technologies, INC. A TXDIN1620 universal DIN rail temperature transmitter from Omega® was used to acquire the temperature data (Figure 3.5*g*).



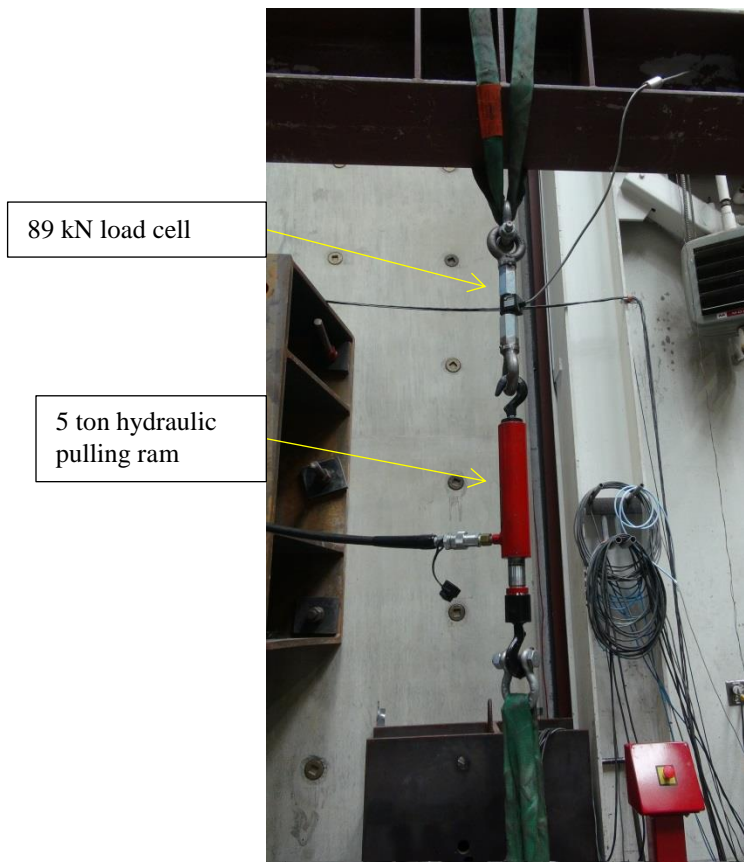
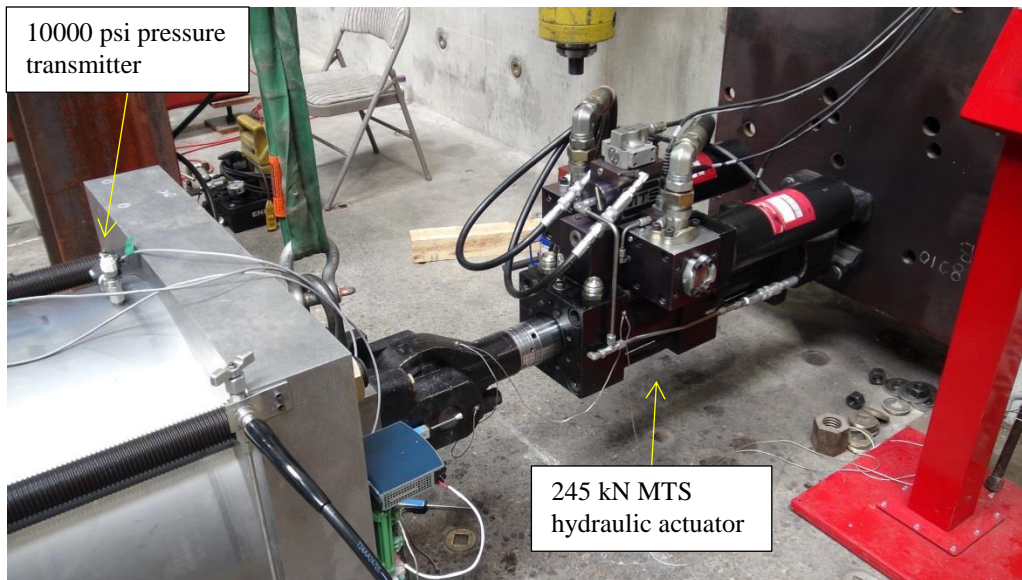
(a)

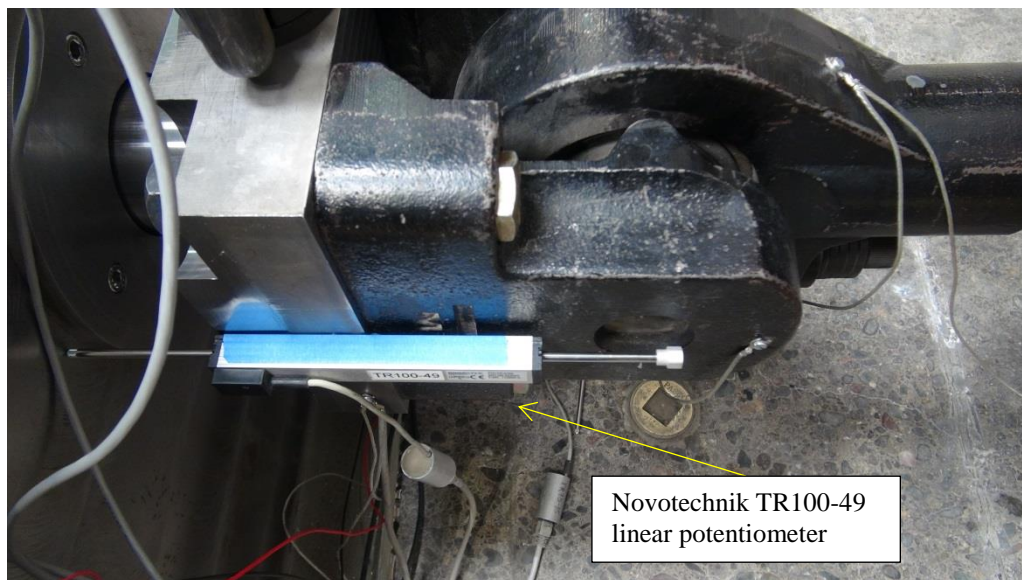


Hand pump

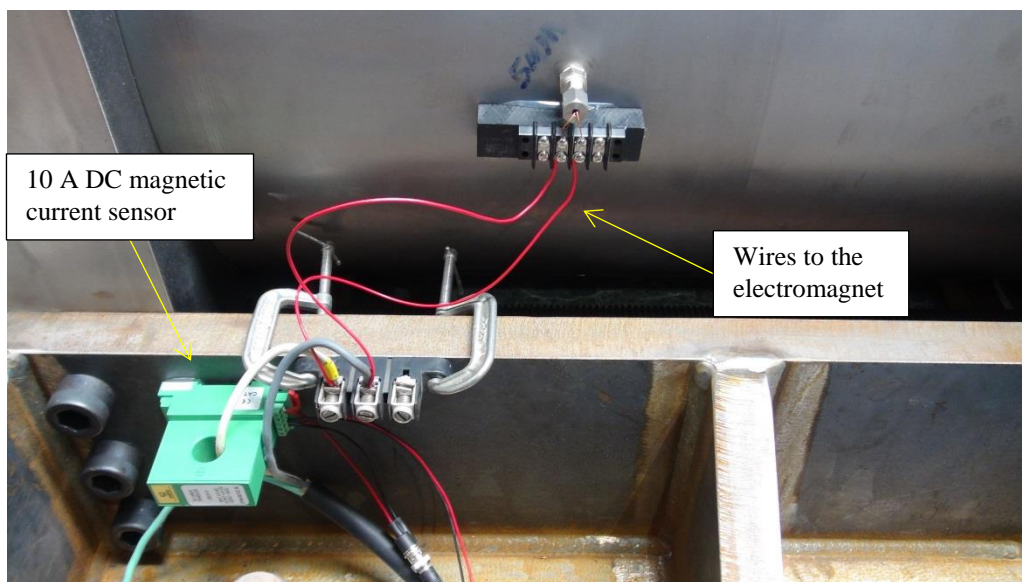
Dwydag rods

(b)

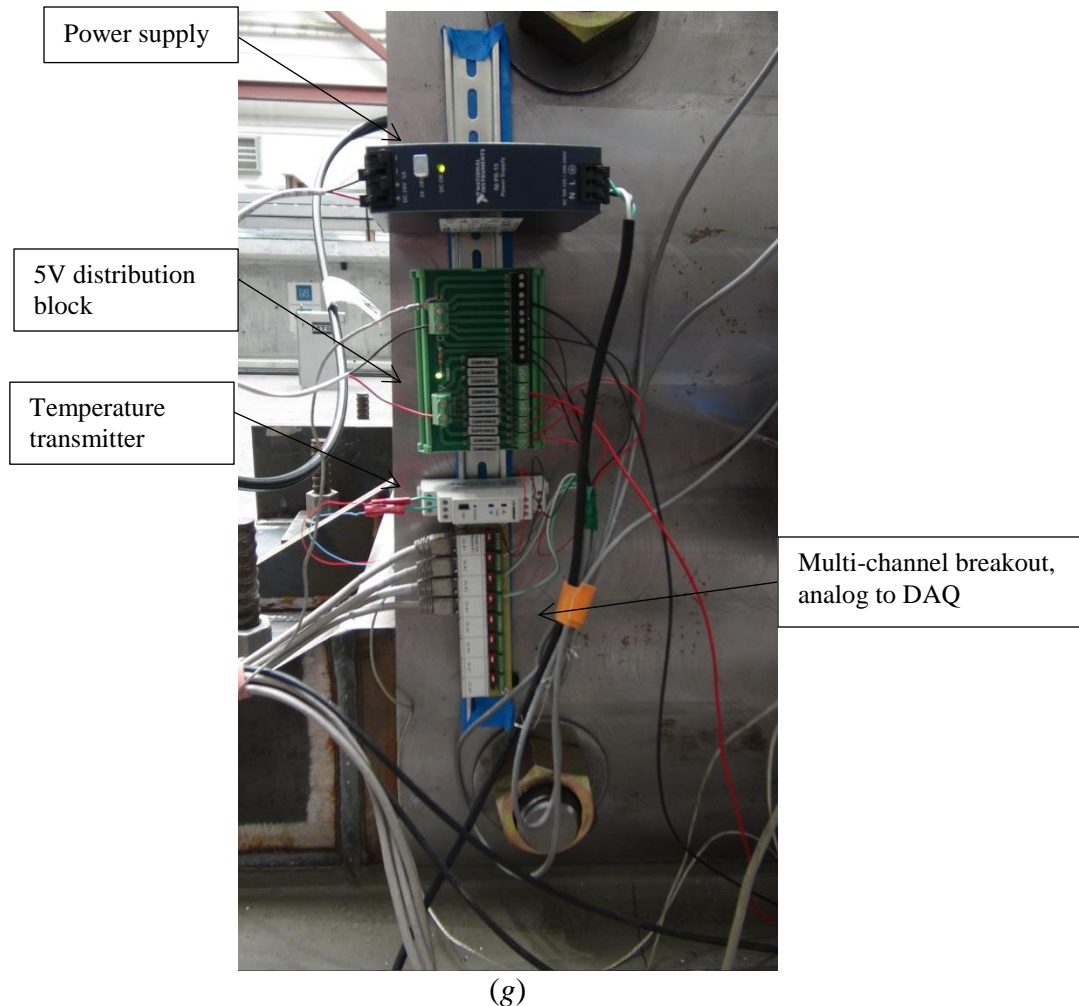




(e)



(f)



(g)

Figure 3.5. Experimental setup: (a) full-view (back), (b) BLS-CMRD, (c) hydraulic actuator, (d) hydraulic pulling ram, (e), shaft displacement transducer, (f) Current transducer, and (g) DAQ board.

3.4. Axial Testing

The following types of tests were performed for loading in the axial direction alone. First, the bulk modulus of MRF-132DG was measured with axial testing of a custom-made test plunger on an MTS machine. The tests were conducted under quasi-static conditions. The seal friction tests were also performed under quasi-static and dynamic conditions in axial mode. Finally, the dynamic behavior of the BLS-CMRD was characterized under axial loading with varying excitation amplitudes, frequencies, and currents of 0.0127 to 0.0254 m, 0.5 to 4 Hz, and 0 to 1 A, respectively. Tests were also conducted to see the response of the device to scaled earthquake motions. Each type of test is described in further detail in the following subsections. The tests except the earthquake motions were repeated three cycles for accuracy and to capture any system degradation.

3.4.1. Quasi-static Test

Quasi-static tests of the bulk modulus of MRF-132DG were performed with a passive oil plunger on an electromechanical MTS machine (Figure 3.7). Recall that the bulk modulus is needed to calculate the liquid stiffness in the top chamber. The tests were conducted at a rate of 0.0254 m/min to eliminate any inertial effects. Before filling up the damper, the MR fluid was placed in a vacuum chamber to remove any entrapped air inside the fluid (Figure 3.6).



Figure 3.6. MR fluid in the vacuum chamber.

Next, the fluid was poured into the plunger carefully to avoid any air bubbles. Air bubbles in the fluid are not desired because they would alter the compressibility of the fluid. Then, the plunger was installed on the MTS machine (Figure 3.7).

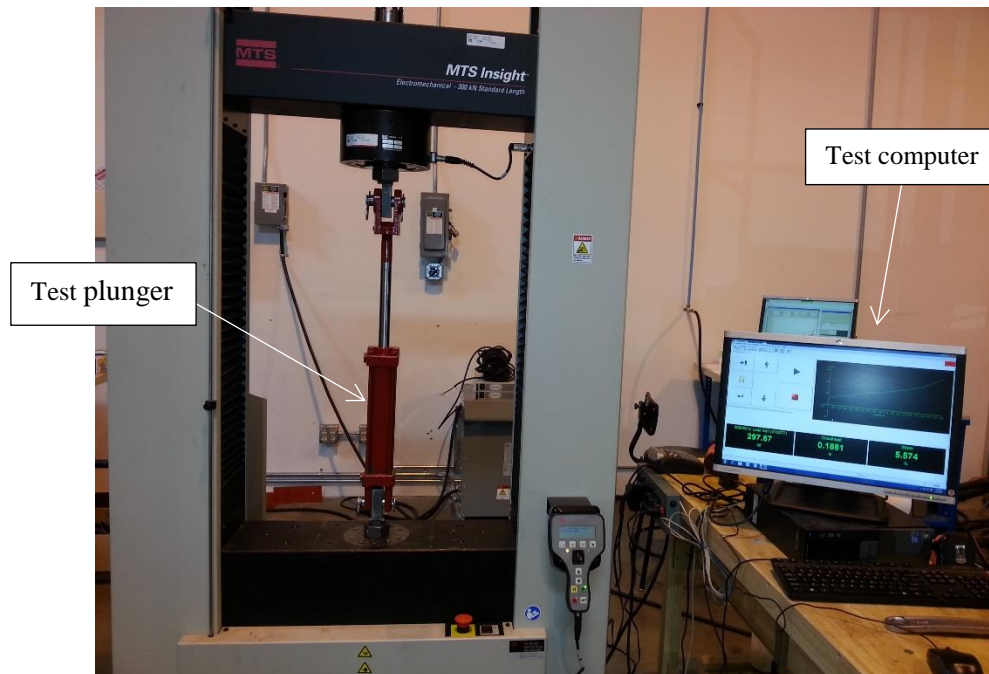


Figure 3.7. Test setup for the measurement of the bulk modulus of the MR fluid.

The fluid was compressed up to 17.24 MPa, the operating pressure limit of the plunger, to capture the variation of the bulk modulus with pressure in the broadest range. The compression tests were repeated at least three times to ensure accuracy. Figure 3.8 shows the variation of the bulk modulus with pressure. The bulk modulus is observed to increase with increasing values of pressure, but tends to level off at higher pressures. This is expected because the compressibility of the liquids reduces as the pressure increases, which means with the same amount of pressure increase the volume change is less at higher pressures compared to lower pressure ranges. This phenomenon was not fully captured due to the limitations on the test plunger.

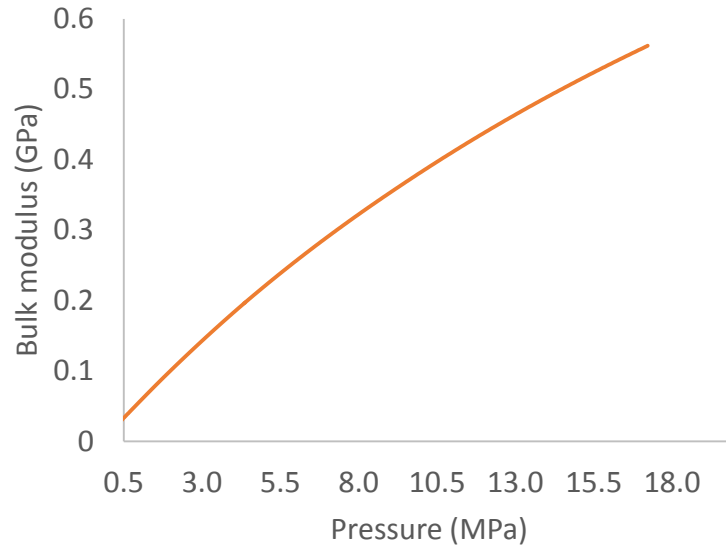


Figure 3.8. Variation of bulk modulus with pressure for MRF-132DG.

3.4.2. Seal Friction Characterization

The modeling of the seal friction force is discussed in Section **Error! Reference source not found.** The seal friction consists of two components: constant dry friction and dynamic friction. Due to the limitations on the test schedule at the LSSL, the seal friction tests were conducted after filling the top and bottom chambers with corresponding fluids. The tests were conducted at the stroke and frequency of 0.0127 m and 0.01 Hz, respectively.

3.4.3. Bi-linear Liquid Spring, Viscous Damping

The BLS-CMRD provides fail safe damping under no magnetic field. The fail-safe viscous damping forces are characterized at zero current and at different excitation

amplitudes and frequencies. Table 3.2 shows the test matrix for the characterization of fail-safe viscous damping.

Table 3.2. Test matrix for the characterization of passive damping force.

Amplitude, X (m)	0.0127		0.0254	
Frequency, f (Hz)	0.5	1.0	2.0	4.0
Current, I (A)	0			

Before starting the tests, a 92.8 kN static load was applied to the device by pressurizing the bottom chamber. The pressurization was controlled with the displacement of the shaft. Therefore, all tests started at around $(x, F) = (-0.01547 \text{ m}, -92.8 \text{ kN})$. This represents the expected field conditions. The static displacement makes the stroke longer in the compression side than the rebound side.

3.4.4. Bi-linear Liquid Spring, Viscous Damping, Controllable Magnetorheological Damping

Finally, the behavior of the BLS-CMRD was characterized at different magnetic fields. Table 3.3 shows the test matrix for the characterization of controllable magnetorheological damping.

Table 3.3. Test matrix for the characterization of controllable MR damping.

Amplitude, X (m)	0.0127		0.0254	
Frequency, f (Hz)	0.5	1	2	4
Current, I (A)	0.25	0.5	1	

3.4.5. Tests with Scaled Earthquake Motions

Tests were also conducted to see the response of BLS-CMRD to some scaled earthquake motions. Table 3.4 shows the selected earthquake motions with scale factors. The scale factor applied to the original recorded motion represents a design level earthquake. The motions were run at intensities ranging from 100% to 300% of the design level. The scaled displacements histories were input to the device at zero and different current levels.

Table 3.4. Earthquake records and scale factors.

No	Earthquake Name	Year	Station Name	Scale Factor
1	Northridge	1994	LA - Sepulveda VA Hospital	2.16
2	Loma Prieta	1989	LGPC	1.13
3	Chi-Chi, Taiwan	1999	TCU079	2.98

3.5. Combined Axial and Shear Testing

Lastly, the BLS-CMRD was tested for combined axial and shear loadings. The axial loading was applied at 0.0254 m stroke and varying frequencies and currents. The test matrix is shown in Table 3.5. The shear loads were applied by a hydraulic ram (Figure 3.5d). The ram was attached to the shear frame on one end and to the top pedestal on the other end via high-strength straps. It pulled on the top pedestal through a hoist-ring. The pedestal was connected to the actuator via a swivel joint, which prevented the applied shear load from passing to the actuator and thus, causing any possible damages to the actuator.

Table 3.5. Test matrix for combined axial and shear loading.

Force, F (kN)	3.34	6.67	13.35	27.85
Amplitude, X (m)	0.0254			
Frequency, f (Hz)	1		4	
Current, I (A)	0		1	

CHAPTER 4 EXPERIMENTAL RESULTS AND MODEL VERIFICATION

4.1. Introduction

In this chapter, results for the axial and combined axial and shear tests are presented. Only test matrices are shown in this section. The expanded test combinations are presented in Appendix B. The dynamic behavior of the device is modeled with the model equations given in Section 2.2.

4.2. Seal Friction Characterization

From Figure 4.1, the seal friction is found to be 5.5 kN in the compression side and as high as 12 kN at the maximum stroke in the rebound side. Also, the compression and rebound stiffnesses are calculated to be 76,685 N/cm and 484,175 N/cm.

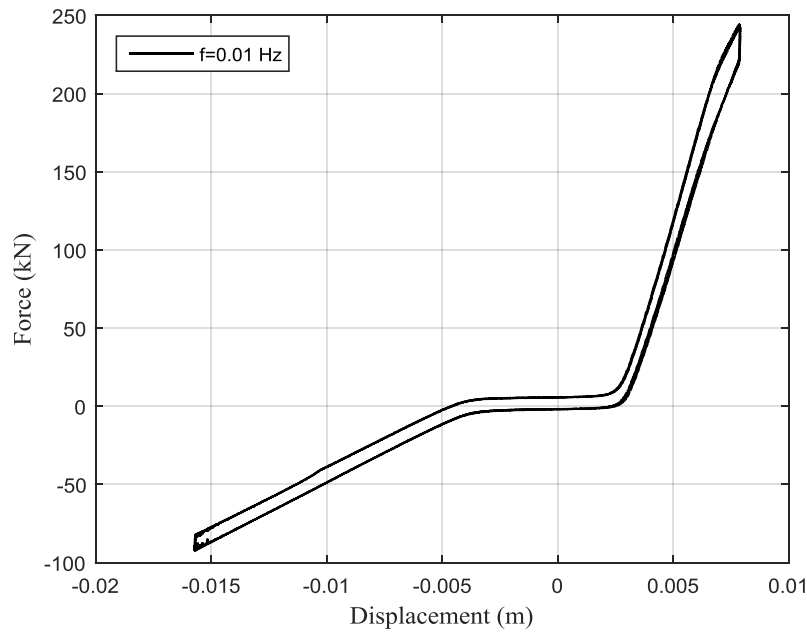


Figure 4.1. Seal characterization test at $X = 0.0127$ m and $f = 0.01$ Hz.

The design stiffnesses were 60,000 N/cm and 240,000 N/cm for the compression and rebound modes, respectively. The discrepancy between the design and realized stiffnesses for the rebound mode is believed to be a result of entrapped air in the MR fluid. As the shaft moves further into the top chamber, it first compresses tiny air bubbles and then squeezes the MR fluid. Therefore, the realized fluid volume is less than the design volume. The less volume means higher stiffness as the volume is the denominator in Eq. (2.2). Regarding the compression stiffness, the bulk modulus for the silicone oil was assumed to be 1.13 GPa from the literature. The discrepancy in the stiffness is assumed to come from a discrepancy in the bulk modulus; based on the observed stiffness, the actual bulk modulus is 1.40 GPa.

The flat region in the center of the force vs. displacement curve in Figure 4.1 is due to the air in both the bottom and top chambers. The shaft was initially displaced by $X_0 = 0.01547$ m to apply the static load. During this process, the shaft first compressed any entrapped air inside the bottom chamber and thus, the liquid stiffness occurred after a certain displacement. The same is true when the shaft moves into the top chamber. The shaft first compresses any entrapped air inside the top chamber, which results in no-stiffness region, and then compresses the liquid therein causing liquid stiffness.

4.3. Bi-linear Liquid Spring, Viscous Damping

Figure 4.2 and 4.3 show the force vs. displacement plots for frequencies of 0.5, 1, 2, and 4 Hz and strokes of 0.0127 m and 0.0254 m, respectively. From figures, it is observed that the force levels increase with increasing frequencies and strokes. This is

expected because viscous damping force (Eq. (2.9)) is a function of velocity which is functions of both stroke and frequency.

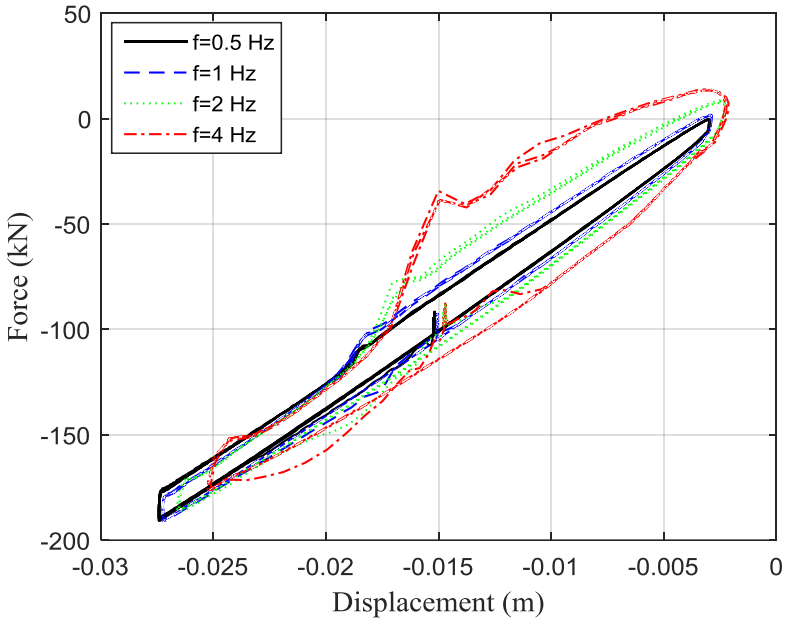


Figure 4.2. Force vs. displacement curves at zero current and $X = 0.0127$ m.

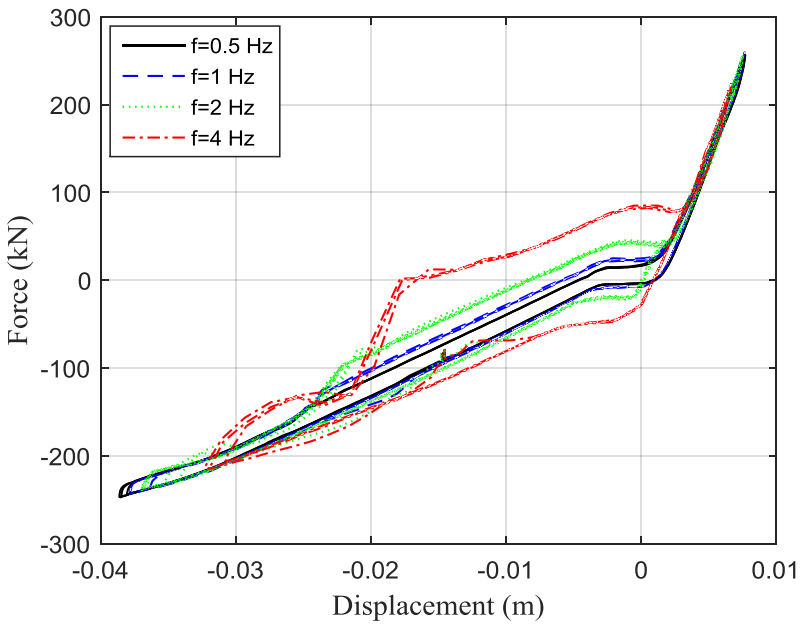


Figure 4.3. Force vs. displacement curves at zero current and $X = 0.0254$ m.

It is observed that the displacement levels are reduced as the frequency is increased. This is related to the test equipment. The actuator had a finite force vs. velocity curve, and with the higher velocities, the actuator was not able to provide the desired force levels.

Also, it is interesting to note that a portion of the energy dissipation is lost on the lower end of the plots, where the stroke reaches its maximum in the compression mode. This phenomenon will be discussed in the next section.

4.4. Bi-linear Liquid Spring, Viscous Damping, Controllable Magnetorheological Damping

Figure 4.4-4.6 show the test results for 0.0127 m stroke and different frequencies and current levels. It is observed that as the current input increases, the width of the curves increases. This is because the controllable MR damping increases with the applied current. It can also be seen that the rate of increase reduces as the current increases. This is due to the fact that MR fluid approaches to its magnetic saturation as the current continues to increase. The force levels also seem to increase with increasing frequencies as expected. The curves are not symmetric about the x -axis, i.e., the force increases more on the upper side of the curves. This is because there is more flow through the MR valve in the rebound mode than the compression mode. The effective piston area in the rebound mode is higher than it is in the compression mode. Also, each of the three comparative tests reaches a different displacement, although the target displacements are the same for the all. This is because the actuator reaches its force capacity. The deformation on the fixture plate between the actuator and the wall also contributed to the unequal

displacements. During the experiments, high forces are observed to cause visible deformations on the fixture plate.

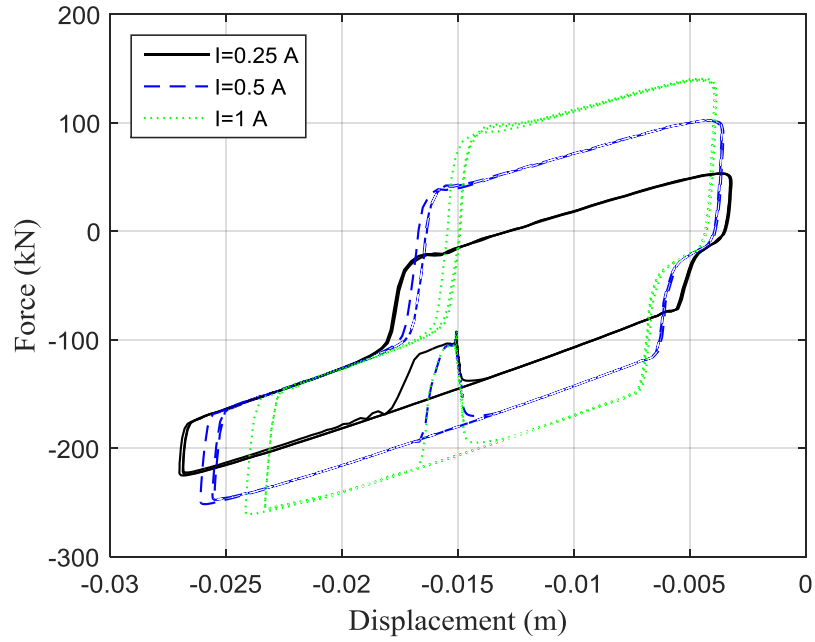


Figure 4.4. Force vs. displacement curves at $X = 0.0127$ m and $f = 1$ Hz.

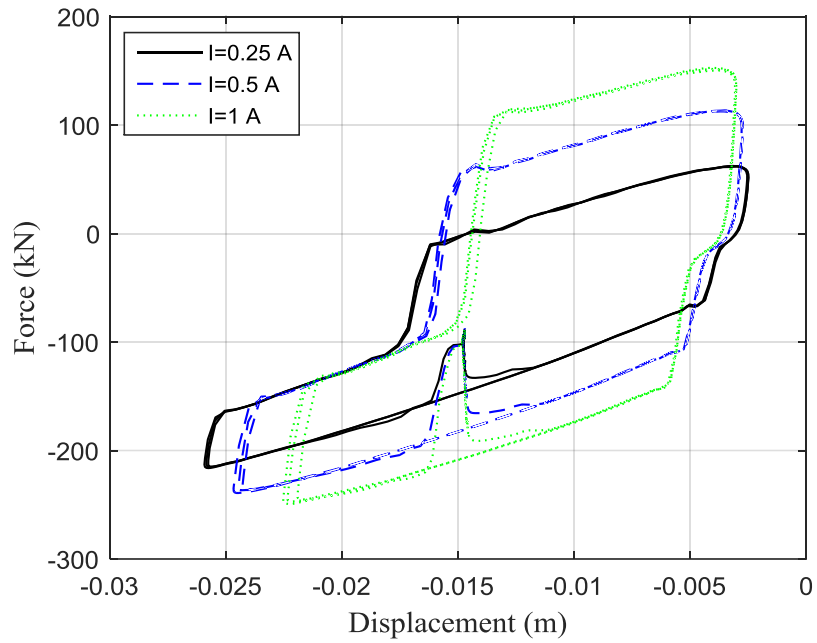


Figure 4.5. Force vs. displacement curves at $X = 0.0127$ m and $f = 2$ Hz.

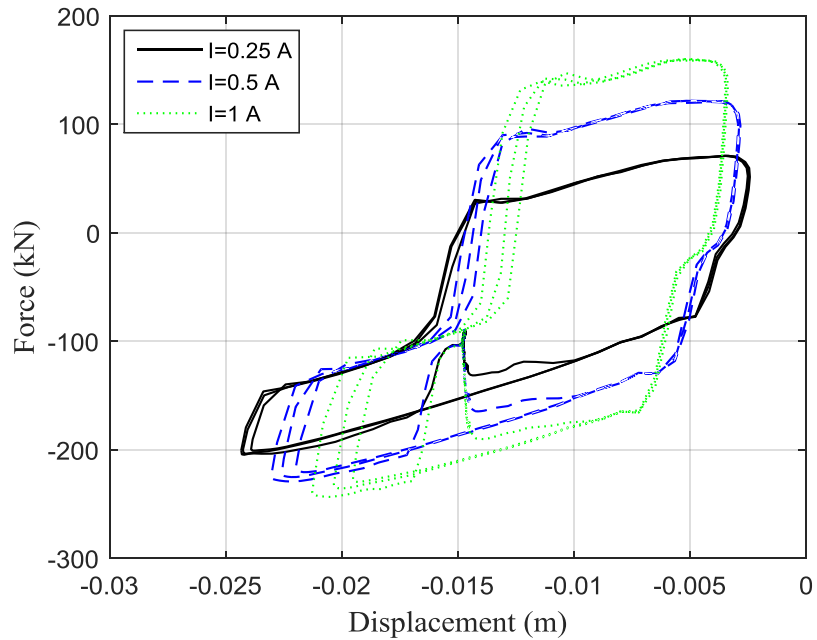


Figure 4.6. Force vs. displacement curves at $X = 0.0127$ m and $f = 4$ Hz.

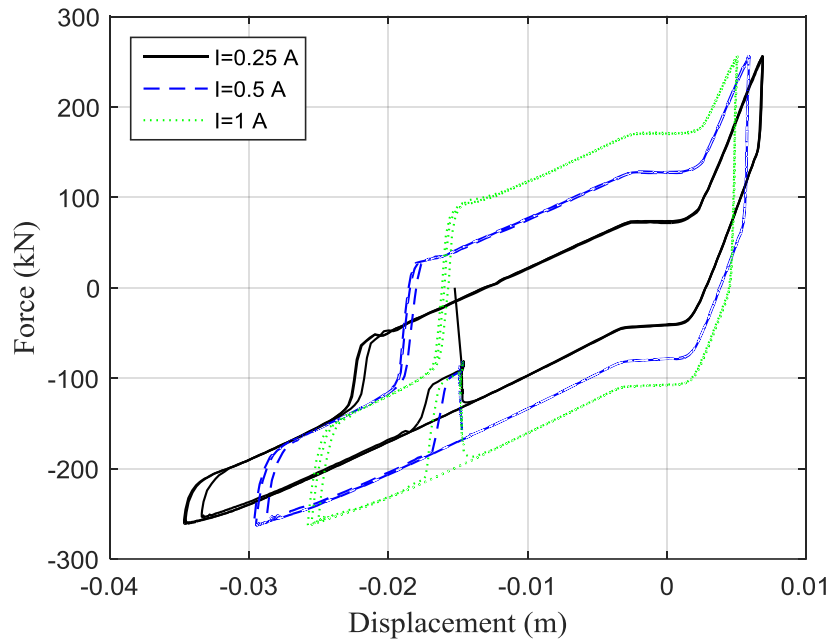


Figure 4.7. Force vs. displacement curves at $X = 0.0254$ m and $f = 0.5$ Hz.

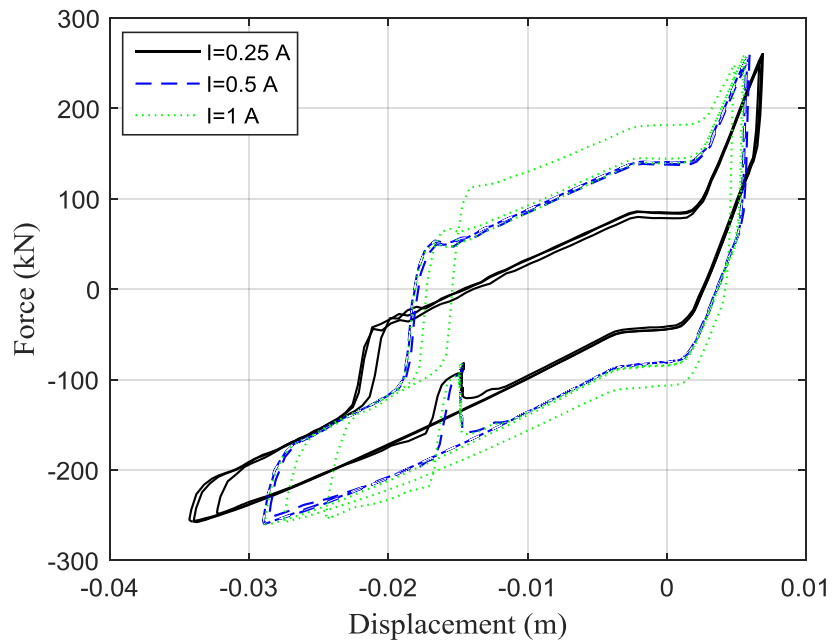


Figure 4.8. Force vs. displacement curves at $X = 0.0254$ m and $f = 1$ Hz.

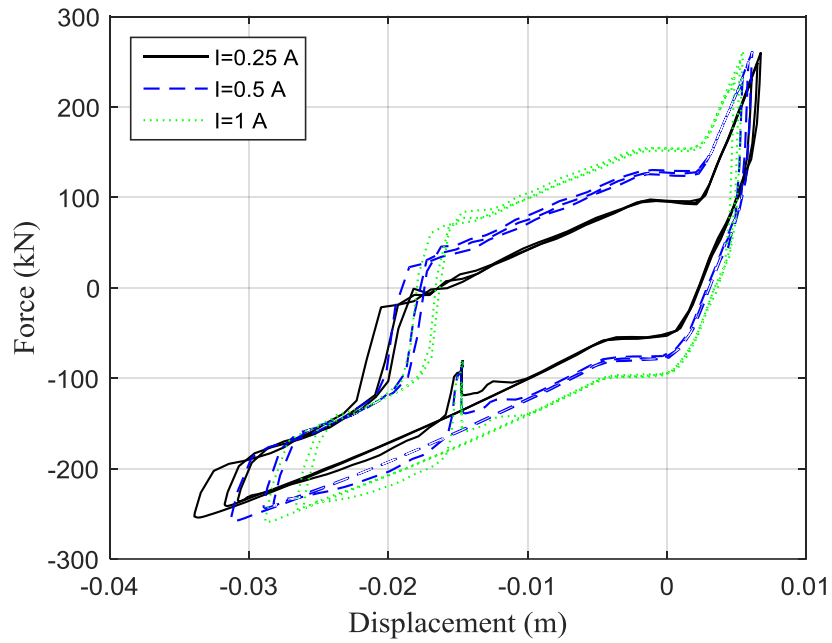


Figure 4.9. Force vs. displacement curves at $X = 0.0254$ m and $f = 2$ Hz.

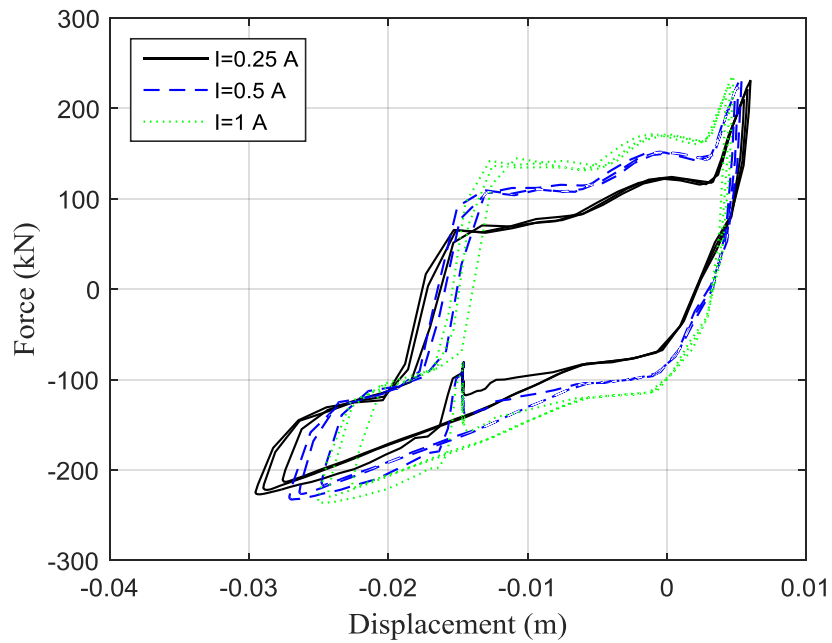


Figure 4.10. Force vs. displacement curves at $X = 0.0254$ m and $f = 4$ Hz.

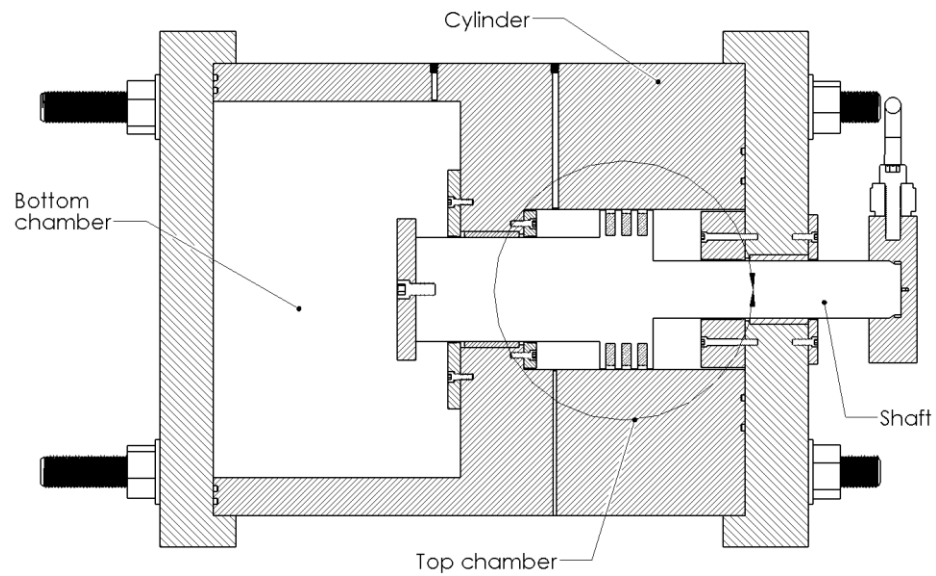
Figure 4.7-4.10 show the force vs. displacement curves for 0.0254 m stroke and different frequencies and current levels. Similar to the observations from Figure 4.4-4.6, the force levels increase as the current and frequency increase. A distinct bi-linear liquid stiffness is achieved as expected. However, it is also noted that there is a no-stiffness region between the compression and rebound modes. This is believed to be a result of trapped air in the top chamber. Following the tests, it was observed that a certain amount of air was trapped inside this chamber, which supports the reasoning.

As in Figure 4.2 and 4.3, cut-outs are observed in the force vs. displacements plots of Figure 4.4-4.10. These are the regions indicating the losts in the energy dissipation. The cut-outs become more visible as the force levels increase. This interesting phenomenon is attributed to the following: the entrapped air in the MR fluid, lack of accumulator in the top chamber, and difference in the shaft diameters. Before attempting any discussion, it is worth to describe how the force vs. displacement curves were obtained.

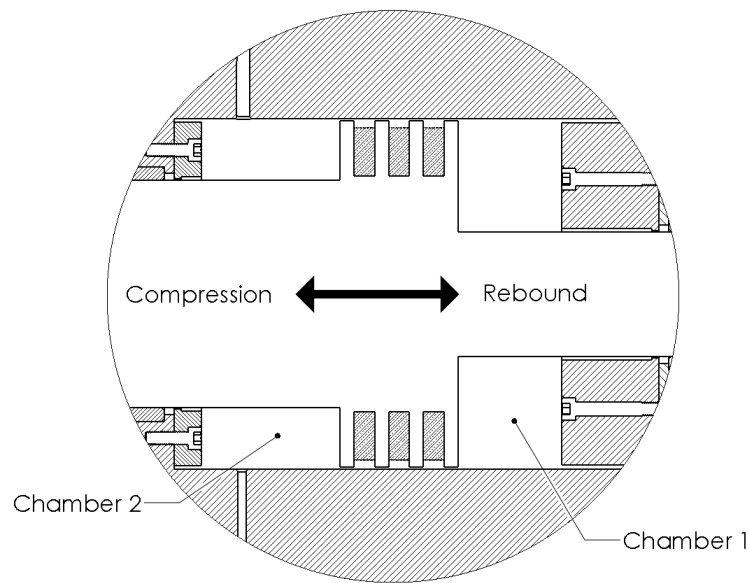
Prior to the tests, the bottom chamber was pressurized by displacing the shaft for $X_0 = 0.01547$ m into this chamber to account for the static load of the structure. Then, sinusoidal excitations were applied at two different strokes, $X = 0.0254$ m and $X = 0.0127$ m, frequencies and current levels. In all of Figures 4.2-4.10, the curves start at $X_0 = -0.01547$ m and continue to the left (compression mode) as the shaft moves further into the bottom chamber. After reaching the maximum stroke in the compression mode, then they reverse the direction to the right (rebound mode) and continue to reach first the initial displacement ($X_0 = -0.01547$ m) and then the maximum stroke in this mode. Then,

they again reverse the direction to the left (compression mode) to complete the cycles.

The compression and rebound modes are depicted in Figure 4.11.



(a)



(b)

Figure 4.11. (a) 2D cross-section of the device and (b) detail view of the top chamber.

The cut-outs happen when the shaft begins the rebound mode. When the shaft starts from $X_0 = -0.01547$ m and moves to the left, the fluid in Chamber 2 flows through the annular flow gap between the piston and inner wall of the cylinder into Chamber 1. However, the area of the piston on Chamber 2 side is less than that on Chamber 1 side. The amount of the fluid that flows into Chamber 1 is not able to compensate the void that occurs in this chamber due to the motion of the shaft. Because, when the shaft moves to the left, it takes out volume from the top chamber thereby reducing the pressure in this chamber. If there is air trapped in the MR fluid, then the air bubbles expand in Chamber 1. Now when the shaft reverses direction and moves to the right into the top chamber, it first compresses the air bubbles in Chamber 1 which results in no flow across the piston, and thus no damping. The flow starts again when no air bubbles remain in Chamber 1. The same phenomenon occurs again when the shaft shifts modes from rebound to compression. However, the amount of energy dissipation lost is much less for compression than for rebound. This cut-out could be minimized or eliminated by pressurizing the top chamber. The pressurization would help eliminate the air bubbles. It would also ensure that there is always a positive pressure so that a flow occurs across the piston.

Another solution to the cut-out regions would be a modification to the current design. The MR valve could be removed from the top chamber and placed into a third chamber to provide only damping in this chamber, as presented in Figure 4.12. In this configuration, the compression and rebound chambers would provide the bi-linear liquid spring effect, while the damping chamber would be used only for passive and controllable MR damping. The equal shaft diameters before and after the piston would

eliminate the drawbacks that occurred in the current design. The proposed design configuration would also greatly reduce the size of the device. The primary reason for the large size of the current design is that the diameter of the top shaft had to be large to account for the shear loading, and the remaining system requirements had to be achieved based on the large shaft diameter. With this proposed design, a higher stiffness could be achieved by reducing the sizes of the bottom shaft and the rebound chamber, and the targets for the viscous damping and dynamic range could be achieved independently in the damping chamber. A lower bottom shaft diameter would reduce the size of the lower chamber to achieve the required compression stiffness. The design process described here would greatly reduce both the length and width of the device.

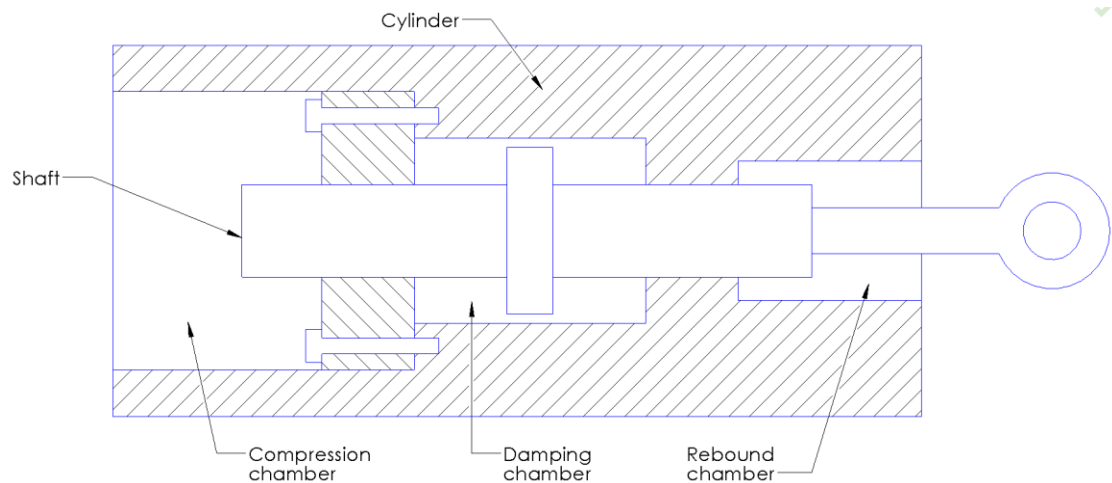
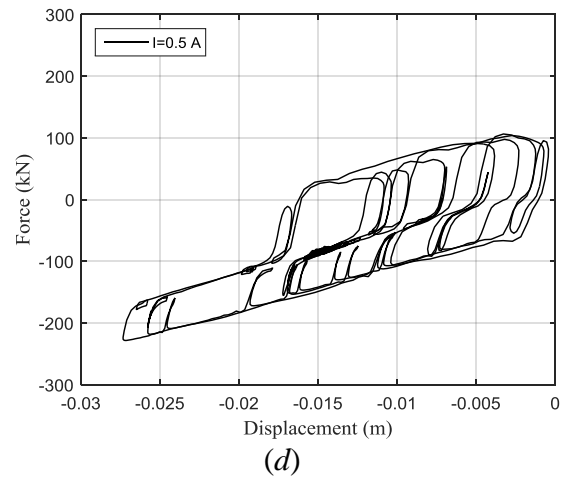
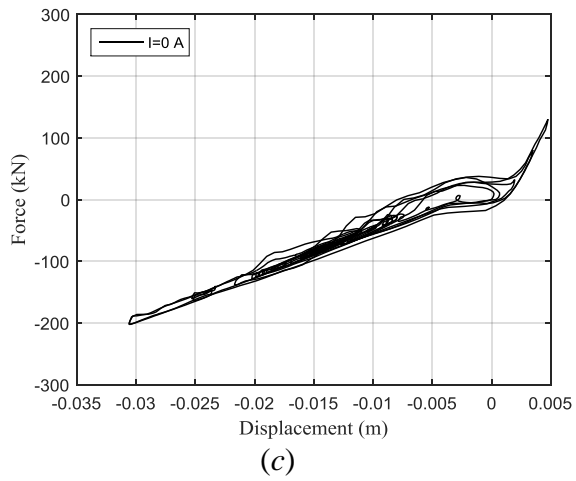
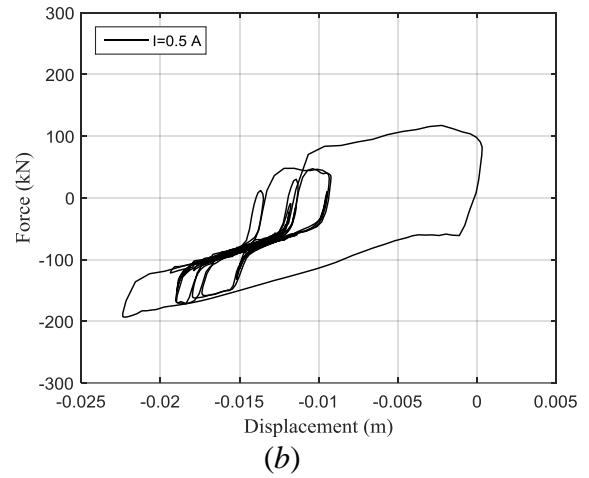
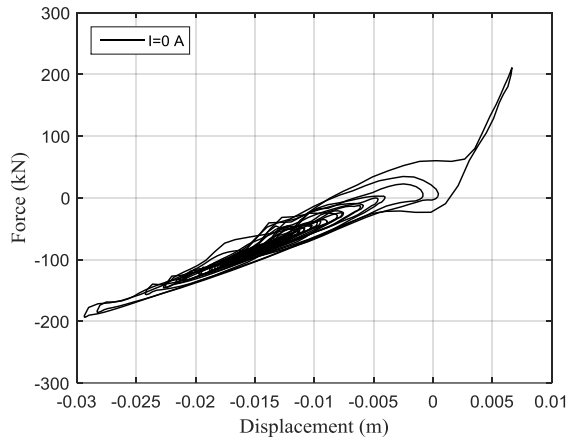


Figure 4.12. An alternative design for the BLS-CMRD.

4.5. Tests with Scaled Earthquake Motions

Figure 4.13 shows the response of the BLS-CMRD for zero and 0.5 A currents for 150% design level of the listed earthquakes. From the Figure, it is seen that the same energy dissipation is achieved with less displacement. However, for an effective isolation both

displacement and acceleration levels should be within desired limits. Study for control of the device is beyond the scope of this work.



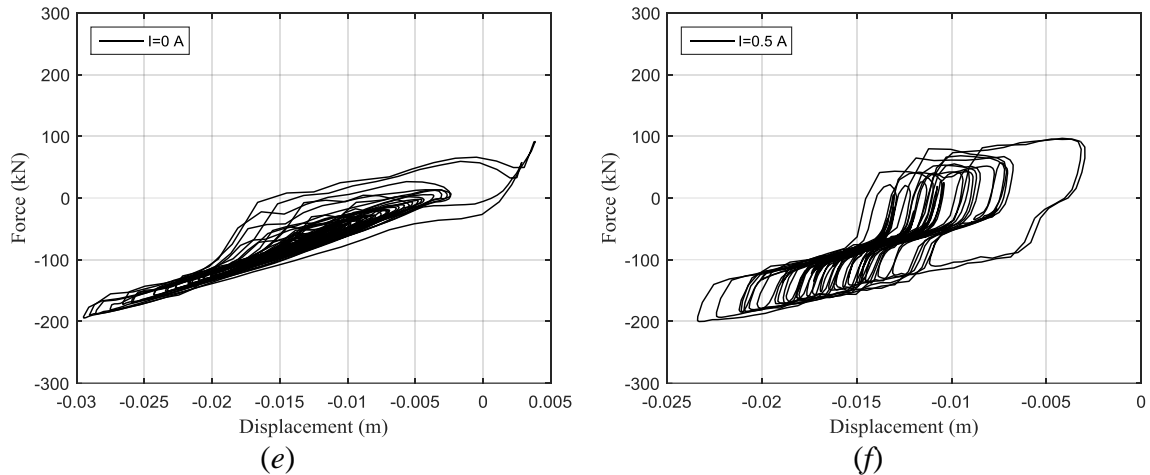
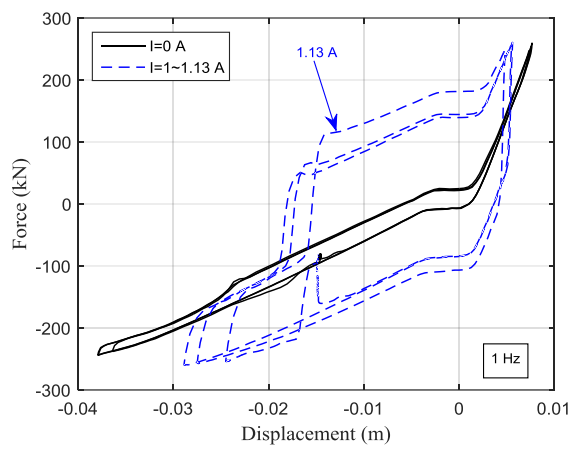


Figure 4.13. (a), (b) Northridge-01, LA-Sepulveda V A Hospital, (c), (d) Loma Prieta, LGPC, and (e), (f) Chi-Chi, TCU079, all at 150% design level.

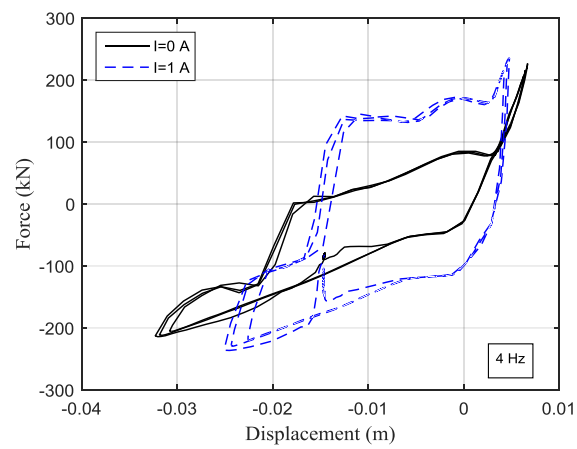
4.6. Combined Axial and Shear Testing

Figure 4.14*a-l* show the force vs. displacement curves for zero to 27.85 kN shear loadings. The tests were conducted at fail-safe passive damping and 1 A current at the design stroke of 0.0254 m. A visual inspection on Figure 4.14*a-l* would show that the BLS-CMRD maintains its performance under combined axial and shear loadings without a loss in its performance. This important achievement would suggest that the BLS-CMRD could be used in earthquake isolation of building structures successfully.

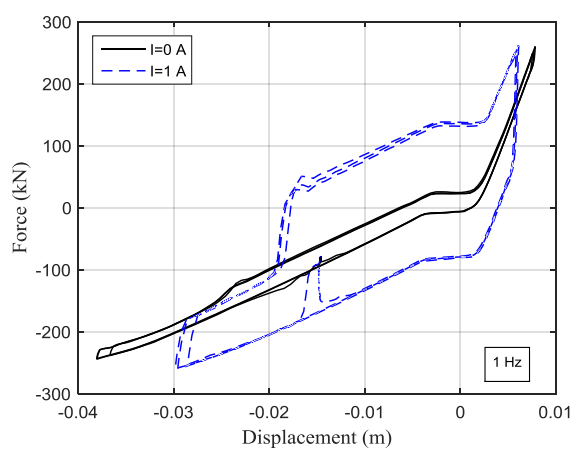
It should also be noted that the recorded fluid temperatures did not exceed 23 °C for all the tests performed.



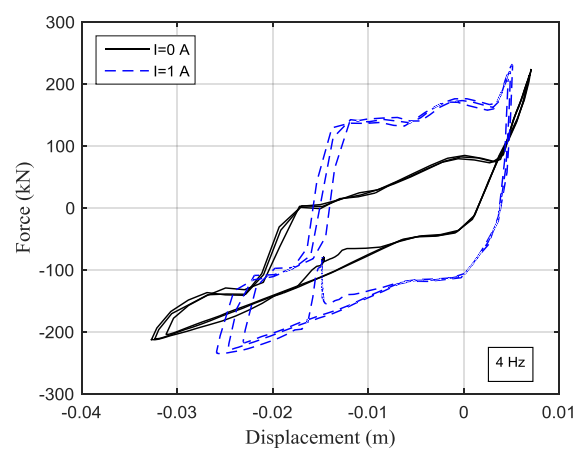
(a)



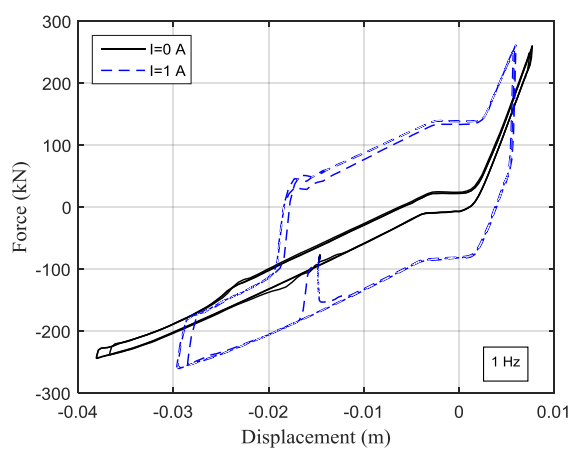
(b)



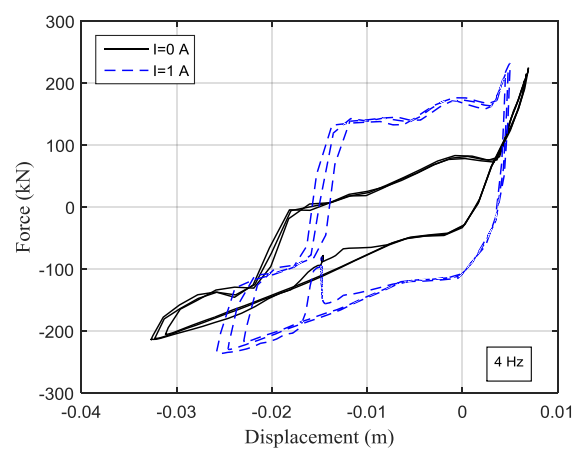
(c)



(d)



(e)



(f)

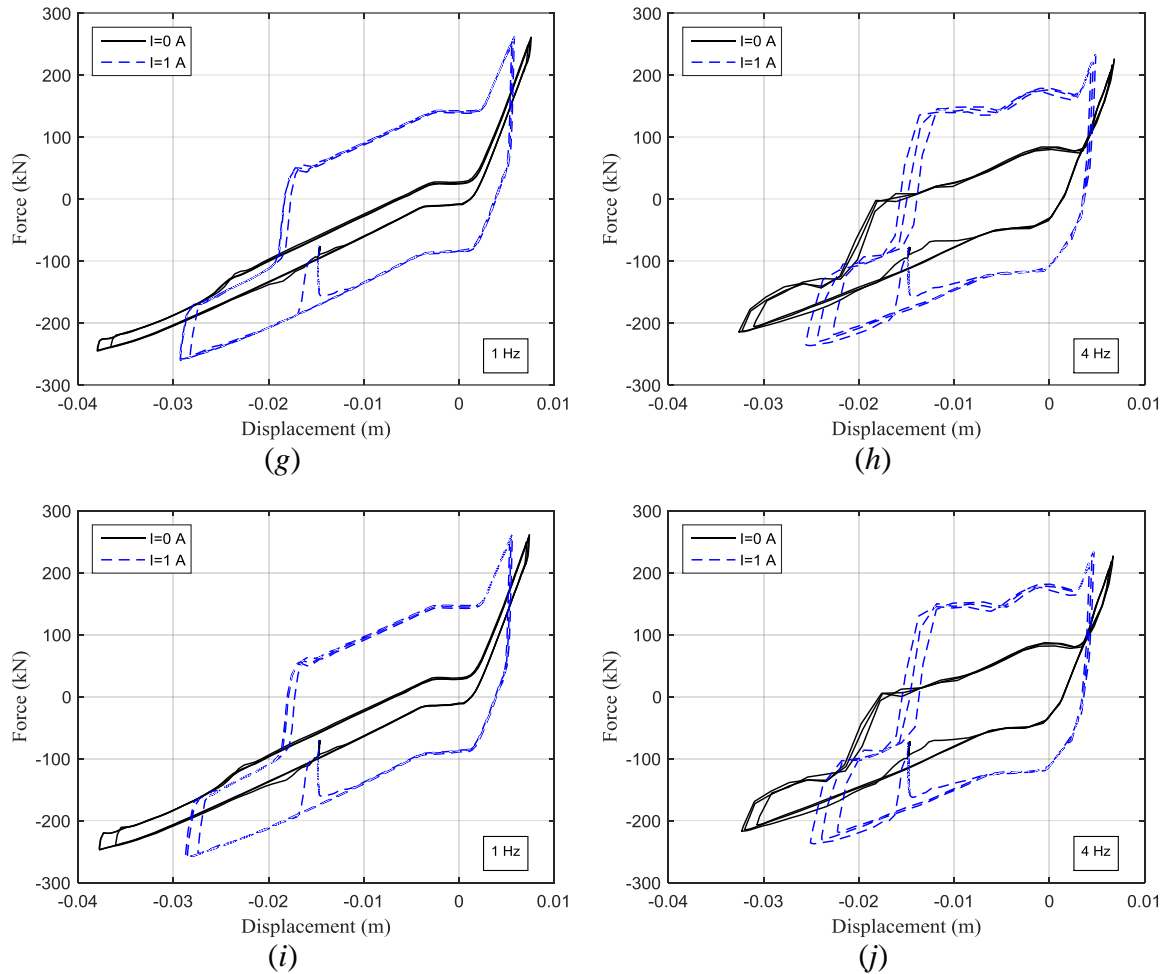


Figure 4.14. Force vs. displacement curves at different shear loadings: (a),(b) zero-shear load, (c),(d) 3.34 kN, (e),(f) 6.67 kN, (g),(h) 13.35 kN, and (i),(j) 27.85 kN.

4.7. Model Verifications

The modeling procedure for the BLS-CMRD is discussed in Chapter 2. In this section, several comparisons are made to validate the modeling approach. The comparisons are made for the stroke of 0.0127 m at different frequencies and current levels. The bulk modulus of the Silicone oil is calibrated to be 1.40 GPa from the slope of the curves, whereas it was assumed to be 1.13 GPa in the design stage from the literature. The yield stresses for the calculation of the controllable MR damping are also calibrated

from test data. The variations of the experimental and model yield stresses with the applied current are given Figure 4.15.

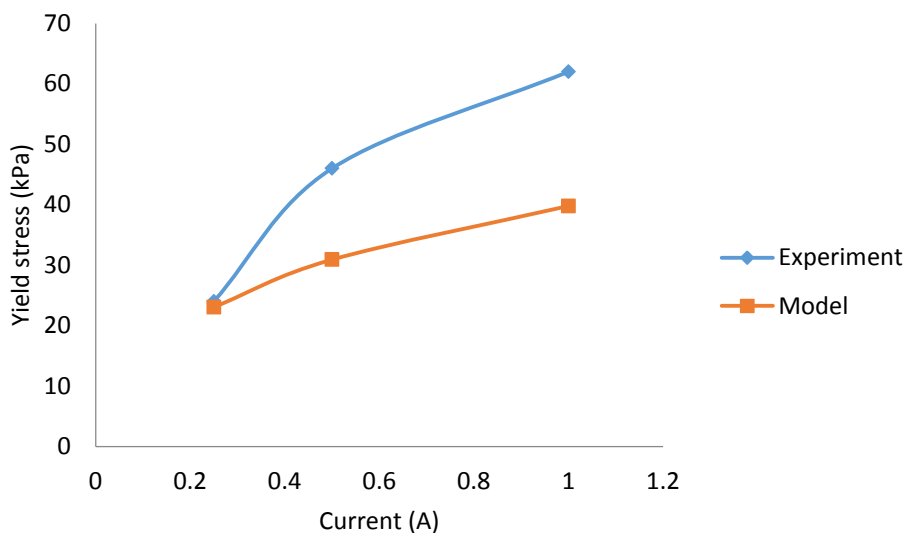


Figure 4.15. The experimental and model yield stress vs. current.

The difference between the experimental and model yield stresses could be attributed to the effect of pressure. Recent studies reveal the effect of pressure on the yield stress [86]–[88]. Spaggiari and Dragoni [86] report that yield stress is increased from 50 kPa to 150 kPa when the pressure is increased from 0 to 30 bar at 800 mT magnetic field. Also, as the magnetic field is increased, the effect of the pressure becomes more dominant, a similar trend observed in Figure 24. In another study, Spaggiari and Dragoni [87] demonstrate that the yield stress of MRF-130CG of Lord Co is increased by 200% as the pressure is increased to 30 bar at the highest magnetic field of 300 mT in shear mode. Becnel et al also show that the yield stress of MRF-132DG of

Lord Co is increased by 77% for a rotary magnetorheological energy absorber. Squeeze strengthening effects are realized when the magnetic field exceeds 50 kA/m.

Figure 4.16-4.19 show the comparisons for $X = 0.0127$ m, zero current, and different frequencies. There is a good agreement between the model and experimental data except that the model is not able to capture the cut-out existing in the experimental data.

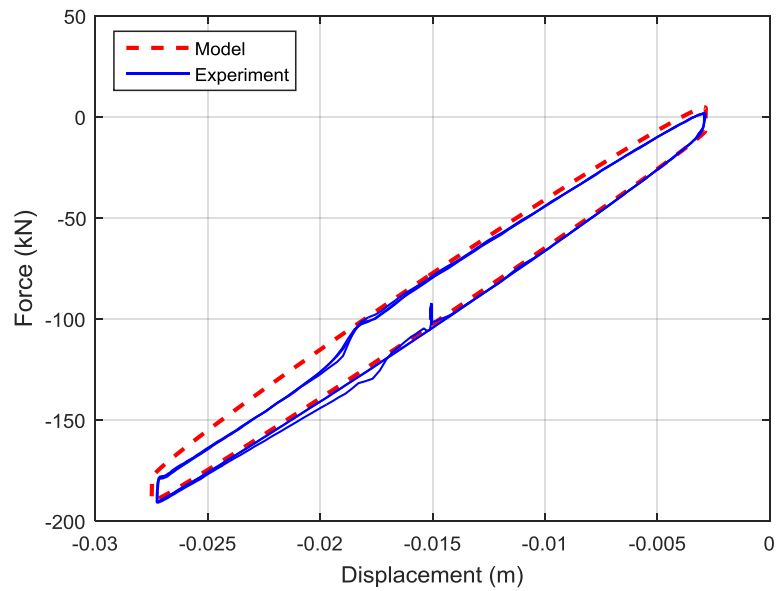


Figure 4.16. Comparisons between the model and experiments for $X = 0.0127$ m, $f = 0.5$ Hz, and zero current.

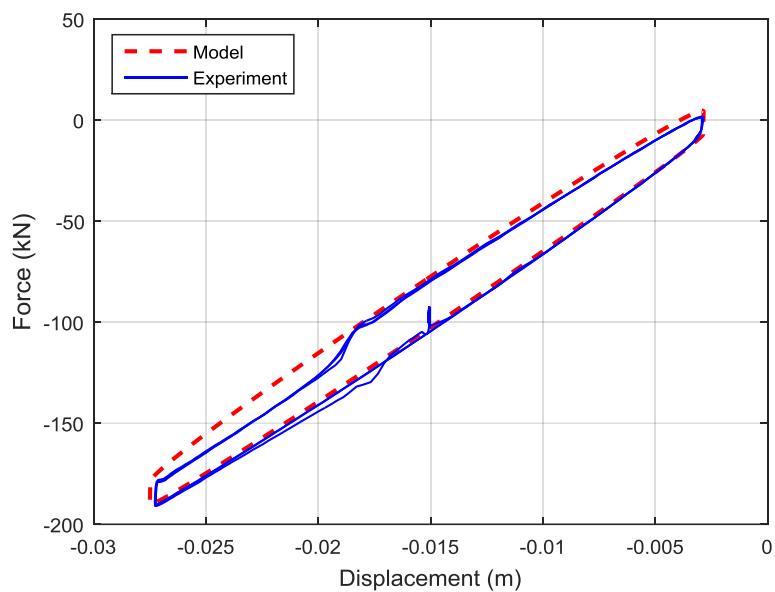


Figure 4.17. Comparisons between the model and experiments for $X = 0.0127$ m, $f = 1$ Hz, and zero current.

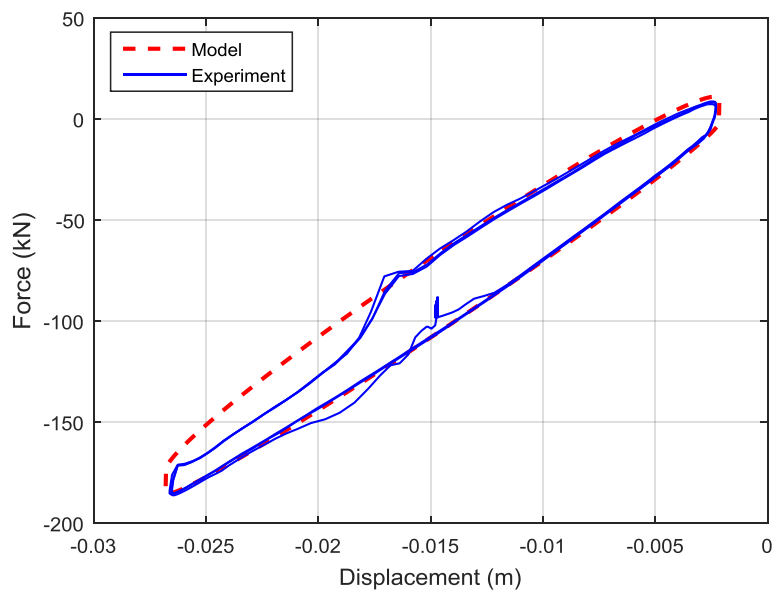


Figure 4.18. Comparisons between the model and experiments for $X = 0.0127$ m, $f = 2$ Hz, and zero current.

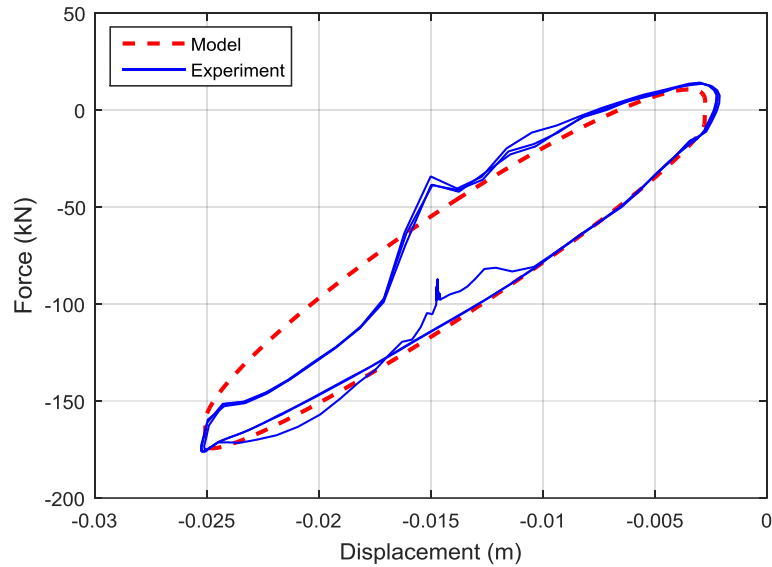


Figure 4.19. Comparisons between the model and experiments for $X = 0.0127$ m, $f = 4$ Hz, and zero current.

Figure 4.20-4.23 show the comparisons between the model and experimental data for $X = 0.0127$ m and different current and frequency levels. In Figure 4.20, the model matches well with the experimental data except that it is not able to capture the cut-out regions. From Section 4.4, a cut-out region was attributed to the fact that there was no flow in that region. Based on this discussion, the cut-out regions are modeled by setting the passive and controllable MR damping forces to zero in these regions. The comparisons between the modified model and experiments are shown in Figure 4.21-4.23. The plots show that the modified model can effectively model the cut-out regions.

Also it should be noted that comparisons are made only for the compression cycles, i.e. not for bi-linear cases, because of the no-stiffness regions observed in Figure 4.7-4.10.

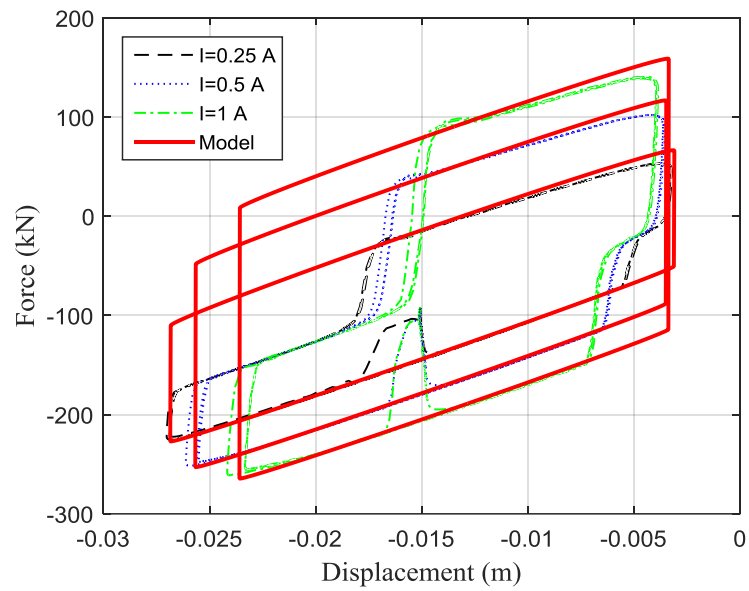


Figure 4.20. Comparisons between the model and experiments for $X = 0.0127$ m, $f = 1$ Hz, and different current levels (without modeling the cut-out regions).

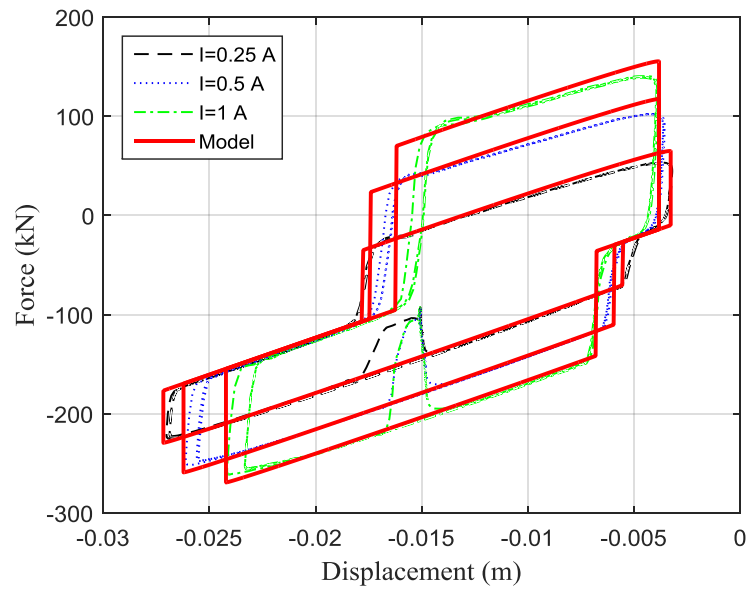


Figure 4.21. Comparisons between the model and experiments for $X = 0.0127$ m, $f = 1$ Hz, and different current levels.

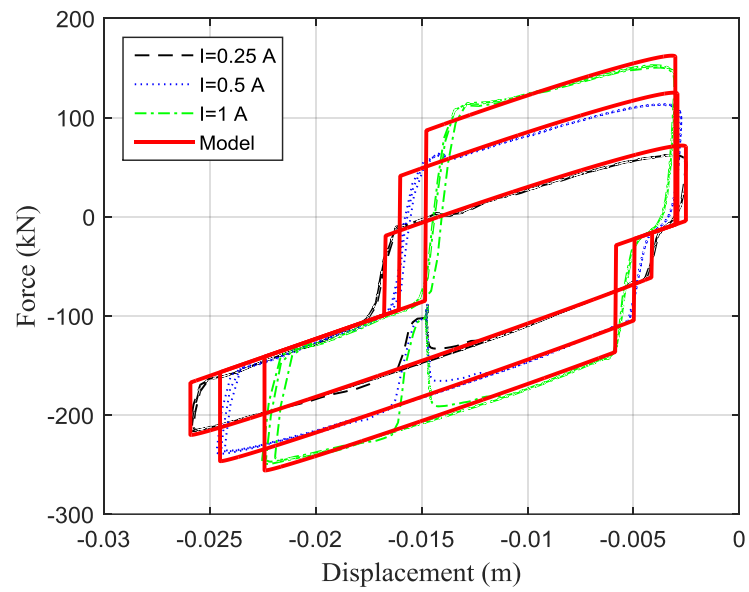


Figure 4.22. Comparisons between the model and experiments for $X = 0.0127$ m, $f = 2$ Hz, and different current levels.

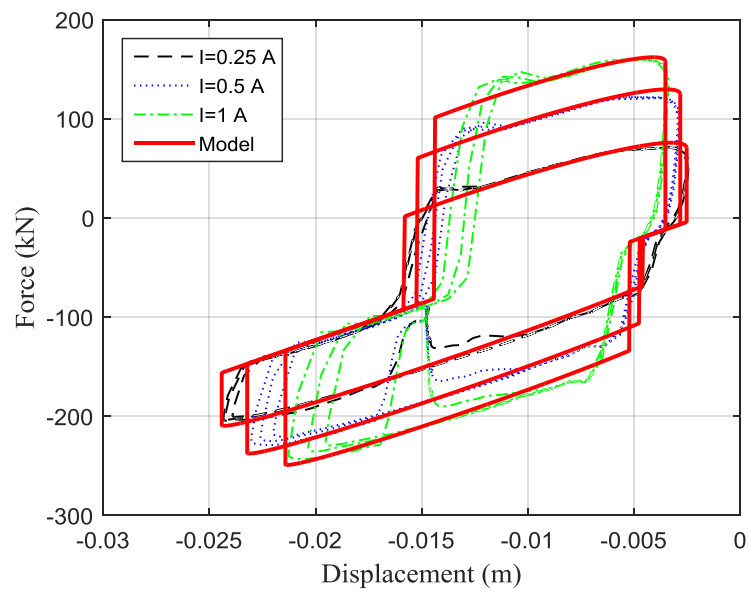


Figure 4.23. Comparisons between the model and experiments for $X = 0.0127$ m, $f = 4$ Hz, and different current levels.

CHAPTER 5 SUMMARY, CONCLUSIONS, AND FUTURE WORK

5.1. Summary

In this study, a fail-safe, bi-linear liquid spring, controllable magnetorheological damper was designed, built, and tested. The design of the BLS-CMRD involved both theoretical and simulation modeling to achieve the system requirements. The theoretical modeling was split into four steps: spring force, seal friction, fail-safe viscous damping, and controllable magnetorheological damping. Simulation modeling involved structural, electromagnetic, and thermal analyses. Structural analyses were conducted to ensure the safety of the structure under combined shear and axial loadings. The electromagnetic and thermal analyses were carried out to determine the magnetic flux density in the flow gap and to minimize the heat generation in the MR fluid, respectively. During these analyses, parametric studies were conducted to assess the effects of input parameters on the design requirements. The parametric studies revealed that the design targets were functions of some common geometric parameters. To achieve all design targets effectively, a comprehensive optimization program was developed in ANSYS software.

Next, the device was fabricated. Individual components were machined by different vendors, and later assembled in the LSSL of UNR, where the device was tested. The tests were conducted under sinusoidal loading and scaled seismic motions with varying strokes, frequencies, and applied current. The results proved that the device exhibited a distinct bi-linearity as expected. It is observed that the damping was increased as the excitation stroke, frequency, and current were increased. However, it is also observed that a portion of the damping was lost in the compression mode. This is

attributed to the entrapped air in the MR fluid, lack of accumulator in the top chamber, and difference in the shaft diameters. An alternative design was proposed to remedy the cut-out in the force vs. displacement loops. This design could also reduce the size of the device substantially. The tests were also conducted under combined axial and shear loadings. The device performed successfully under all applied shear loadings up to 28 kN. To our knowledge, it is the first time an MR damper was tested at combined axial and shear loadings and was shown to function successfully.

The design model was compared against the experimental data. It was seen that the model was able to match with the experimental data except that it was not able to capture the cut-out regions. The model was modified to match the cut-out regions by setting the passive and controllable damping to zero based on the discussions that the cut-out regions occurred due to no-flow in those regions. The modified model was able to match the cut-out regions.

5.2. Conclusions

- A bi-linear stiffness, fail-safe viscous, and controllable MR damping can be combined into a single unit that could work for the vertical component of a 3D earthquake isolation system of large building structures.

- For the first time, a BLS-CMRD was shown to perform successfully under combined axial and shear loadings.

5.3. Future Work

During the tests, the device reached the force capacity of the actuator. A higher capacity actuator can be utilized to capture the full dynamic behavior of the device under given and/or expanded test conditions.

To further investigate the effect of the trapped air in the MR fluid, the device can be filled with a more efficient deaeration process.

The size of the device could be reduced substantially by utilizing the design shown in Figure 4.12. This design configuration would also eliminate the effect of any entrapped that was believed to cause the lost in damping.

REFERENCES

- [1] G. P. Warn and K. L. Ryan, "A Review of Seismic Isolation for Buildings: Historical Development and Research Needs," *Buildings*, vol. 2, no. 4, pp. 300–325, Aug. 2012.
- [2] A. K. Agrawal and M. Amjadian, "Seismic component devices," in *Innovative Bridge Design Handbook Construction, Rehabilitation, and Maintenance*, no. November 2015, A. Pipinato, Ed. Massachusetts: Elsevier Inc., 2016, pp. 531–553.
- [3] Taylor Devices Inc., "Taylor Devices, Inc.-- History, design, and applications of fluid dampers in structural engineering," 2017. [Online]. Available: <http://taylordevices.com/papers/history/design.htm>. [Accessed: 05-Jan-2017].
- [4] S. Thenozhi and W. Yu, "Stability analysis of active vibration control of building structures using PD/PID control," *Eng. Struct.*, vol. 81, pp. 208–218, Dec. 2014.
- [5] T. T. . Soong and B. F. . Spencer Jr., "Supplemental energy dissipation: State-of-the-art and state-of-the-practice," *Eng. Struct.*, vol. 24, no. 3, pp. 243–259, 2002.
- [6] L. M. Jansen and S. J. Dyke, "Semiactive Control Strategies for MR Dampers: Comparative Study," *J. Eng. Mech.*, vol. 126, no. 8, pp. 795–803, Aug. 2000.
- [7] F. Yi, S. J. Dyke, J. M. Caicedo, and J. D. Carlson, "Experimental Verification of Multiinput Seismic Control Strategies for Smart Dampers," *J. Eng. Mech.*, vol. 127, no. 11, pp. 1152–1164, Nov. 2001.
- [8] R. Zemp, J. C. de la Llera, and F. Weber, "Experimental analysis of large capacity MR dampers with short- and long-stroke," *Smart Mater. Struct.*, vol. 23, no. 12, p.

125028, 2014.

- [9] G. Yang, B. F. Spencer, J. D. Carlson, and M. K. Sain, “Large-scale MR fluid dampers: modeling and dynamic performance considerations,” *Eng. Struct.*, vol. 24, pp. 309–323, 2002.
- [10] K. Esteki, “Developing new analytical and numerical models for mr fluid dampers and their application to seismic design of buildings,” Concordia University, 2014.
- [11] Z. Jiang, S. J. Kim, S. Plude, and R. Christenson, “Real-time hybrid simulation of a complex bridge model with MR dampers using the convolution integral method,” *Smart Mater. Struct.*, vol. 22, no. 10, p. 105008, Oct. 2013.
- [12] B. F. Spencer, G. Yang, J. . D. Carlson, and M. K. Sain, “Smart Dampers for Seismic Protection of Structures : A Full-Scale Study,” in *Proceedings of the 2nd World Conference on Structural Control*, 1998, pp. 1–10.
- [13] R. Reitherman, “Overview of the Northridge Earthquake,” in *Proceedings of the NEHRP Conference and Workshop on Research on the Northridge, California Earthquake of January 17, 1994*, 1998, p. I-1.
- [14] C. A. Kircher, “It makes dollars and sense to improve nonstructural system performance,” in *ATC-29-2 Proceedings of Seminar on Seismic Design, Performance, and Retrofit of Nonstructural Components in Critical Facilities*, 2003, pp. 109–119.
- [15] S. Malushte and A. Whittaker, “Survey of past base isolation applications in nuclear power plants and challenges to industry/regulatory acceptance,” *18th Int.*

Conf., 2005.

- [16] V. Zayas, S. Low, L. Bozzo, and S. Mahin, “Feasibility and performance studies on improving the earthquake resistance of new and existing buildings using the friction pendulum system,” Berkeley, California, 1989.
- [17] D. M. Fenz and M. C. Constantinou, “Spherical sliding isolation bearings with adaptive behavior: Theory,” *Earthq. Eng. Struct. Dyn.*, vol. 37, no. 2, pp. 163–183, Feb. 2008.
- [18] G. P. Warn, A. S. Whittaker, and M. C. Constantinou, “Vertical Stiffness of Elastomeric and Lead–Rubber Seismic Isolation Bearings,” *J. Struct. Eng.*, vol. 133, no. 9, pp. 1227–1236, Sep. 2007.
- [19] I. D. Aiken, J. M. Kelly, and F. F. Tajirian, “Mechanics of low shape factor elastomeric seismic isolation bearings,” Berkeley, California, 1989.
- [20] F. F. Tajirian, J. M. Kelly, I. D. Aiken, and W. Veljovich, “Elastomeric bearings for three-dimensional seismic isolation,” in *1990 ASME PVP CONFERENCE*, 1990.
- [21] I. G. Buckle and H. Liu, “Critical loads of elastomeric isolators at high shear strain,” *Tech. Rep. NCEER*, vol. 94–9, pp. 4-85-99, 1994.
- [22] I. Buckle, S. Nagarajaiah, and K. Ferrell, “Stability of Elastomeric Isolation Bearings: Experimental Study,” *J. Struct. Eng.*, vol. 128, no. 1, pp. 3–11, 2002.
- [23] J. Sanchez, A. Masroor, M. Asce, G. Mosqueda, A. M. Asce, and K. Ryan, “Static and Dynamic Stability of Elastomeric Bearings for Seismic Protection of

- Structures,” *J. Struct. Eng.*, vol. 139, no. 7, pp. 1149–1159, 2013.
- [24] S. Nagarajaiah and K. Ferrell, “Stability of elastomeric seismic isolation bearings,” *J. Struct. Eng.*, vol. 125, no. 9, pp. 946–954, 1999.
- [25] G. K. Huffmann, “Full base isolation for earthquake protection by helical springs and viscodampers,” *Nucl. Eng. Des.*, vol. 84, no. 3, pp. 331–338, 1985.
- [26] N. Makris and H. Deoskar, “Prediction of observed response of base-isolated structure,” *J. Struct. Eng.*, 1996.
- [27] K. Inoue, M. Morishita, and T. Fujita, “Development of Three-Dimensional Seismic Isolation Technology for Next Generation Nuclear Power Plant in Japan,” in *Seismic Engineering, Volume 2*, 2004, pp. 29–34.
- [28] J. Suhara, T. Tamura, K. Ohta, Y. Okada, and S. Moro, “Research on 3-D Base Isolation System Applied to New Power Reactor 3-D Seismic Isolation Device with Rolling Seal Type Air Spring: Part 1,” in *Transactions of the 17 th International Conference on Structural Mechanics in Reactor Technology (SMiRT 17)*, 2003, pp. 1–6.
- [29] J. Suhara, R. Matsumoto, S. Oguri, Y. Okada, K. Inoue, and K. Takahashi, “Research on 3-D Base Isolation System Applied To New Power Reactor 3-D Seismic Isolation Device with Rolling Seal Type Air Spring: Part 2,” in *18th International Conference on Structural Mechanics in Reactor Technology (SMiRT 18)*, 2005, pp. 3381–3391.
- [30] M. Kageyama, T. Iba, K. Umeki, T. Somaki, and S. Moro, “Development of Three

- Dimensional Base Isolation System with Cable Reinforcing Air Spring,” in *Transactions of the 17 th International Conference on Structural Mechanics in Reactor Technology (SMiRT 17)* , 2003, pp. 1–8.
- [31] M. Kageyama, Y. Hino, and S. Moro, “Study on Three-Dimensional Seismic Isolation System for Next Generation Nuclear Power Plant: Independent Cable Reinforced Rolling-Seal Air Spring,” in *Seismic Engineering, Volume 2*, 2004, pp. 49–56.
- [32] A. Kashiwazaki, T. Shimada, T. Fujiwaka, and S. Moro, “Study on 3-Dimensional Base Isolation System Applying to New Type Power Plant Reactor (Hydraulic 3-Dimensional Base Isolation System: No.1),” in *Transactions of the 17 th International Conference on Structural Mechanics in Reactor Technology (SMiRT 17)*, 2003, pp. 1–8.
- [33] Z. R. F. Taylor Paul H, “Liquid Springs,” US 2837329 A, 1958.
- [34] Taylor Paul H., “Fluid amplified liquid spring shock absorbers with improved piston heads,” US3722640 A, 1973.
- [35] P. H. Taylor, “Liquid spring-shock absorber assembly,” US3933344 A, 1976.
- [36] D. P. Taylor, “Liquid spring, vehicle suspension system and method for producing a low variance in natural frequency over a predetermined load range,” US3947004 A, 1976.
- [37] M. H. Naft and P. P. Seabase, “Applying the ‘Pressure’ to a Liquid Spring Off-Highway Truck Suspension.” SAE International, Milwaukee, p. 12, 1977.

- [38] L. W. Davis, "Liquid spring vehicular suspension system and associated control apparatus," US5316272 A, 1994.
- [39] R. F. Zumwalt, "Double-acting liquid spring," US 2899194 A, 1959.
- [40] N. R. Maus, "Fail-safe, Bi-directional Liquid Spring, Controllable Magnetorheological Fluid Damper," University of Nevada, Reno, 2013.
- [41] P. H. Taylor, "Liquid spring," US 2842356 A, 1958.
- [42] P. H. Taylor, "Liquid spring Seal," US 2909398 A, 1959.
- [43] Douglas P. Taylor, "Liquid energy absorber device," US 4389045 A, 1983.
- [44] P. H. Taylor, "Energy absorber device with composite plastic casing having high strength inner cylinder," US 4738339 A, 1988.
- [45] D. P. Taylor and D. A. Lee, "Shock isolation method and apparatus for ship-mounted device," US 4892051 A, 1990.
- [46] L. W. Davis, "Liquid spring having improved damper valve structure," US5305859 A, 1994.
- [47] C. R. Brown and W. T. Price, "Liquid spring mounting means for a launching tube," US 3221602 A, 1965.
- [48] L. R. Fagan C., "Energy absorbing landing gear," US3716208 A, 1973.
- [49] L. L. Rene, "Liquid spring shock-absorber," US 2650820 A, 1953.
- [50] H. G. Kirchner, "Vehicle suspension employing a liquid spring," US 4079923 A, 1978.

- [51] Z. B. Andrews, “Breaking liquid spring support with dormant lockout,” US3367235 A, 1968.
- [52] D. A. Lee, “Self-centering liquid spring assembly and constructions thereof,” US 5890705 A, 1999.
- [53] R. L. Vick, “Liquid spring accumulator with self-charging means,” EP 0089286 A2, 1983.
- [54] W. A. Gail, “Temperature compensated liquid spring,” US2992816 A, 1961.
- [55] D. Delorenzis, R. Meyer, and D. Lamkin, “Compressible liquid vibration control system,” US6293530 B1, 2001.
- [56] D. Delorenzis, C. Cajulis, and R. J. Meyer, “Single valve control of damping and stiffness in a liquid spring system,” US6598885 B2, 2003.
- [57] D. Delorenzis and R. J. Meyer, “Seamless control of spring stiffness in a liquid spring system,” US6679504 B2, 2004.
- [58] W. H. Hogan, “Double acting liquid shock isolator,” US2723847 A, 1955.
- [59] P. H. Taylor, “Tension-compression liquid spring unit,” US4630805 A, 1986.
- [60] W. Kordonsky, “Elements and Devices Based on Magnetorheological Effect,” *J. Intell. Mater. Syst. Struct.*, vol. 4, no. 1, pp. 65–69, Jan. 1993.
- [61] O. Ashour, C. A. Rogers, and W. Kordonsky, “Magnetorheological Fluids: Materials, Characterization, and Devices,” *J. Intell. Mater. Syst. Struct.*, vol. 7, no. 2, pp. 123–130, Mar. 1996.

- [62] J. D. Carlson and M. R. Jolly, "MR Fluid, foam and elastomer devices," *Mechatronics*, vol. 10, no. 4–5, pp. 555–569, 2000.
- [63] P. P. Phulé, "Magnetorheological (MR) Fluids: Principles And Applications," *Smart Mater. Bull.*, vol. 2001, no. 2, pp. 7–10, 2001.
- [64] J. Rabinow, "The Magnetic Fluid Clutch," *Trans. Am. Inst. Electr. Eng.*, vol. 67, no. 2, pp. 1308–1315, 1948.
- [65] D. Guo and H. Hu, "Nonlinear Stiffness of a Magneto-Rheological Damper," *Nonlinear Dyn.*, vol. 40, pp. 241–249, 2005.
- [66] H. Sahin, Y. Liu, X. Wang, F. Gordaninejad, C. Evrensel, and A. Fuchs, "Full-Scale Magnetorheological Fluid Dampers for Heavy Vehicle Rollover," *J. Intell. Mater. Syst. Struct.*, vol. 18, no. 12, pp. 1161–1167, 2007.
- [67] H. Sahin, "Theoretical and Experimental Studies of Magnetorheological (MR) Fluids and MR Greases/Gels: From Rheology to System Application," University of Nevada, Reno, 2008.
- [68] X. Wang and F. Gordaninejad, "Lyapunov-Based Control of a Bridge Using Magneto-Rheological Fluid Dampers," *J. Intell. Mater. Syst. Struct.*, vol. 13, no. 7–8, pp. 415–419, Jul. 2002.
- [69] Wang Xiaojie and Gordaninejad Faramarz, "Magnetorheological Materials and their Applications," in *Intelligent Materials*, Mohsen Shahinpoor and Hans-Jörg Schneider, Ed. The Royal Society of Chemistry, 2008, pp. 339–385.
- [70] B. M. Kavlicoglu, "A new unified theory for flow analysis of magneto-rheological

- (MR) fluids and application of MR fluids in a high-torque clutch,” 2006.
- [71] L. A. Ahure-Powell, “Magnetorheological fluids and applications to adaptive landing gear for a lightweight helicopter,” 2014.
- [72] D. Simon and M. Ahmadian, “Vehicle Evaluation of the Performance of Magneto Rheological Dampers for Heavy Truck Suspensions,” *J. Vib. Acoust.*, vol. 123, no. 3, p. 365, 2001.
- [73] W. W. Chooi and S. O. Oyadiji, “Design, modelling and testing of magnetorheological (MR) dampers using analytical flow solutions,” 2007.
- [74] S.-R. Hong, G. Wang, W. Hu, and N. M. Wereley, “Liquid spring shock absorber with controllable magnetorheological damping,” *Proc. Inst. Mech. Eng. Part D J. Automob. Eng.*, vol. 220, no. 8, pp. 1019–1029, 2006.
- [75] G. Hitchcock and F. Gordaninejad, “Controllable compressible fluid damper,” US7422092 B2, 2008.
- [76] S. Mantripragada, “A controllable MRF damper with a liquid spring device,” University of Nevada, Reno, 2009.
- [77] P. Raja, “Design and Development of a Compressible Magneto-Rheological Damper,” University of Nevada, Reno, 2009.
- [78] P. Raja, X. Wang, and F. Gordaninejad, “A high-force controllable MR fluid damper–liquid spring suspension system,” *Smart Mater. Struct.*, vol. 23, no. 1, p. 15021, Jan. 2014.
- [79] M. R. Potnuru, X. Wang, S. Mantripragada, and F. Gordaninejad, “A compressible

- magneto-rheological fluid damper – liquid spring system,” *Int. J. Veh. Des.*, vol. 63, no. 2–3, pp. 256–274, 2013.
- [80] M. J. McKee, “Effects of Temperature on Performance of Compressible Magnetorheological Fluid Dampers,” University of Nevada, Reno, 2010.
- [81] M. McKee, X. Wang, and F. Gordaninejad, “Effects of temperature on performance of a compressible magnetorheological fluid damper-liquid spring suspension system,” *J. Intell. Mater. Syst. Struct.*, no. Special Issue Article, pp. 1–11, 2017.
- [82] N. Maus and F. Gordaninejad, “A fail-safe, bi-linear liquid spring controllable magnetorheological fluid damper,” in *SPIE Smart Structures and Materials + Nondestructive Evaluation and Health Monitoring*, 2014, p. 90570Q.
- [83] S. Kitayama and M. C. Constantinou, “Fluidic Self-Centering Devices as Elements of Seismically Resistant Structures : Description , Testing , Modeling , and Model Validation,” *J. Struct. Eng.*, vol. 143, no. 7, pp. 1–10, 2017.
- [84] “Beemer Precision, Inc. - Oilite - Sleeve & Flange Bearings, Flexible Couplings - Sintered Products.” [Online]. Available: <http://www.oilite.com/>. [Accessed: 15-Apr-2017].
- [85] “Adhesives, Coatings, Vibration and Motion Control, Sensing, and Magnetically Responsive Technologies | LORD Corp.” [Online]. Available: <http://www.lord.com/>. [Accessed: 31-Dec-2016].
- [86] A. Spaggiari and E. Dragoni, “Effect of pressure on the physical properties of

magnetorheological fluids,” *Fract. Struct. Integr.*, no. 23, p. Pages 75-86, 2012.

- [87] A. Spaggiari and E. Dragoni, “Combined Squeeze-shear Properties of Magnetorheological Fluids: Effect of Pressure,” *J. Intell. Mater. Syst. Struct.*, vol. 25, no. 9, pp. 1041–1053, 2014.
- [88] A. C. Becnel, S. G. Sherman, W. Hu, and N. M. Wereley, “Squeeze strengthening of magnetorheological fluids using mixed mode operation,” *J. Appl. Phys.*, vol. 117, no. 17, pp. 1–5, 2015.

APPENDIX A. Device Assembly Protocol

The device was assembled in the order shown in Figure A.1-A.7.

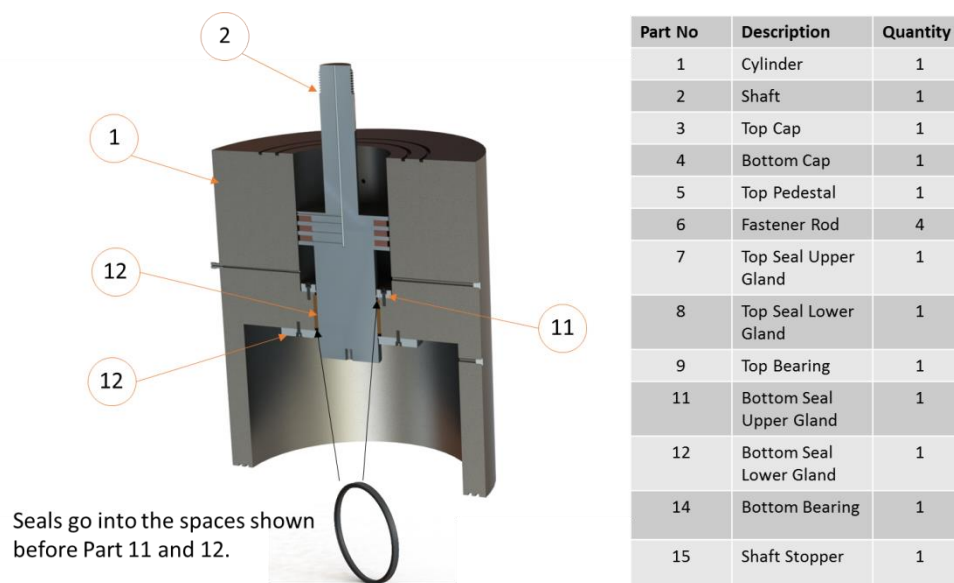


Figure A.1. Step 1: Insert the shaft into the cylinder bore (the bottom bearing, seals, bottom seal lower and upper glands were installed on the cylinder).

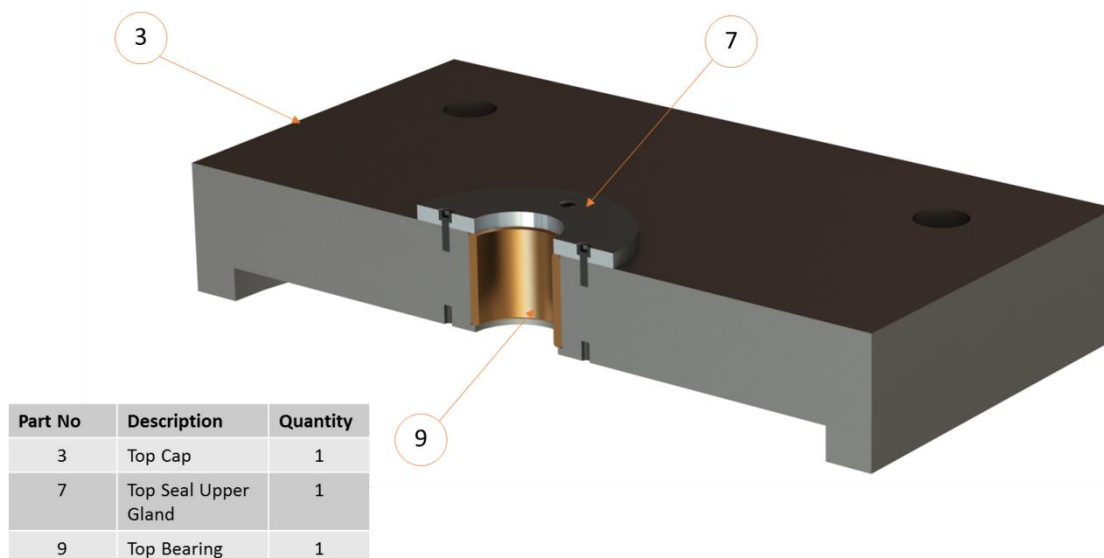


Figure A.2. Step 2: Install the top seal upper gland (the top bearing was already press-fitted).

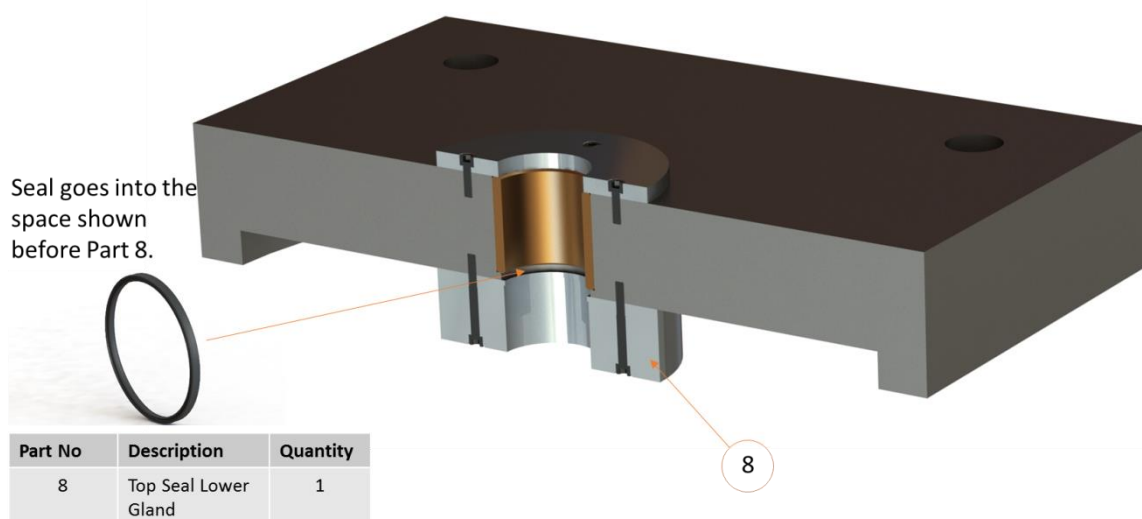
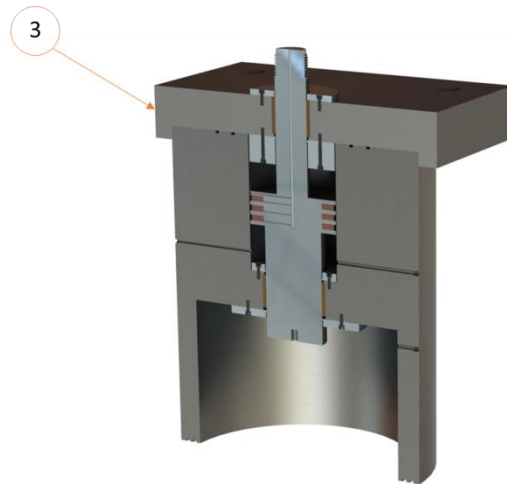
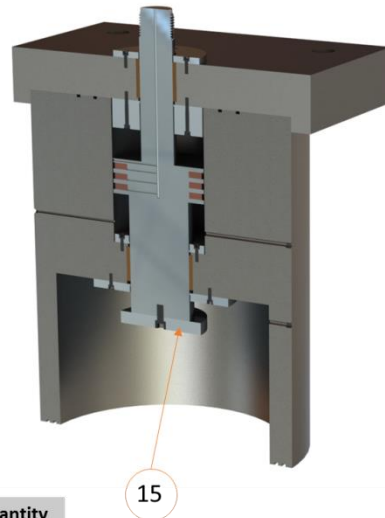


Figure A.3. Step 3: Install the top seal lower gland.



Part No	Description	Quantity
3	Top Cap	1

Figure A.4. Step 4: Insert the top cap on the shaft.



Part No	Description	Quantity
15	Shaft Stopper	1

Figure A.5. Step 5: Install the shaft stopper on the bottom side of the shaft.

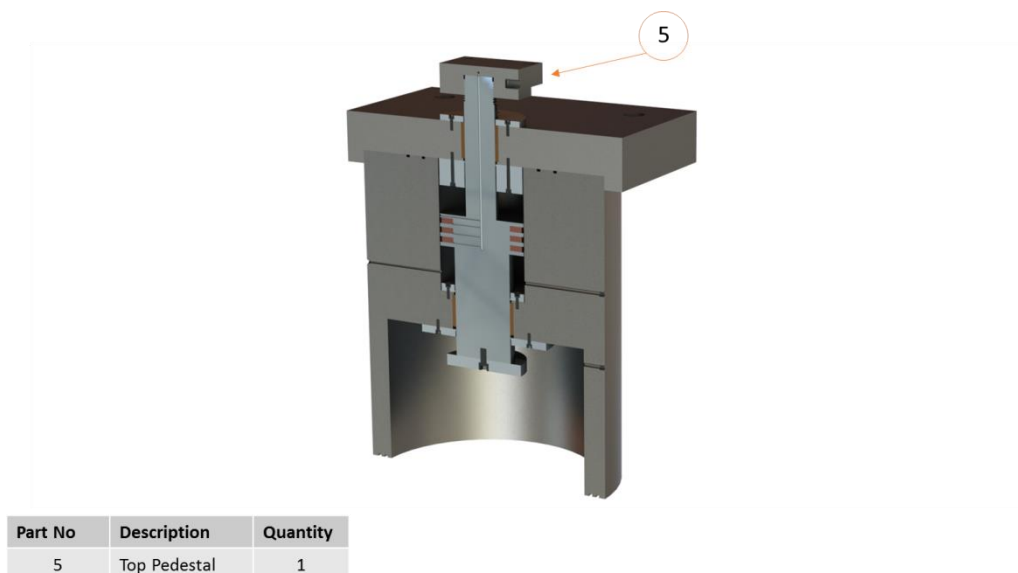


Figure A.6. Step 6: Install the top pedestal on the on the top side of the shaft.

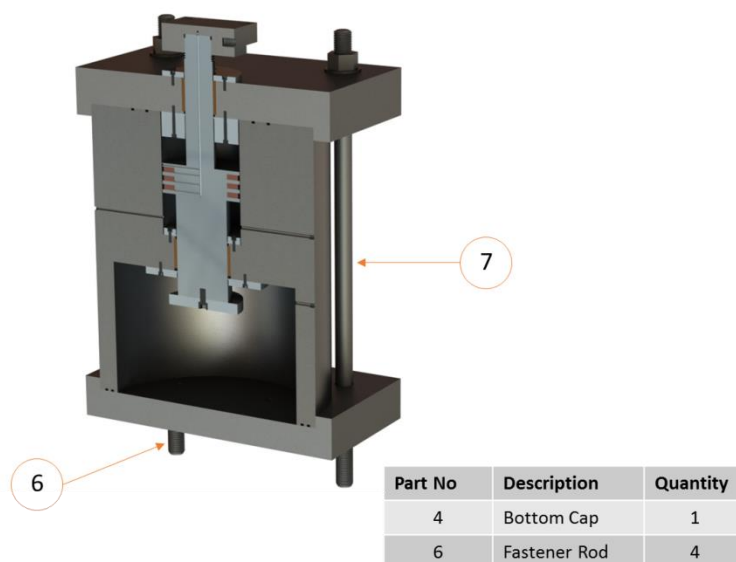


Figure A.7. Step 7: Install the bottom cap and fasten the external fastener rods on the top and bottom Caps.

APPENDIX B. Test Protocol

The testing combinations followed during the characterization of the BLS-CMRD are given in this appendix.

Table B.1. Expanded form of the axial test.

Axial Tests								
Test ID	Amplitude (m)	Number of cycles	Shear load (N)	Current (A)	Frequency (f)	Velocity (m/s)	Repeats	Remarks
000	Preload the static displacement = 0.01547 m							
001	0.0127	3	0	0	0.5	0.03990	3	No. of cycles are 9.
002	0.0127	3	0	0.5	0.5	0.03990	1	
003	0.0127	3	0	1	0.5	0.03990	1	
004	0.0127	3	0	3	0.5	0.03990	1	
101	0.0127	3	0	0	0.1	0.00798	1	
102	0.0127	3	0	0.5	0.1	0.00798	1	
103	0.0127	3	0	1	0.1	0.00798	1	
104	0.0127	3	0	3	0.1	0.00798	1	
005	0.0127	3	0	0	1	0.07980	1	
006	0.0127	3	0	0.25	1	0.07980	1	
007	0.0127	3	0	0.5	1	0.07980	1	
008	0.0127	3	0	1	1	0.07980	1	
009	0.0127	3	0	0	2	0.15959	1	
010	0.0127	3	0	0.25	2	0.15959	1	
011	0.0127	3	0	0.5	2	0.15959	1	
012	0.0127	3	0	1	2	0.15959	1	
013	0.0127	3	0	0	4	0.31919	1	
014	0.0127	3	0	0.25	4	0.31919	1	
015	0.0127	3	0	0.5	4	0.31919	1	
016	0.0127	3	0	1	4	0.31919	1	
017	0.0254	3	0	0	0.5	0.07980	1	
018	0.0254	3	0	0.25	0.5	0.07980	1	
019	0.0254	3	0	0.5	0.5	0.07980	1	
020	0.0254	3	0	1	0.5	0.07980	1	
021	0.0254	3	0	0	1	0.15959	1	
022	0.0254	3	0	0.25	1	0.15959	1	
023	0.0254	3	0	0.5	1	0.15959	1	
024	0.0254	3	0	1	1	0.15959	1	
025	0.0254	3	0	0	2	0.31919	3	No. of cycles are 9.
026	0.0254	3	0	0.25	2	0.31919	1	
027	0.0254	3	0	0.5	2	0.31919	1	
028	0.0254	3	0	1	2	0.31919	1	
029	0.0254	3	0	0	4	0.63837	1	
030	0.0254	3	0	0.25	4	0.63837	1	
031	0.0254	3	0	0.5	4	0.63837	1	
032	0.0254	3	0	1	4	0.63837	1	

Table B.2. Expanded form of the axial test-Continued.

Axial Tests								
Test ID	Amplitude (m)	Number of cycles	Shear load (N)	Current (A)	Frequency (f)	Velocity (m/s)	Repeats	Remarks
053	0.0127	3	0	0	0.5	0.03990	3	No. of cycles are 9.
054	0.0127	3	0	0.5	0.5	0.03990	1	
055	0.0127	3	0	1	0.5	0.03990	1	
056	0.0127	3	0	3	0.5	0.03990	1	
057	0.0127	3	0	0	1	0.07980	1	
058	0.0127	3	0	0.25	1	0.07980	1	
059	0.0127	3	0	0.5	1	0.07980	1	
060	0.0127	3	0	1	1	0.07980	1	
061	0.0127	3	0	0	2	0.15959	1	
062	0.0127	3	0	0.25	2	0.15959	1	
063	0.0127	3	0	0.5	2	0.15959	1	
064	0.0127	3	0	1	2	0.15959	1	
065	0.0127	3	0	0	4	0.31919	1	
066	0.0127	3	0	0.25	4	0.31919	1	
067	0.0127	3	0	0.5	4	0.31919	1	
068	0.0127	3	0	1	4	0.31919	1	
069	0.0254	3	0	0	0.5	0.07980	1	
070	0.0254	3	0	0.25	0.5	0.07980	1	
071	0.0254	3	0	0.5	0.5	0.07980	1	
072	0.0254	3	0	1	0.5	0.07980	1	
073	0.0254	3	0	0	1	0.15959	1	
074	0.0254	3	0	0.25	1	0.15959	1	
075	0.0254	3	0	0.5	1	0.15959	1	
076	0.0254	3	0	1	1	0.15959	1	
077	0.0254	3	0	0	2	0.31919	1	
078	0.0254	3	0	0.25	2	0.31919	1	
079	0.0254	3	0	0.5	2	0.31919	1	
080	0.0254	3	0	1	2	0.31919	1	
081	0.0254	3	0	0	4	0.63837	1	
082	0.0254	3	0	0.25	4	0.63837	1	
083	0.0254	3	0	0.5	4	0.63837	1	
084	0.0254	3	0	1	4	0.63837	1	

Table B.3. Axial earthquake tests.

Axial Earthquake Tests			
Test ID	Current (A)	Repeats	Remarks
EQ1-100-P	0	1	Northridge-01, LA-Sepulveda V A Hospital - 100% Design Level - Pasive OFF
EQ2-100-P	0	1	Loma Prieta, LGPC - 100% Design Level - Pasive OFF
EQ3-100-P	0	1	Chi-Chi, TCU079 - 100% Design Level - Pasive OFF
EQ1-150-P	0	1	Northridge-01, LA-Sepulveda V A Hospital - 150% Design Level - Pasive OFF
EQ2-150-P	0	1	Loma Prieta, LGPC - 150% Design Level - Pasive OFF
EQ3-150-P	0	1	Chi-Chi, TCU079 - 150% Design Level - Pasive OFF
EQ1-150-I0.5	0.5	1	Northridge-01, LA-Sepulveda V A Hospital - 150% Design Level - Pasive ON - Current 0.5 Amp
EQ2-150-I0.5	0.5	1	Loma Prieta, LGPC - 150% Design Level - Pasive ON - Current 0.5 Amp
EQ3-150-I0.5	0.5	1	Chi-Chi, TCU079 - 150% Design Level - Pasive ON - Current 0.5 Amp
EQ1-200-I0.5	0.5	1	Northridge-01, LA-Sepulveda V A Hospital - 200% Design Level - Pasive ON - Current 0.5 Amp
EQ2-200-I0.5	0.5	1	Loma Prieta, LGPC - 200% Design Level - Pasive ON - Current 0.5 Amp
EQ3-200-I0.5	0.5	1	Chi-Chi, TCU079 - 200% Design Level - Pasive ON - Current 0.5 Amp
EQ1-200-I3	3	1	Northridge-01, LA-Sepulveda V A Hospital - 200% Design Level - Pasive ON - Current 3 Amp
EQ2-200-I3	3	1	Loma Prieta, LGPC - 200% Design Level - Pasive ON - Current 3 Amp
EQ3-200-I3	3	1	Chi-Chi, TCU079 - 200% Design Level - Pasive ON - Current 3 Amp
EQ1-250-I3	3	1	Northridge-01, LA-Sepulveda V A Hospital - 250% Design Level - Pasive ON - Current 3 Amp
EQ2-250-I3	3	1	Loma Prieta, LGPC - 250% Design Level - Pasive ON - Current 3 Amp
EQ3-300-I3	3	1	Chi-Chi, TCU079 - 300% Design Level - Pasive ON - Current 3 Amp

Table B.4. Combined axial and shear tests.

Combined Axial and Shear Tests								
Test ID	Amplitude (m)	Number of cycles	Shear load (N)	Current (A)	Frequency (f)	Velocity (m/s)	Repeats	Remarks
033	0.0254	3	1112.06	0	1	0.15959	1	
034	0.0254	3	1112.06	0	4	0.63837	1	
035	0.0254	3	1112.06	1	1	0.15959	1	
036	0.0254	3	1112.06	1	4	0.63837	1	
037	0.0254	3	3336.17	0	1	0.15959	1	
038	0.0254	3	3336.17	0	4	0.63837	1	
039	0.0254	3	3336.17	1	1	0.15959	1	
040	0.0254	3	3336.17	1	4	0.63837	1	
041	0.0254	3	6672.33	0	1	0.15959	1	
042	0.0254	3	6672.33	0	4	0.63837	1	
043	0.0254	3	6672.33	1	1	0.15959	1	
044	0.0254	3	6672.33	1	4	0.63837	1	
045	0.0254	3	13344.66	0	1	0.15959	1	
046	0.0254	3	13344.66	0	4	0.63837	1	
047	0.0254	3	13344.66	1	1	0.15959	1	
048	0.0254	3	13344.66	1	4	0.63837	1	
049	0.0254	3	27840	0	1	0.15959	1	
050	0.0254	3	27840	0	4	0.63837	1	
051	0.0254	3	27840	1	1	0.15959	1	
052	0.0254	3	27840	1	4	0.63837	1	

APPENDIX C. Fabrication Drawings of the BLS-CMRD

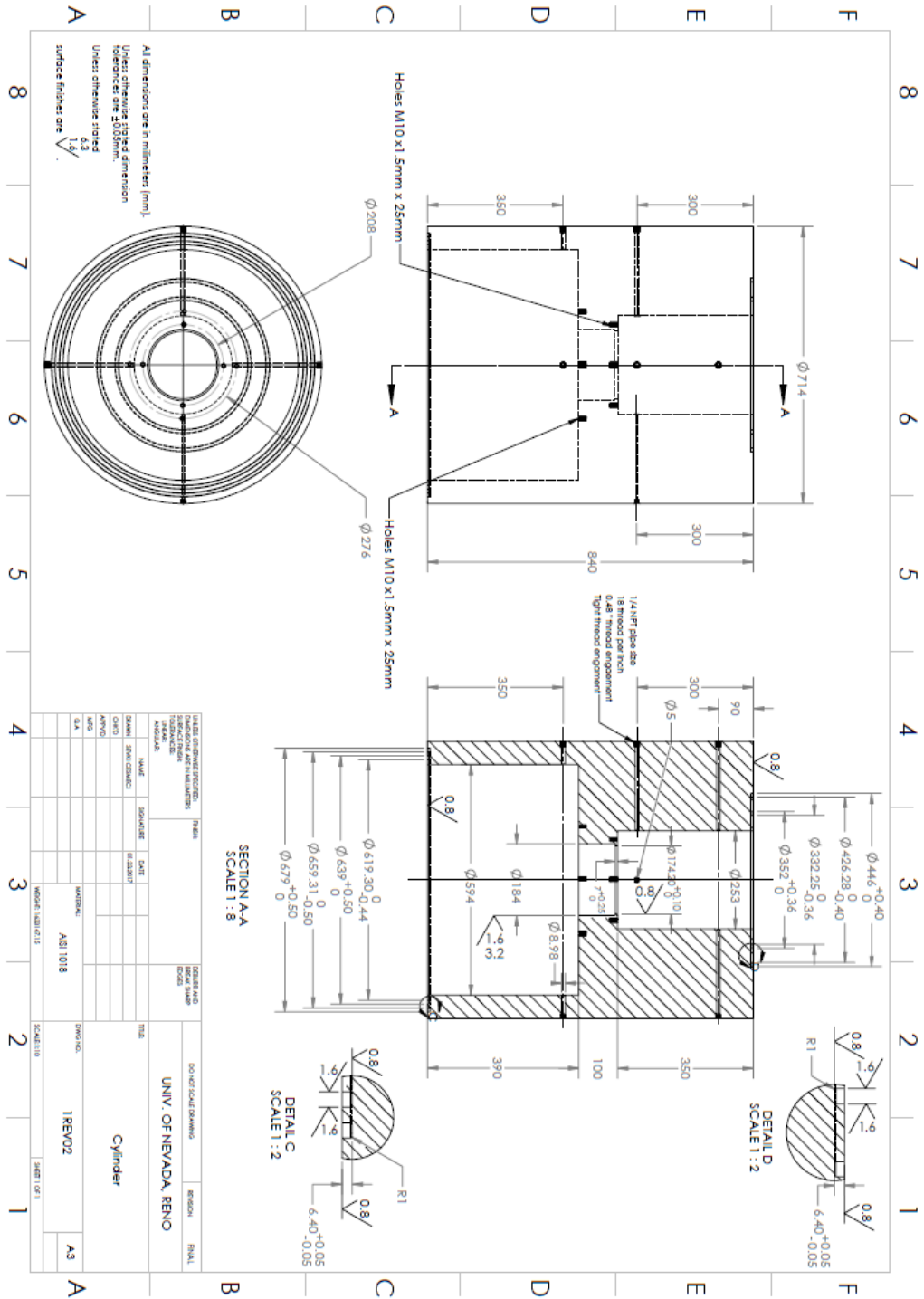


Figure C.1. 2D technical drawing for the cylinder.

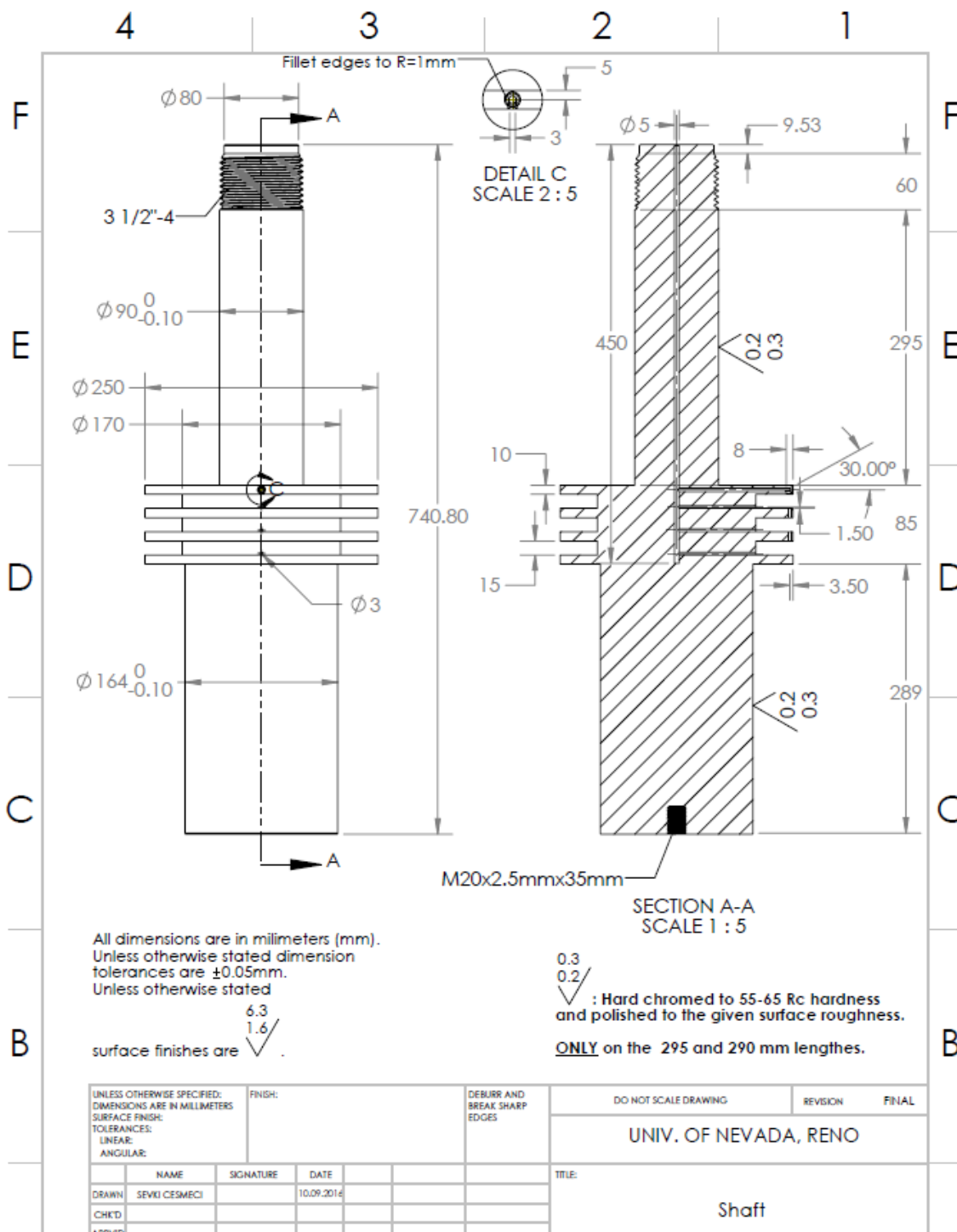


Figure C.2. 2D technical drawing for the shaft.

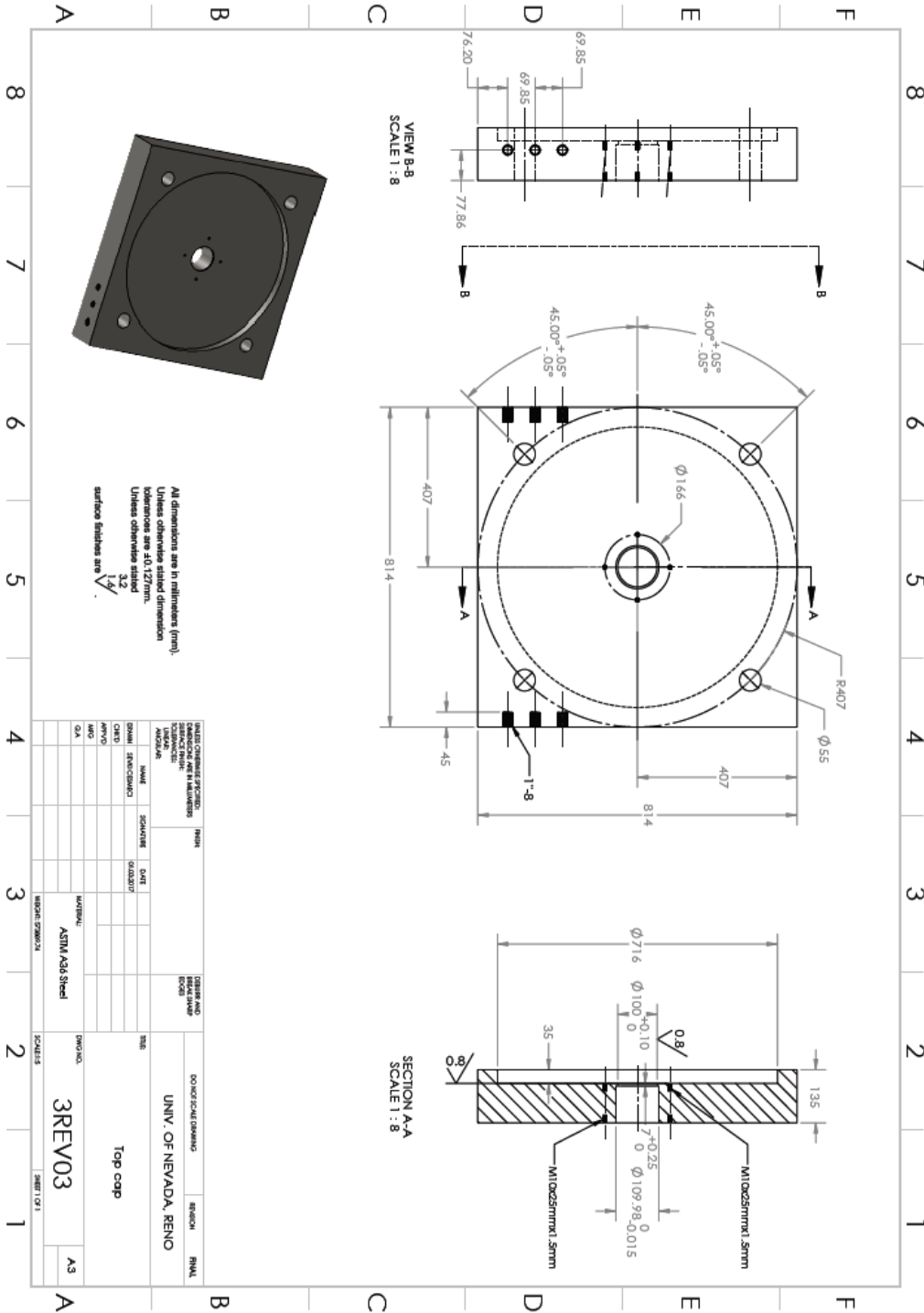


Figure C.3. 2D technical drawing for the top cap.

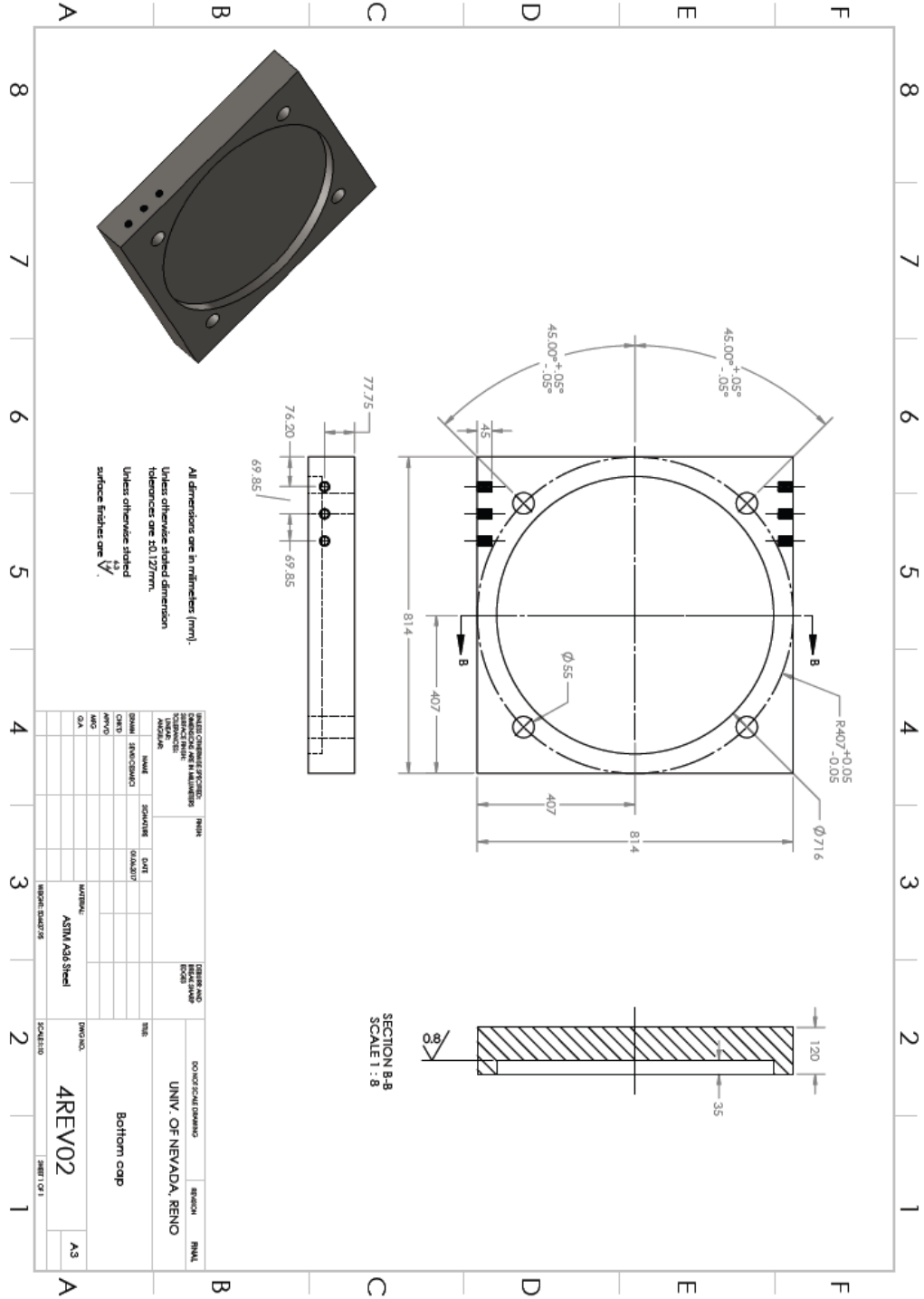


Figure C.4. 2D technical drawing for the bottom cap.

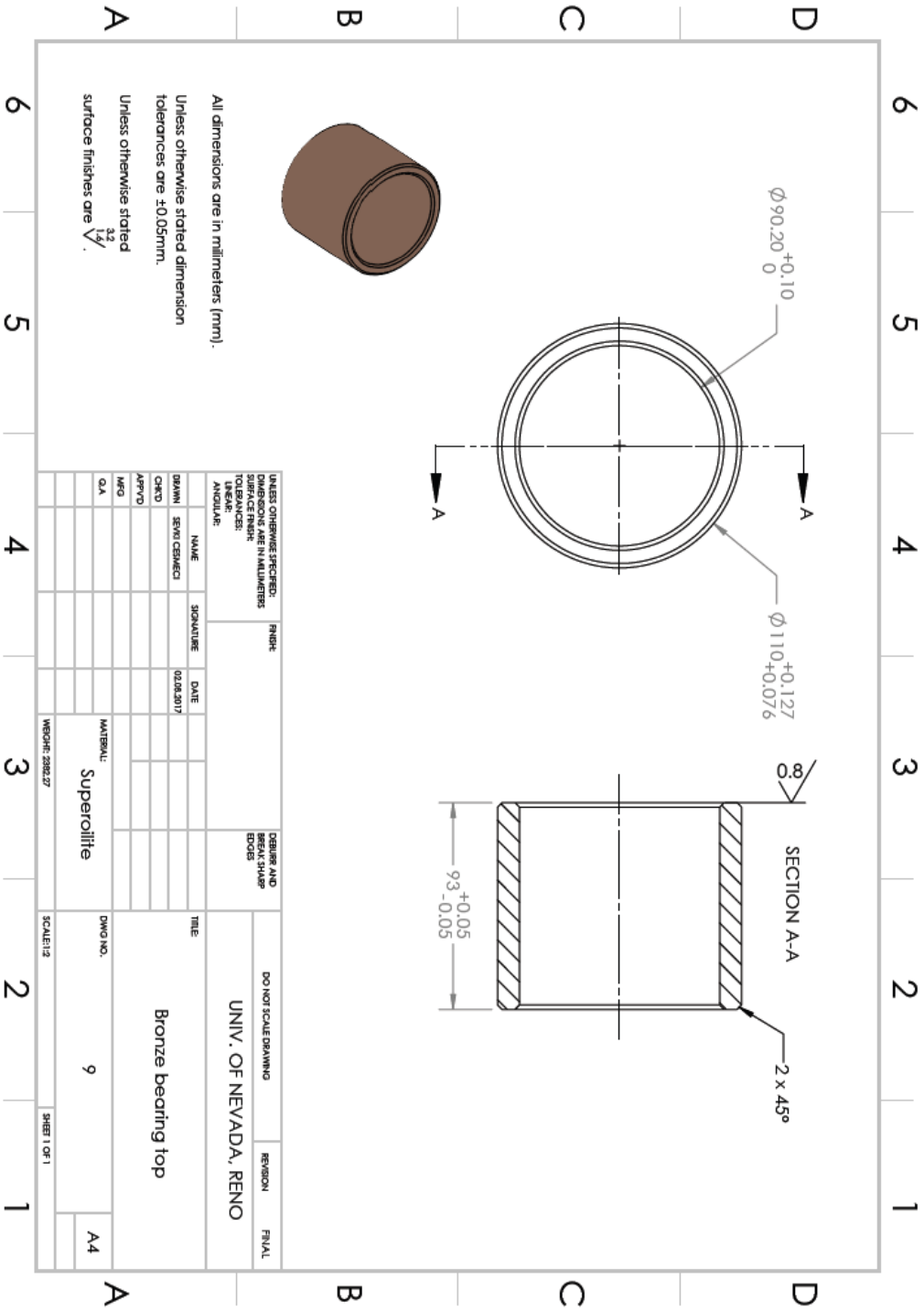


Figure C.6. 2D technical drawing for the top bearing.

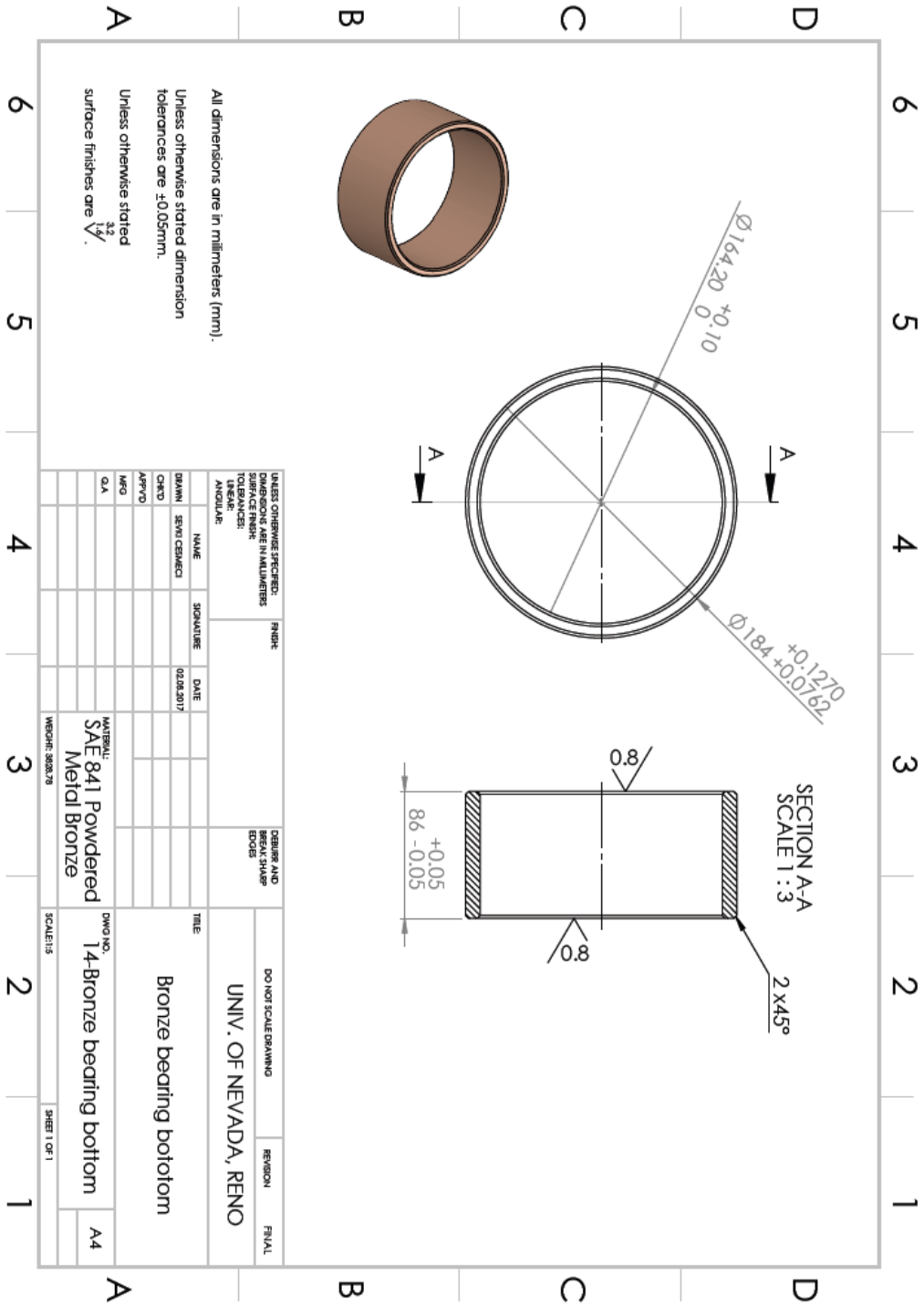


Figure C.7. 2D technical drawing for the bottom bearing.

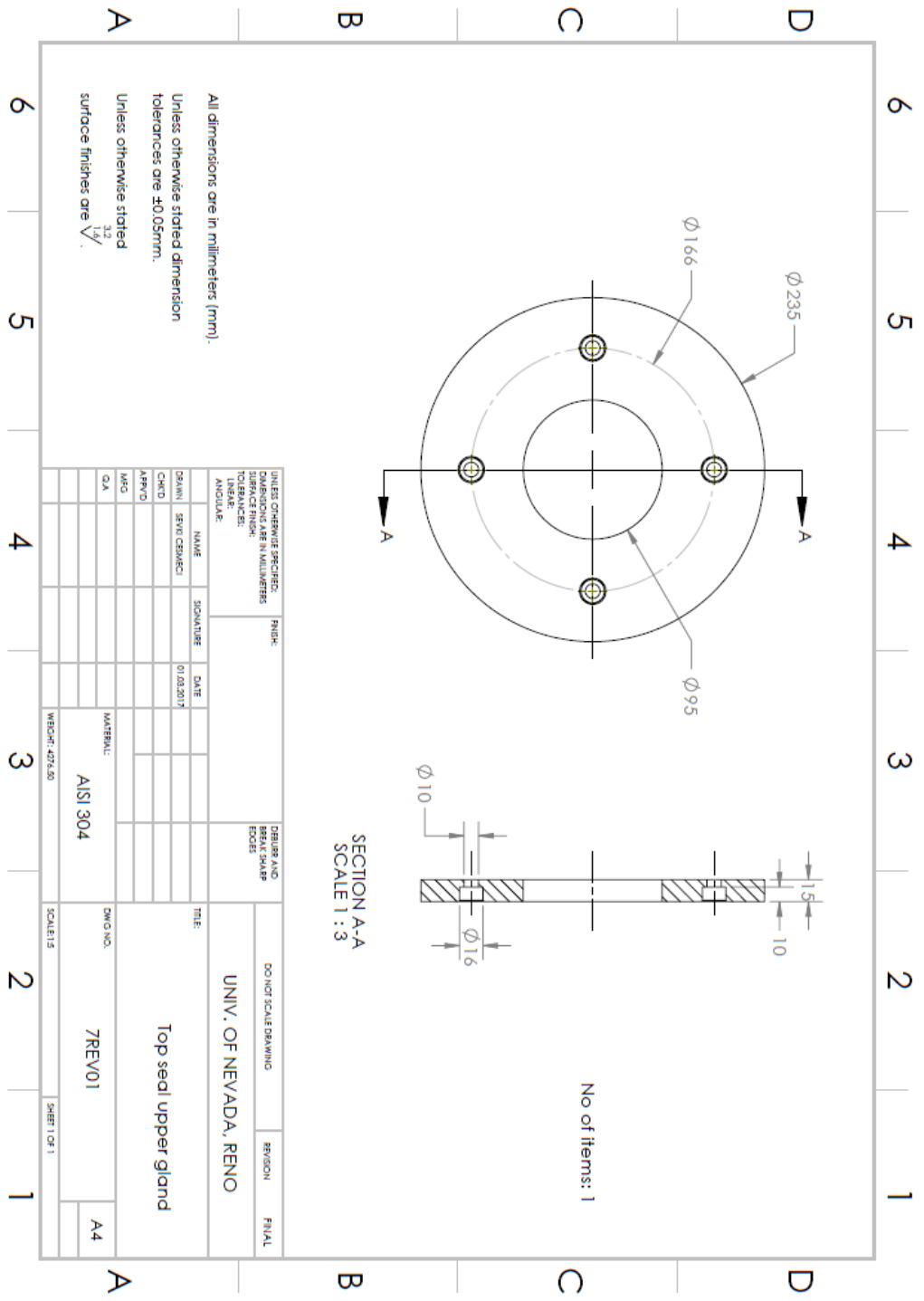


Figure C.8. 2D technical drawing for the top seal upper gland.

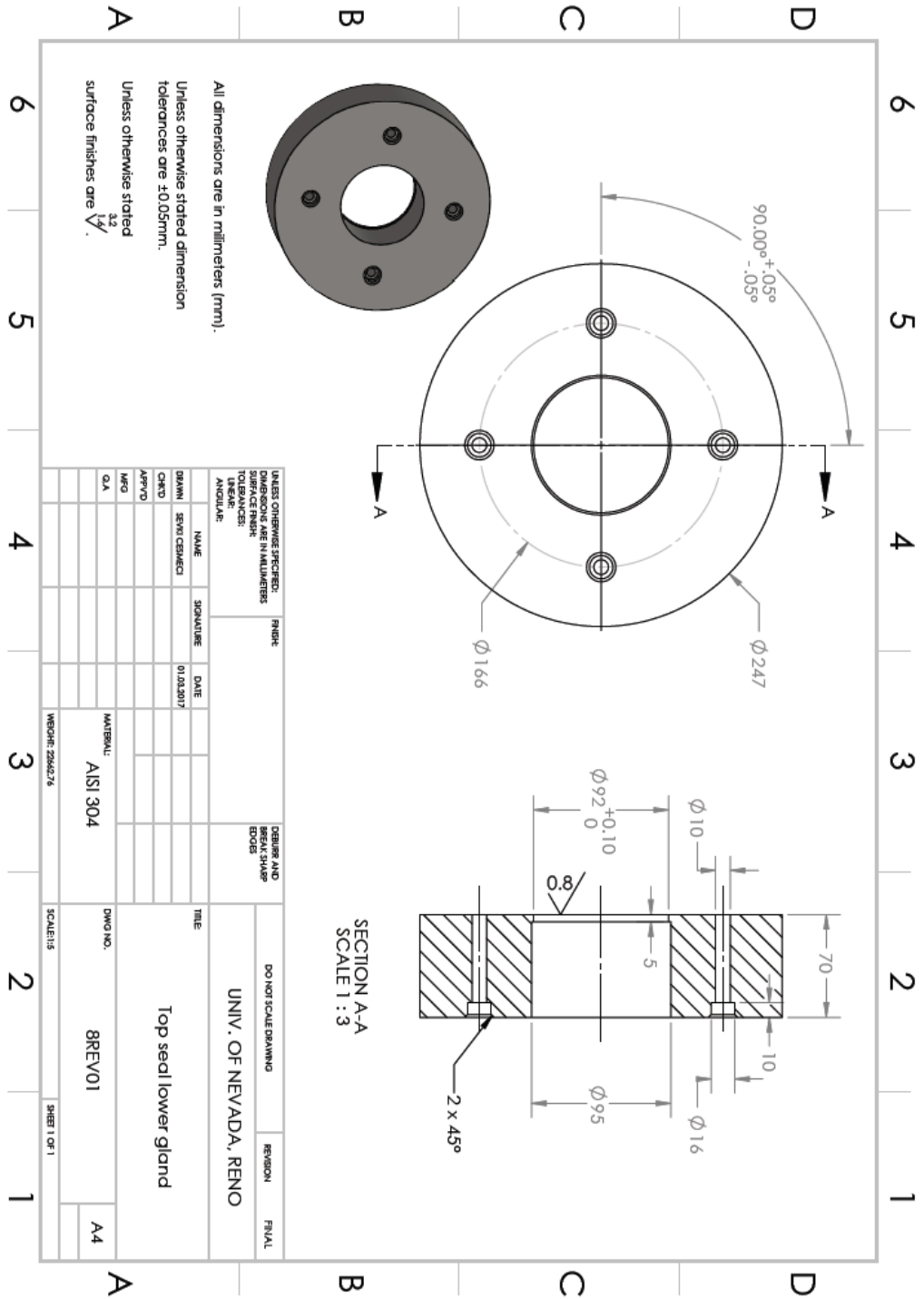


Figure C.9. 2D technical drawing for the top seal lower gland.

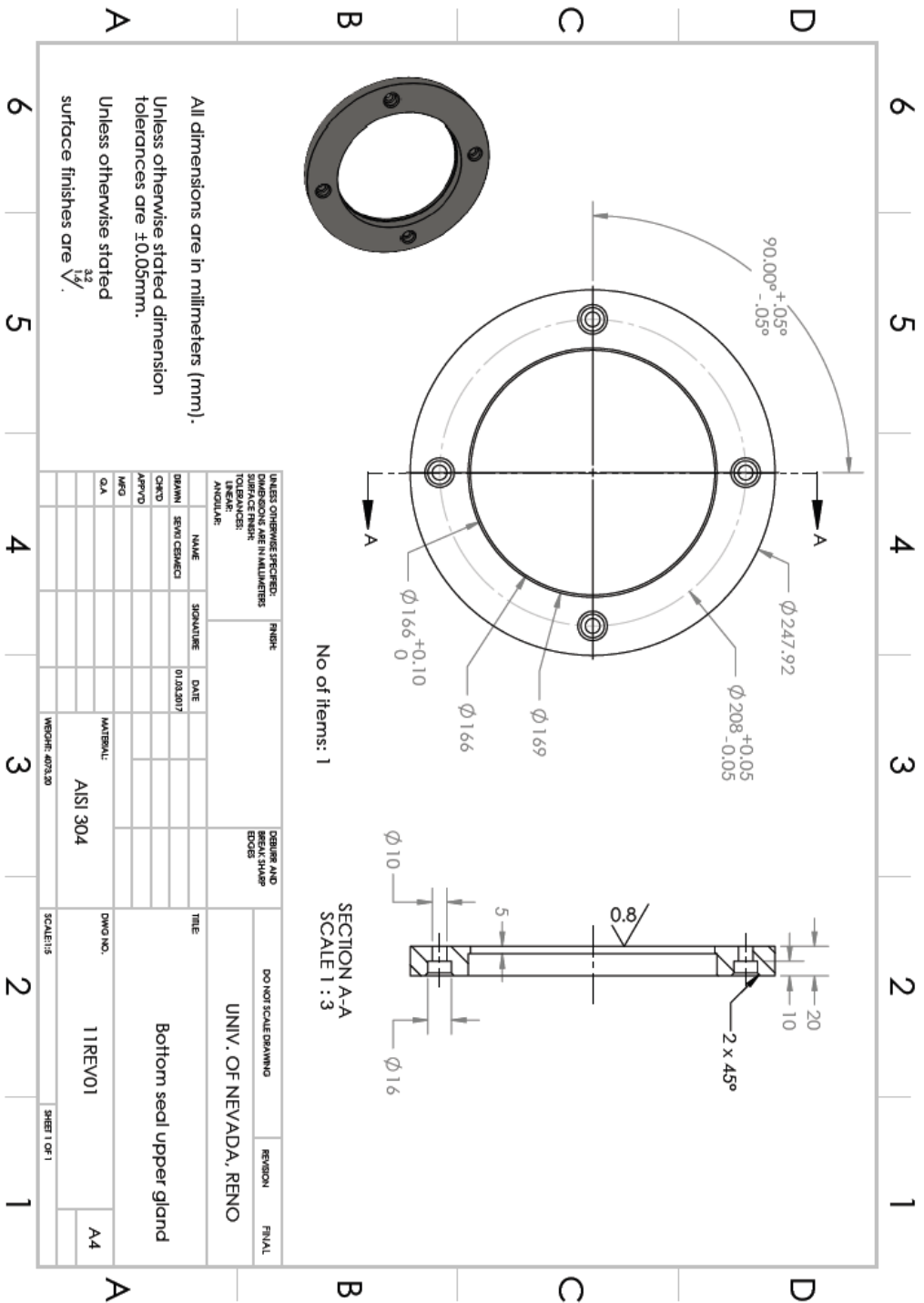


Figure C.10. 2D technical drawing for the bottom seal upper gland.

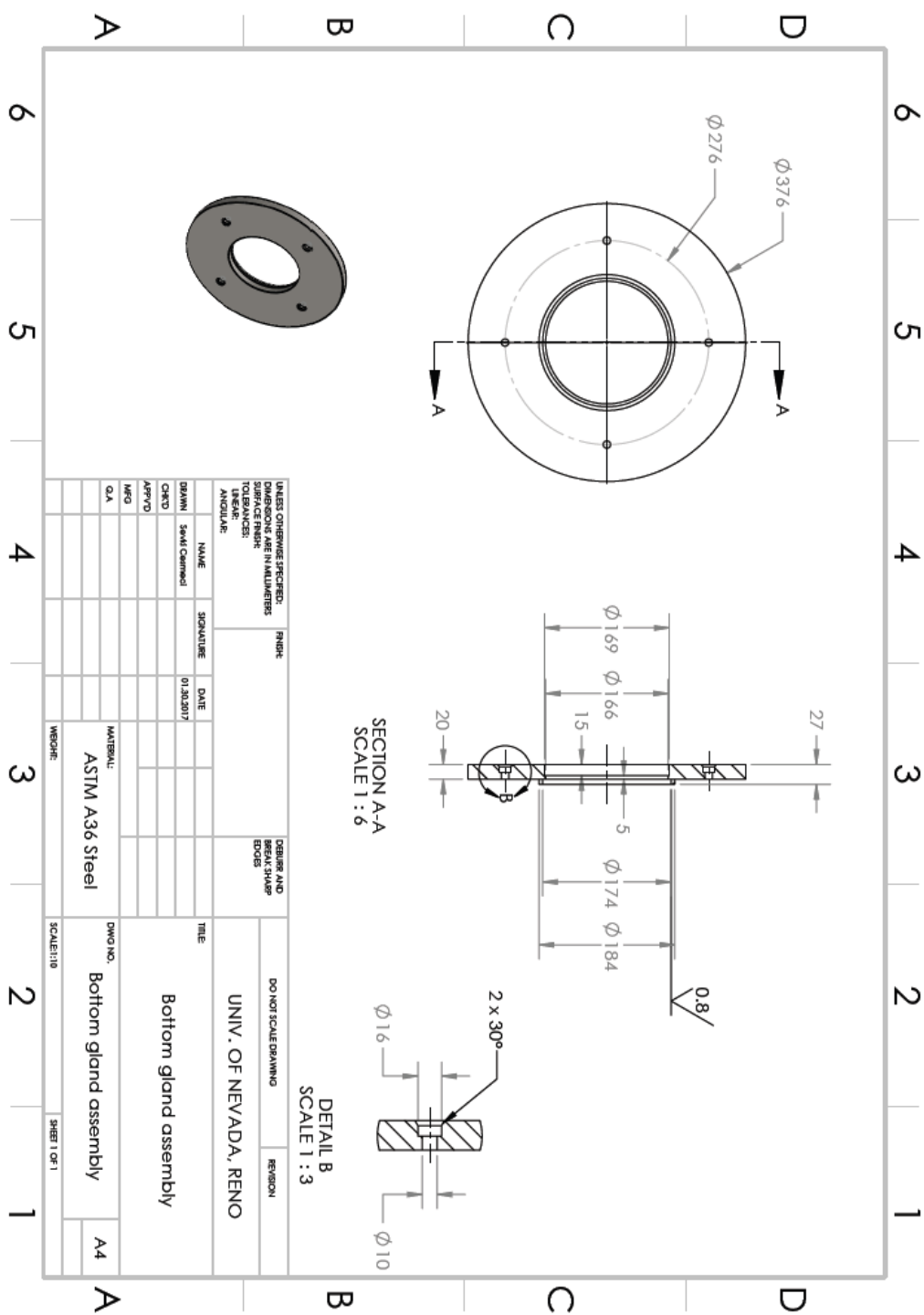


Figure C.11. 2D technical drawing for the bottom seal bottom gland assembly.

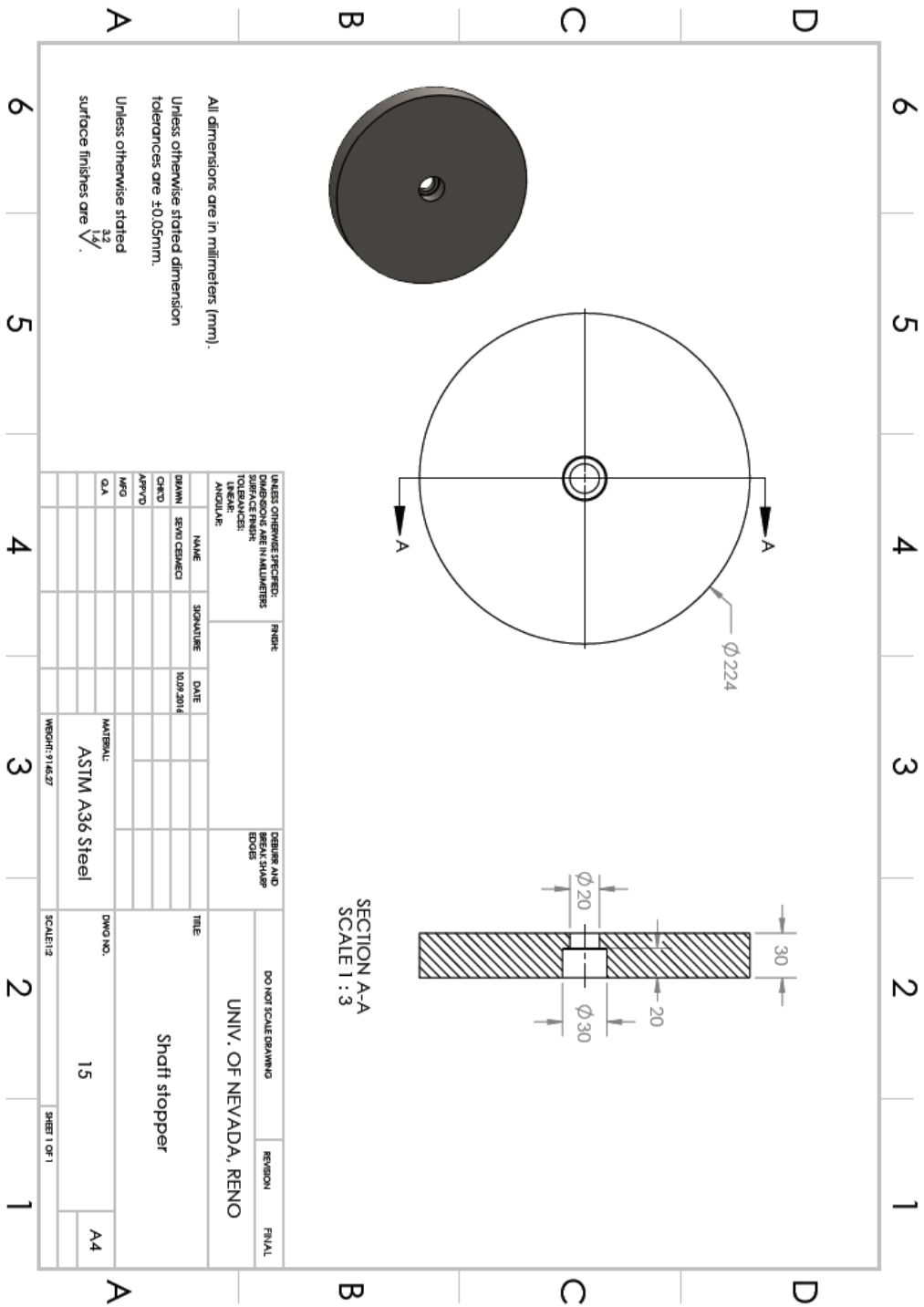


Figure C.12. 2D technical drawing for the shaft stopper.